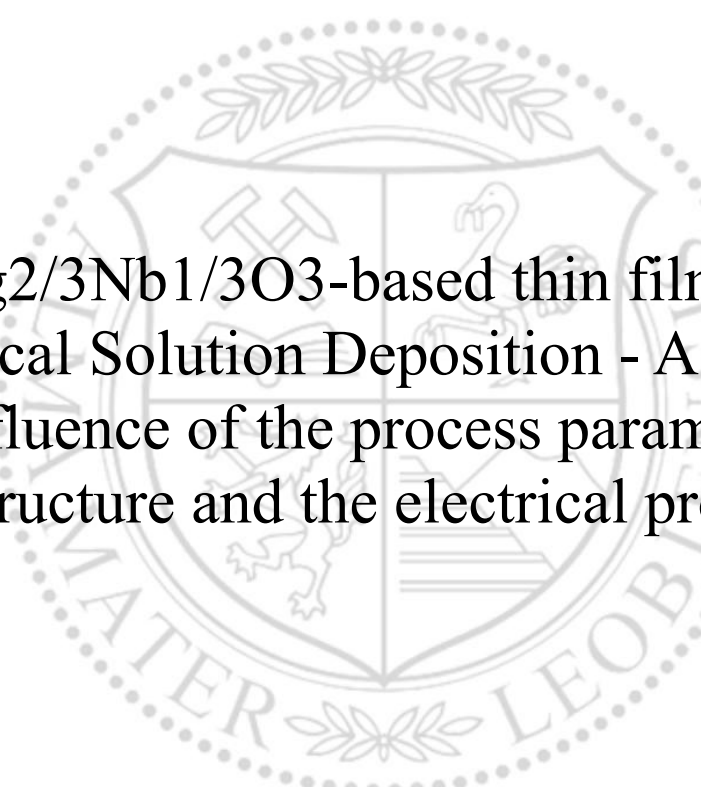Chair of Structural and Functional Ceramics

Master's Thesis

BiMg2/3Nb1/3O3-based thin films from Chemical Solution Deposition - A study on the influence of the process parameters on the structure and the electrical properties

Theresa Gindel, BSc

February 2024

MONTANUNIVERSITÄT LEOBEN
www.unileoben.ac.at

EIDESSTATTLICHE ERKLÄRUNG

Ich erkläre an Eides statt, dass ich diese Arbeit selbstständig verfasst, andere als die angegebenen Quellen und Hilfsmittel nicht benutzt, den Einsatz von generativen Methoden und Modellen der künstlichen Intelligenz vollständig und wahrheitsgetreu ausgewiesen habe, und mich auch sonst keiner unerlaubten Hilfsmittel bedient habe.

Ich erkläre, dass ich den Satzungsteil „Gute wissenschaftliche Praxis" der Montanuniversität Leoben gelesen, verstanden und befolgt habe.

Weiters erkläre ich, dass die elektronische und gedruckte Version der eingereichten wissenschaftlichen Abschlussarbeit formal und inhaltlich identisch sind.

Datum 12.02.2024

_____
Unterschrift Verfasser/in
Theresa Gindel

Acknowledgments

I would like to express my gratitude to everyone who supported me during my master's studies and while writing my Master's thesis. First, I would like to thank Priv.-Doz. Dr. Marco Deluca for giving me the opportunity to do my Master's thesis in his team.

My greatest thanks go to Herbert Kobald and Alexander Kobald for supervising and mentoring my diploma thesis. I am very grateful to them for their extensive support and numerous insights. I would also like to thank Ivana Panžić for her good scientific advice and all the helpful discussions and Martina Angermann for her support.

Also, I want to acknowledge the entire Sensor Solutions Team, at the Microelectronics Department of the Materials Center Leoben Forschung GmbH, for granting me the opportunity and providing guidance throughout my Master's thesis.

My gratitude extends to my family, particularly my parents Sigrid and Herbert, and my brother Simon. Their constant encouragement and unwavering support have been my foundation in successfully completing this academic degree.

Furthermore, I want to thank my friends and fellow students Martin, Philip, Daniel, Barbara and Lisa for the unforgettable moments during our study years. The times spent away from studying, at various gatherings and other experiences, have created cherished memories. Most importantly Federica, who has been there for me always. Federica, I want to express my heartfelt appreciation for the cherished memories we've created together, the life experiences we've shared, and for always being there to lend an ear whenever I needed to vent or express my concerns about something.

Last but not least, I would like to express my deepest gratitude to my boyfriend Daniel. Your presence has been my anchor throughout this academic journey, and I am endlessly grateful for your unwavering emotional support and uplifting distractions. You mean the world to me, and I am grateful for the significant difference you have made with your constant encouragement.

Abstract

Enhancing the energy storage properties of lead-free dielectric capacitors is a key focus in today's microelectronic industry. This objective is gaining importance in the quest to develop lead-free devices that align with lead-based property standards while minimizing the toxicity associated with processing and the end products. $BiMg_{2/3}Nb_{1/3}O_3$-based thin films show promising energy storage properties due to the disruption of the long-range ferroelectric order. The relaxor-like behavior results in slimmer polarization vs. electric field hysteresis loops (PE loops) compared to ferroelectrics and leading to a significant reduction in energy losses while maintaining a high permittivity. The use of thin film technology, as opposed to bulk ceramics, is a crucial step in the miniaturization of devices. In addition, this technique increases energy density and breakdown fields by improving microstructure and promoting texture.

In this thesis, thin films based on $(1-x)Bi(Mg_{2/3}Nb_{1/3})O_3–xBi_{0.5}Na_{0.5}TiO_3$ (BMN-BNT, x = 0.85) and $(1-x)Bi(Mg_{2/3}Nb_{1/3})O_3–xNaNbO_3$ (BMN-NN, x = 0.78) systems were produced by chemical solution deposition (CSD) on $Pt/TiO_2/SiO_2/Si$ substrates. All films have been successfully synthesized and the influence of different heating rates and crystallization temperatures on the microstructure and electrical properties have been investigated and characterized. Characterization analysis was carried out using Raman spectroscopy, X-ray diffraction (XRD), scanning electron microscopy (SEM) and Energy-Dispersive X-ray (EDX) analysis. Electrical measurements (PE loops) were conducted to evaluate the energy storage properties and to gain insights into the temperature-dependent response and cyclic fatigue behavior of the various films. Both thin film systems show a phase pure and highly crystalline perovskite structure in both XRD and Raman spectroscopy. The BMN-BNT composition showed the most promising energy storage properties (W_{rec} ~ 20 J/cm^3 and 69% efficiency), coupled with excellent thermal stability up to 140°C. However, superior cyclic fatigue stability, extending up to 10^6 unipolar cycles, and low leakage currents were observed for the BMN-NN system. In a broader context, it can be confirmed that varying process parameters significantly impact both the microstructure and the electrical properties of the two material systems. The complex interplay between structural characteristics and electrical behavior underscores the need of thorough exploration of processing conditions in achieving tailored material properties.

Keywords: BMN, Thin films, Chemical Solution Deposition, Process parameters

Kurzfassung

Die Verbesserung der Energiespeichereigenschaften von bleifreien dielektrischen Kondensatoren ist ein wichtiger Aspekt in der heutigen Mikroelektronikindustrie. Dieses Ziel gewinnt zunehmend an Bedeutung in dem Bestreben, bleifreie Geräte zu entwickeln, die Normen für bleihaltige Eigenschaften einhalten und gleichzeitig die mit der Verarbeitung und den Endprodukten verbundene Toxizität minimieren. Dünnschichten auf Basis von $BiMg_{2/3}Nb_{1/3}O_3$ zeigen vielversprechende Energiespeichereigenschaften aufgrund der Unterbrechung der langen Reichweite der ferroelektrischen Ordnung. Das relaxor-ähnliche Verhalten führt im Vergleich zu Ferroelektrika zu schlankeren Hystereseschleifen zwischen Polarisation und elektrischem Feld (PE-Schleifen) und damit zu geringeren Energieverlusten bei gleichzeitiger Beibehaltung einer hohen Permittivität. Die Verwendung von Dünnschichttechnologie an Stelle von Bulk-Keramik ist entscheidend für die Geräteminiaturisierung und steigert die Energiedichte, sowie die Durchbruchsfelder durch verbesserte Mikrostruktur und Texturförderung.

In dieser Arbeit wurden Dünnschichten basierend auf $(1-x)Bi(Mg_{2/3}Nb_{1/3})O_3–xBi_{0.5}Na_{0.5}TiO_3$ (BMN-BNT, x = 0.85) und $(1-x)Bi(Mg_{2/3}Nb_{1/3})O_3–xNaNbO_3$ (BMN-NN, x = 0.78) mittels chemischer Lösungsabscheidung (CSD) auf $Pt/TiO_2/SiO_2/Si$-Substraten hergestellt. Alle Filme wurden erfolgreich synthetisiert, der Einfluss verschiedener Heizraten und Kristallisationstemperaturen auf die Mikrostruktur und die elektrischen Eigenschaften wurde untersucht und charakterisiert. Die Charakterisierungsanalyse umfasste Ramanspektroskopie, Röntgenbeugung (XRD), Rasterelektronenmikroskopie (SEM) und energiedispersive Röntgenanalyse (EDX). Elektrische Messungen wurden durchgeführt, um die Energiespeichereigenschaften zu bewerten und Einblicke in das temperaturabhängige Verhalten sowie das zyklische Ermüdungsverhalten der verschiedenen Filme zu gewinnen. Beide Dünnschichtsysteme zeigen sowohl im XRD als auch in der Ramanspektroskopie eine phasenreine und hochkristalline Perowskitstruktur. Die BMN-BNT Zusammensetzung zeigte die vielversprechendsten Energiespeichereigenschaften (W_{rec} ~ 20 J/cm^3, 69% Effizienz), sowie eine ausgezeichnete thermische Stabilität bis 140 °C. Das BMN-NN System zeigte eine bessere zyklische Ermüdungsstabilität, bis zu 10^6 unipolaren Zyklen, und niedrige Leckströme. Es kann nachgewiesen werden, dass die unterschiedlichen Prozessparameter sowohl die Mikrostruktur als auch die elektrischen Eigenschaften der beiden Materialsysteme erheblich beeinflussen. Das komplexe Zusammenspiel zwischen strukturellen Merkmalen und elektrischem Verhalten unterstreicht eine notwendige gründliche Untersuchung der Verarbeitungsbedingungen, um maßgeschneiderte Materialeigenschaften zu erzielen.

Table of Content

1   Introduction

The growing world population and the increasing networking of electronic devices are leading to higher energy consumption, which requires new autonomous electrical energy storage systems (EESS) to compensate for the discontinuity of renewable energy sources. Efficient EESS tailored to specific applications can be divided into four main classes: (1) solid oxide fuel cells, (2) conventional batteries (Li-ion), (3) electrochemical capacitors and (4) dielectric capacitors. Two important parameters, the energy density and the power density, determine the suitability of the EESS classes for certain applications. In the scope of this thesis, the focus is on dielectric capacitors with a particular emphasis on ferroelectric and relaxor-like materials. These materials exhibit a broad spectrum of applications, ranging from capacitors to non-linear optical devices. Employing ferroelectric thin films is particularly advantageous due to the prospect of tailoring their properties through precise control of the films' crystallographic texture. Chemical solution deposition (CSD) offers a straightforward and environmentally friendly route for fabricating oxide films and also a rapid screening of the properties. Nonetheless, a comprehensive understanding of the intricate processes of decomposition and crystallization is imperative to systematically engineer and understand the film's properties. [1]

Despite the lower energy density, dielectric capacitors offer advantages such as high-power density, higher operating voltages, lower costs, size flexibility, thermal and cyclic stability and adjustable leakage currents, which makes them interesting for many applications. Achieving high energy density in dielectric capacitors while maintaining high power density opens up new possibilities for versatility, cost efficiency and miniaturization. [1, 2] It should be noted that the properties of thin films differ from those of the bulk materials, leading to complexities that must be considered in the search for an improved capacitor performance. The differences could occur due to size effects that lead to changes in the microstructure and the interaction between substrate and film, especially in the case of growth phenomena at the bottom electrode. Also, the thermal expansion mismatch influences the nucleation, texture and final properties, making the growth of ferroelectric thin films more complex.

To select a suitable material system for capacitor applications, the decision was made not to use the well-known ferroelectric lead-based materials. The European Union has established the Restriction of the Use of Certain Hazardous Substances (RoHS), prohibiting the introduction of electrical and electronic equipment containing more than 0.1 weight percent of lead – if replaceable – as lead is not only toxic and environmentally damaging but it also produces volatile Pb-gases during processing, which poses risks to production personnel. [3] Furthermore, the decision aligns with addressing recycling challenges and environmental concerns during the end-of-life

stages. Considering these factors, an alternative material system was deemed necessary to address both performance requirements and environmental concerns in capacitor applications.

The reason for researching $BiMg_{2/3}Nb_{1/3}O_3$ lies in the observed similarities with $PbMg_{1/3}Nb_{2/3}O_3$. From the chemical perspective, lead and bismuth share similarities in the perovskite structures, both characterized by the lone pair effect, resulting in high polarizations. However, the introduction of heterovalent substitution results in a different behavior that requires further investigation. Understanding the unique behavior resulting from this substitution is crucial for discovering the full potential and special properties of $BiMg_{2/3}Nb_{1/3}O_3$ and opens the way for its effective application and integration into various material systems.

Bismuth proves to be a promising alternative to Pb. To overcome this challenge, the exploration of combinations with other materials could present a feasible solution. A widely used system is the lead-based $PbMg_{1/3}Nb_{2/3}O_3$-$PbTiO_3$, where B-site substitution with Ti takes place. However, in lead-free alternatives for this system Bi^{3+} is used instead of Pb^{2+}. Therefore, A-site substitution is needed to keep charge neutrality in the perovskite unit cell instead of just adapting the B-site. Furthermore, the fraction of the B-site ions is contrary in the lead-free to the lead-based because of the same reason. In this work both, A- and B-site substitutions, are done. Additionally, $NaNbO_3$ (NN) was introduced to the $BiMg_{2/3}Nb_{1/3}O_3$-system (BMN), due to its recognized advantageous fatigue behavior properties. [4]

This work includes process adaptations and variations for the two material systems, BMN-BNT as well as BMN-NN, in order to determine ideal conditions and find the optimal electrical and structural properties for the binary system, which serve as a central starting point for further research.

2 Theoretical background

This section covers the theory behind the material systems, the device architecture, the fabrication procedure as well as the applied characterization techniques.

2.1 Ferroelectricity

Dielectrics are electrical insulators that exhibit a responsive displacement of bound charges, encompassing ions or electrons, under the influence of an externally applied electric field. This charge displacement induces dipole moments, thereby causing polarization to appear within the material. Within the classification of dielectric materials, a subset known as piezoelectric materials manifests a distinct behavior. In piezoelectrics, the application of an electric field results in mechanical strain within the material. Conversely, an externally applied mechanical stress leads to the generation of electric polarization within the material. [5] The properties of materials, be it a crystal, a thin film, or polycrystalline structure, are influenced by their symmetry. Crystals are categorized into 7 crystal systems (triclinic, monoclinic, orthorhombic, tetragonal, rhombohedral, hexagonal, and cubic) with a total of 32 crystal classes. [2, 6] It's important to note that piezoelectric materials have a special crystal structure without a central symmetry point. This limits how they can arrange their crystals to only 20 specific groups that lack a particular type of symmetry called inversion symmetry. [5] These 20 point groups are often referred to as piezoelectric point groups, where the coupling of mechanical stress and electrical energy creates piezoelectricity in the material. [2, 6] In conclusion, material symmetry significantly dictates their properties.

Pyroelectrics are a subgroup of piezoelectrics, which exhibit internal strain due to spontaneous electrical polarization within the crystal. This leads to reversible structural changes of lower symmetry upon heating. These crystals possess a distinct net polarization within their basic unit cell. Only 10 point groups can host net polarization, in accordance with Neumann's principle dictating the alignment of macroscopic properties with the crystal's symmetry. [5]

Ferroelectrics (FE) are a type of pyroelectric materials, which display superior pyroelectric and piezoelectric characteristics when compared to non-ferroelectric materials. (Overview see Figure 1) This material class can reversibly switch between polarization states under an applied electric field, enabling alignment of neighboring (ferroelectric) domains. [2, 5]
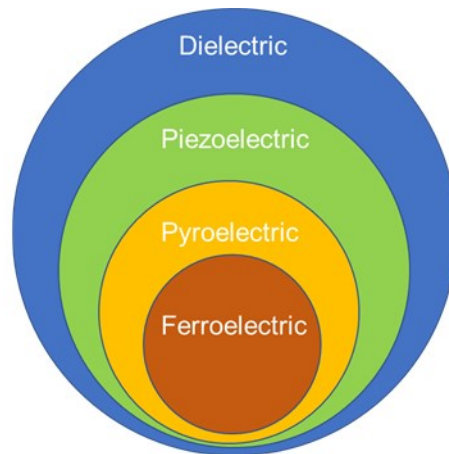
Figure 1: Overview of the dielectric material classes.

The behavior of the domains under the application of an external electric field is illustrated in Figure 2. Ferroelectric domains, are like distinct neighborhoods, where the polarization´s strength and the direction stay consistent. These domains are divided by barriers called domain walls, which prevent from a free domain movement. The walls can be imagined as lines at specific angles dictated by crystal symmetry (e.g. 71° or 109° in a rhombohedral crystal, 90° or 180° in a tetragonal one). Above the Curie Temperature (T_C) a paraelectric behavior is shown. The transition from randomly oriented domains to an ordered ferroelectric structure occurs at T_C. This self-organization takes place to arrange itself in order to minimize the energy level. [2, 7, 8] In the zero-field scenario (Figure 2a), neighboring domain dipole moments are randomly oriented, resulting in a null net polarization due to their canceling effects on a macroscopic scale. In contrast, at the microscopic scale, polarization is present. When an electric field is applied (Figure 2b) polarization at the macroscopic scale occurs.
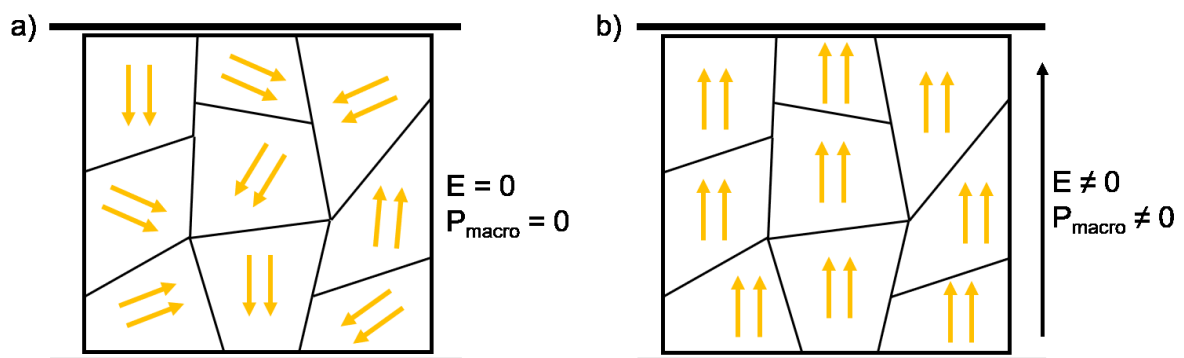

Figure 2: Domain switching behavior of a ferroelectric a) without applied electric field and b) under application of an external electric field.

Experimental confirmation of the ferroelectric effect relies on the capacity to produce a hysteresis loop, illustrating the correlation between polarization and electric field

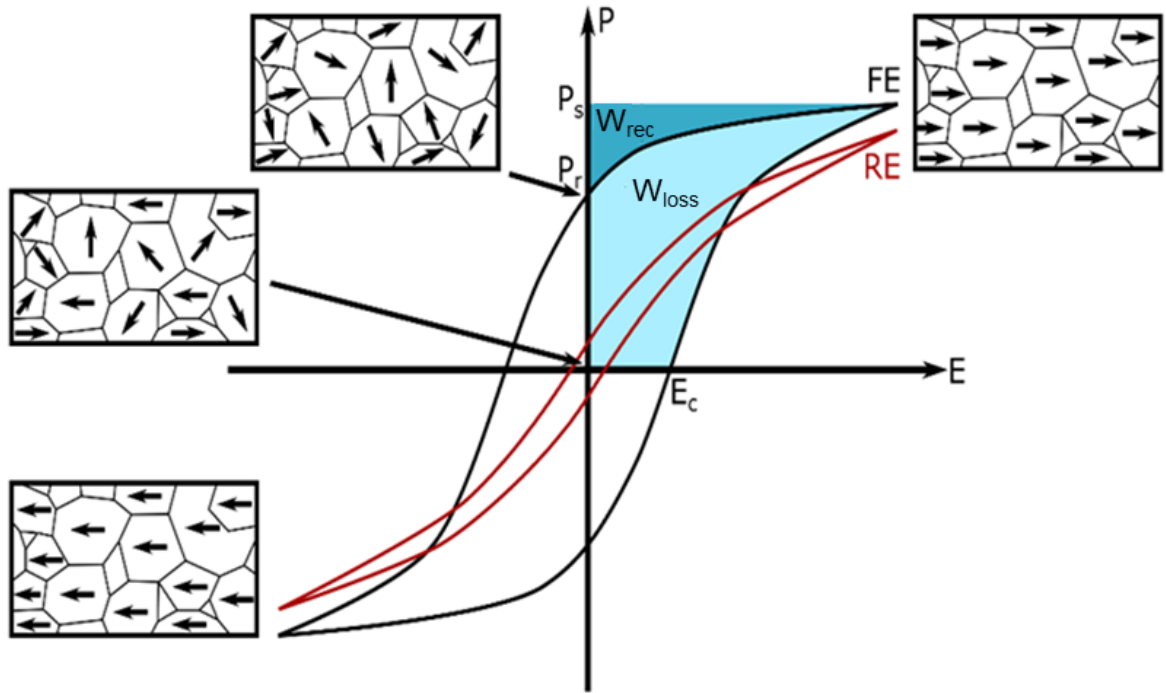cycles. [9] A typical polarization hysteresis loop for ferroelectrics is shown in black (FE) in Figure 3.

Figure 3: Hysteresis loop for ferroelectrics and relaxors.

When a positive electric field surpasses a certain strength known as the coercive field (E_c), the dipole moments align, resulting in a persistent remnant polarization (P_r) even after the field is withdrawn. Conversely, when a negative electric field is applied, the dipole moments switch direction, necessitating a negative coercive field ($-E_c$) for the elimination of net polarization. Upon applying a stronger electric field, the dipole moments complete their switching, leading to the reappearance of net polarization in the ferroelectric material. While aligning the polarization with the applied electric field in the ferroelectric, energy can be stored. Since the appearance of a hysteresis is indicative for a non-linear phenomenon, the standard equation for calculating the stored electric energy that can be recovered from a capacitor (eq. 1) is not valid anymore and changes to eq. 2 [10]:

$$W_{total} = \frac{1}{2}\varepsilon_0\varepsilon_r E^2 \qquad\qquad \text{eq. 1}$$

$$W_{rec} = \int_{P_r}^{P_{max}} EdP \qquad\qquad \text{eq. 2}$$

The region of the Polarization-Electric field (PE) diagram (Figure 3) that is shaded in dark blue represents the energy density that can be regained (W_{rec}). This recoverable energy density (W_{rec}) can be quantified mathematically as the integral of the applied

5

electric field (E) over the measured polarization (P). This integration occurs within the span between the remnant polarization (P_r) and the maximum polarization (P_{max}). [1,7]

Due to the relatively high remnant polarization of ferroelectrics, the energy within the light blue shaded region (W_{loss}) is very large and the recoverable energy density is small. This loss energy is mainly dissipated into heat by elastic energy dissipation through ferroelectric domain switching. [7]

For energy storage applications, the energy storage efficiency (η) is critical and can be computed from the recoverable energy density and the loss energy density using the following formula:

$$\eta = \frac{W_{rec}}{W_{rec} + W_{loss}}$$

eq. 3

FE exhibit higher permittivity but also higher losses attributed to the hysteretic PE loop, as compared to relaxors (RE). The reduced remnant polarization (P_r) of RE materials, in comparison to ferroelectrics, renders RE materials more suitable for energy storage. [1] This is attributed to their high recoverable energy density resulting from their slim PE loops. The relaxor behavior in ferroelectric perovskites is induced by chemical modifications, wherein the substituted cations contribute to the creation of both polar and nonpolar nanoregions. The presence of nonpolar nanoregions disrupts the long-range ferroelectric order, resulting in slimmer loops and reduced hysteretic loss. This occurs because only regions exhibiting ferroelectricity respond to the applied electric field. [11]

In recent years, ferroelectric materials have attracted significant interest owing to their distinctive properties, making them valuable for a variety of modern applications. There are various families of materials that exhibit ferroelectric properties having different structures and characteristics, such as single crystals, polymers as well as ceramics, especially thin films. [7]

Thin film properties differ from bulk materials due to size-effects, resulting often in changes in microstructure, and additional effects from the substrate-film interaction. These effects are mainly the growth phenomena on the surface of the bottom electrode. Also, the strain induced by the bulk substrate in the cooling process of the deposition and the thermal expansion mismatch between the thin film and the substrate play a role. In addition, the nucleation and texture of the thin films are also influenced by the chemical nature, the lattice and microstructure of the substrate. Furthermore, the process tremendously impacts the final properties of the material. Hence, the growth of the ferroelectric materials in thin film form is very complex. [12]

The adoption of this theory influenced the choice to use already available base compositions from ongoing work, $Bi_{0.5}Na_{0.5}TiO_3$ and $NaNbO_3$, for further research, especially on the behavior of the structure as well as the electric properties. In this thesis it was planned to do several process adaptions and variations together with a second material system ($BiMg_{2/3}Nb_{1/3}O_3$) to find the best process conditions for the binary system to provide a starting point for further in-depth research.

2.2 Parallel plate capacitor

In the context of this thesis, the ferroelectric thin films are used in the form of parallel-plate capacitors to probe their electric properties. This section provides a short introduction to capacitors and their characteristics.

A capacitor is defined as an electric component that can store electric energy in a produced electric field. It comprises two conductors – the electrodes - separated by a non-conductive region, which consists of a dielectric material as insulator. [13] Figure 4 shows a typical parallel plate capacitor, which is connected to a voltage source. The positive and negative charges collect on opposite sides of the plates. Electrons move from the positive charge plate to the negative plate, creating a current in the circuit and storing energy in the capacitor.

Capacitance C is defined as the capacity to store a charge q and is expressed by:

$$C = \frac{q}{V}$$

eq. 4

The symbol for voltage is represented by V, and the unit of capacitance is Farad (F).

As already mentioned before and as it can be seen in Figure 4, the two plates of a parallel plate capacitor (I and II) are separated by a dielectric material with a certain thickness d. Consider the electric field and flux density between the plates, denoted as E and D.

$$E = \frac{V}{d} \quad \text{and} \quad D = \frac{q}{A} \quad \text{with} \quad D = E * \varepsilon$$

eq. 5

In this formula, A represents the area of the dielectric, and ε denotes the permittivity of the dielectric material. If you substitute the expression from above ($D = E * \varepsilon$) into $D = \frac{q}{A}$, it yields:

$$E = \frac{q}{\varepsilon * A}$$

eq. 6

It follows:

$$C = \frac{q}{V} = \frac{\varepsilon * A}{d}$$

eq. 7

This results in:

$$C = \frac{\varepsilon_0 * \varepsilon_r * A}{d}$$

eq. 8

ε_0 describes the permittivity of vacuum ($8.854*10^{-12}$ F/m) and ε_r is known as the relative permittivity of the dielectric material.
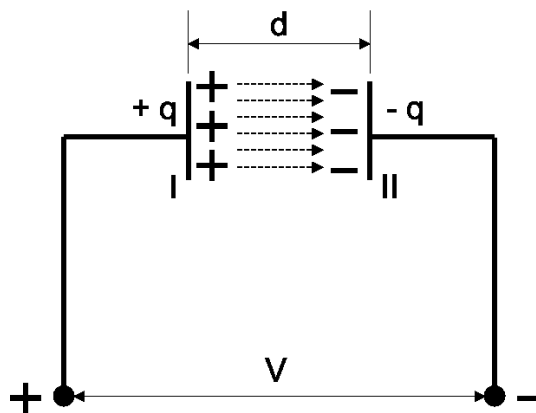

Figure 4: Circuit diagram of a parallel plate capacitor.

In the field of energy storage, there is a need for a combination of high power and high energy density. Ferroelectric materials, especially polycrystalline ceramics, are promising candidates for various applications, including capacitors with high permittivity. [14] A notable example of their application can be found in power electronic inverters, where a variety of high power and energy density buffer devices, known as DC-link capacitors, play a crucial role in compensating for switching current fluctuations. [4]

For all the applications of ferroelectric materials the electric energy of a non-linear capacitor, as explained in the previous chapter, should be considered.

2.3 Chemical solution deposition

Chemical solution deposition (CSD) is a promising alternative to chemical vapor deposition (CVD) and physical vapor deposition (PVD), offering cost-effective and quickly synthesized stoichiometric materials. CSD is particularly valuable in research and development, facilitating efficient exploration of diverse dielectric compositions and properties for material screening. This rapid screening helps to identify optimal dielectric candidates for specific applications, improves the understanding of dielectric properties and enhances the performance of electronic devices. While CSD shows clear advantages in research, its potential for an industrial upscaling is still being explored. In contrast to the dominance of depositing dielectrics with CVD and PVD in large-scale industrial processes, the cost-effectiveness and rapid synthesis capabilities of CSD make it an attractive and interesting option for upscaling efforts, although there is still relatively limited exploration in the industrial context. [15] The most common chemical solution deposition techniques include the sol-gel route, electrodeposition, etc. The process for fabricating thin films through this approach involves the following steps: [16]

• Synthesis of the precursor solution by a chemical route.

• Deposition and application of the final solution by spin-coating or dip coating.

• Low-temperature heat treatment for the drying and pyrolysis of organic species.

• Thermal annealing at higher temperatures to facilitate densification and crystallization of the films into the desired oxide phase. [16]

CSD presents numerous advantages in comparison to conventional physical deposition methods like molecular beam epitaxy (MBE), atomic layer deposition (ALD), and pulsed laser deposition (PLD). All these physical deposition techniques demand highly specific conditions and are conducted under controlled atmospheres to achieve high-quality thin films. Films produced through CSD are typically chemically homogeneous, given that precursor solutions facilitate the effective mixing of diverse cations. This chemical homogeneity stands as a highly appealing feature of CSD. Furthermore, it is scalable, cost- and time-efficient, and versatile in terms of the precursor components and solvents that can be employed. [16, 17] A possible drawback of CSD with respect to MBE, ALD and PLD is the difficulty of obtaining epitaxial films, although recent studies demonstrated also epitaxial growth of perovskite films with CSD. [18]

Additionally, using this method allows for precise control over the microstructure of the deposited films, including factors such as pore size, pore volume, and surface area. [19] The ease of tailoring of a wide array of processing parameters also enables

precise control over the nucleation and growth process making this method highly adaptable for synthesis. [15, 16]

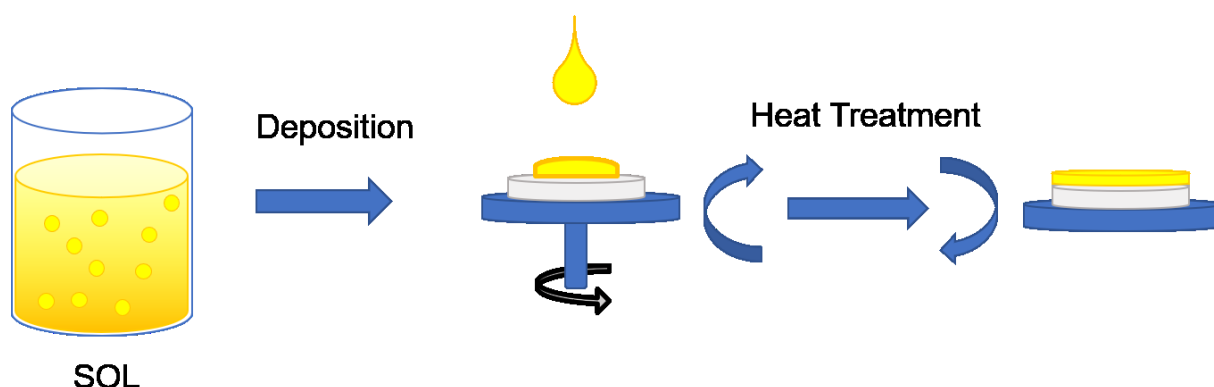The CSD deposition route is illustrated in Figure 5.

Figure 5: Simplified scheme of Chemical Solution Deposition (CSD) Route with spin coating deposition.

Subsequently a more detailed explanation of the single steps: the first step of the CSD method is preparing a stable precursor solution. A sol is a colloidal suspension characterized by solid particles dispersed in a liquid medium. [16] The hydrolysis of the precursor molecules (typically, metal alkoxides) and the condensation between reactive species that occur during this process are the fundamental reactions of the sol-gel process. The processes involved and the properties of the precursor molecules significantly influence the resulting material properties. During hydrolysis, the metal alkoxides react with water, which leads to the elimination of alcohol molecules and the formation of MOH groups: [15]

$$M(OR)_n + H_2O \rightarrow M(OR)_{n-1}OH + ROH \qquad \text{eq. 9}$$
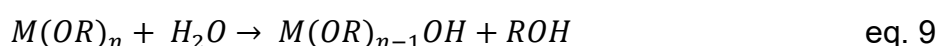
This formula illustrates the partial breakdown of a metal alkoxide with water. Comparable reactions can be formulated for metal carboxylates, but this group displays significantly greater resistance to hydrolysis. In practice, precursor molecules that have undergone partial hydrolysis and contain MOH groups can undergo condensation by eliminating water:

$$(RO)_mM - OH + HO - M(OR)_m \rightarrow (RO)_mM - O - M(OR)_m + H_2O \qquad \text{eq. 10}$$
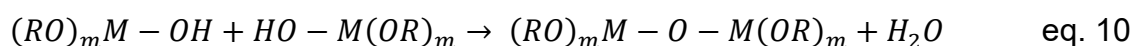
The dimer evolves into trimers, tetramers, and other oligomers through an inorganic polycondensation reaction, ultimately forming particles. Depending on the solvent, a distinction is made between alcoholic sols and hydrosols. Hydrolysis and condensation represent dynamic reactions involving multiple interconnected equilibria, influenced by catalysts like acids or bases. Sol particles may contain significant amounts of unhydrolyzed alcoholate, carboxylate, or diketonate groups. Progressive particle

growth and the aggregation of sol particles into secondary particles lead to increased viscosity. Such "aging" of coating sols can adversely affect industrial production. [15] When a network of sol particles forms between the walls of the reaction vessel, gelation occurs, i.e. the originally viscous sol is transformed into a viscoelastic solid. The gel consists of the gel mesh and the solvent that surrounds it, with all pores connected to each other in an "interpenetrating network". The exact determination of the gelation time is a challenge, as it is also influenced by the vessel size and rheological measurements can significantly affect the development of the network. [15, 20]

Commonly, solvents such as 2-methoxyethanol, methanol, and modifying ligands like acetic acid and acetylacetone find use in the process. [15, 20] Synthesis relying on 2-methoxyethanol is extensively documented due to its notable stability in precursor solutions. This stability minimizes the influence of aging, thus ensuring superior control and reproducibility. This solution is derived from metallo-organic compounds dissolved in suitable solvents, and furthermore blended in a stoichiometric ratio to achieve the intended composition of the final oxide film. [15]

In the subsequent stage, the sol is deposited onto a substrate using various coating procedures. The most widely used methods for this purpose include spin coating, spray coating, and dip coating. [15, 20] In the spin coating process, a small quantity of the solution is dispensed onto the substrate using a syringe. The substrate undergoes high-speed rotation to achieve a uniform film with consistent thickness (Figure 5). Vacuum suction on the back secures the substrate in place. The concentration and viscosity of the precursor solution, along with processing parameters like rotation speed and duration, play crucial roles in determining the thickness and quality of the resulting oxide film. [16, 17]

Following deposition, the film undergoes a sequence of treatments involving drying, pyrolysis, and crystallization. Drying is generally executed on a hot plate, while pyrolysis and annealing on a conventional rapid thermal annealing (RTA) furnace, depending on the desired thermal processing route. [16, 17]

The film thickness can be enhanced by iteratively applying of the deposition and thermal processing sequence. [21] A final thermal treatment of the film at a higher temperature may be necessary to enhance crystallinity, refine the microstructure, or facilitate densification. [16, 17] Typically, a two-step or a one-step process is employed. In the one-step process, both organic removal and crystallization take place in a single processing step conducted at temperatures sufficiently high to induce oxide crystallization (> 600°C). In the two-step process, the elimination of the majority of organic constituents occurs in a distinct processing step at lower temperatures, around 200°C – 400°C, before the high-temperature crystallization.

In the CSD process, the crystallization of the films typically undergoes a nucleation and growth mechanism. Nucleation, the initial phase of crystallization, can occur either homogeneously (Figure 6a) or heterogeneously (Figure 6b) at the substrate interface. This choice significantly shapes the ultimate microstructure and properties of the metal oxide film. [15, 20] In homogeneous nucleation, grains initiate growth from the inner part of the film and eventually, after time- and temperature-dependent processes, form a granular structure (Figure 6c), where the grains can also merge into larger grains. When heterogeneous nucleation occurs at an interface, it often results in the development of a uniform and columnar microstructure (Figure 6d). This specific nucleation pattern can be advantageous for the film's properties, particularly if the lattices of the substrate and the film are compatible, leading to a preferential crystallographic orientation (texture). However, it must be mentioned that during real heating over a definite time interval, different phases of the material can nucleate and change or intermix the ongoing nucleation mode. Therefore, the heating program in CSD is an important factor and the heating rates need to be in the °C/s range – compared to °C/min in conventional sintering – to minimize the time frame of unknown behavior and favorize the wanted high-temperature perovskite phase. [15]
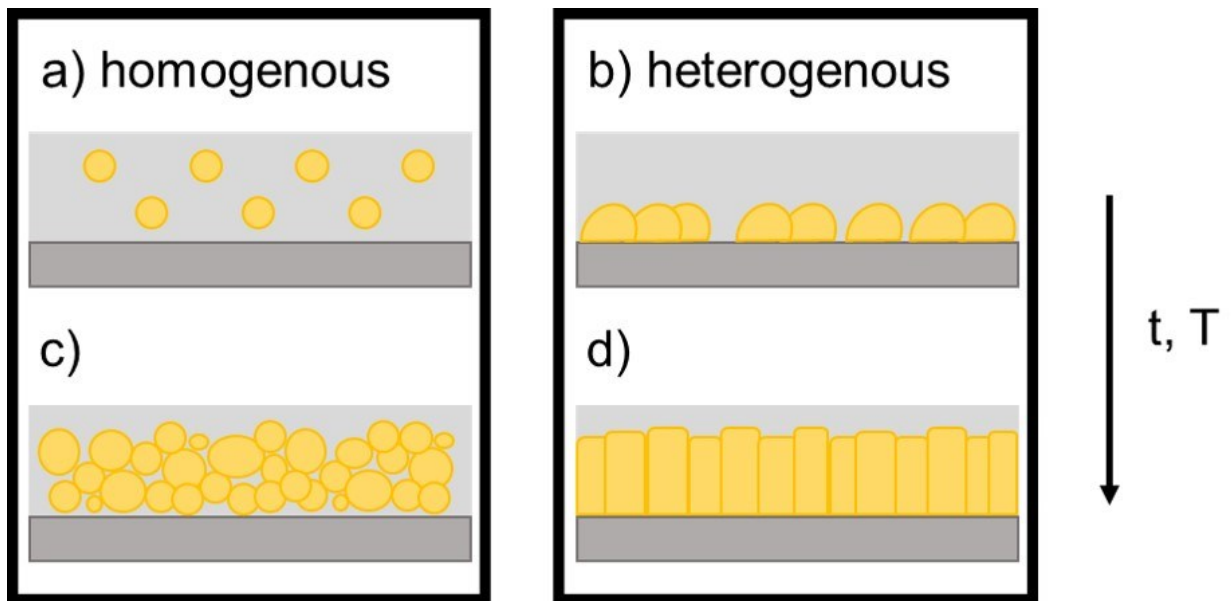

Figure 6: Schematic growth mode of a sol-gel thin film over time and temperature: a) homogenous, b) heterogenous, c) granular and d) columnar.

In Figure 7 the relationship between nucleation and growth concerning temperature is shown. As observed, nucleation initiates at lower temperatures, whereas growth begins at higher temperatures. Therefore, a general trend at higher temperatures would entail the presence of larger grains or increased grain sizes. Typically applied crystallization temperatures ($T_{cryst.}$) for CSD thin films are below 850°C compared to bulk materials. However, these temperatures are far below the melting temperature T_m

of bulk ceramics, which are typically around 1500°C. Therefore, the CSD process is primarily nucleation-driven. Growth can mainly be achieved by expanding the holding time but also can lead to volatilization of certain compounds, for example alkaline metals, and deteriorate the stoichiometry. At higher temperatures the substrates need to be tailored to the material to prevent interdiffusion, formation of intermetallic phases and delamination of the different layers because of lattice mismatch and resulting stress. Although there is already ongoing research on optimizing substrates for CSD thin films, it is not beneficial to change the substrates according to the film as this limits tremendously its applicability in standard semiconductor processing. [22, 23]
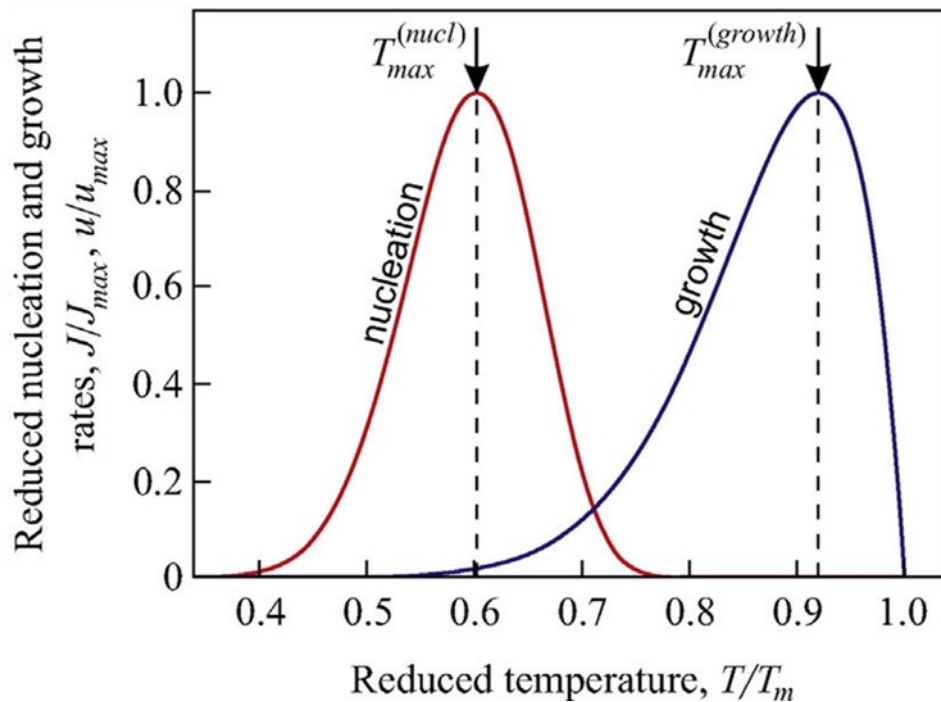

Figure 7: Nucleation and growth rate over temperature. [24]

In general, it can be said that the influence of the heating rate (HR) on the microstructure is relatively small compared to the temperature. This observation is attributed to the presence of a non-equilibrium phase and the specific characteristics of a process driven by a diffusion barrier. Also, the nucleation process is significantly influenced by decomposition reactions and the conditions during annealing. Understanding and controlling these factors are essential for tailoring the microstructure and properties of metal oxide films produced through the CSD method. Hence, the optimal CSD procedure and thermal processing strategy depend on the specific metal oxide under consideration, as well as the chemistry of the precursors and solvents involved. [15]

The thermodynamic driving force for the crystallization process, which is defined by the difference in free energy (ΔG_v) between the amorphous and crystalline phases, is a significant factor that influences the overall nucleation and growth dynamics. This

driving force serves as a critical catalyst for triggering nucleation processes and forms the basis for the subsequent growth process. Ultimately, the interplay of these thermodynamic factors significantly shapes the microstructure of the resulting crystalline film and determines the unique characteristics and properties of the material. [15]

In Figure 8, the behavior of the free energy is illustrated. The green curve represents the total free energy ΔG plotted against the radius of a particle (assuming constant pressure). The total free energy combines two terms: the first, depicted in red, is a bulk term that scales with volume and is consistently negative. The second term, shown in blue, is an interfacial term and constitutes the barrier's origin. It is always positive and scales with surface area. The graph displays the free energy barrier, ΔG^*, and the associated critical radius, r*. This critical radius sets the particle radius at which the derivative of ΔG equals zero and marks the point at which the influence of the volume free energy ΔG_v starts to overcome the influence of the surface free energy ΔG_s on the free energy ΔG. If a particle has a radius below the critical radius it cannot survive in solution without being re-dissolved. Above r* a nucleated particle can survive and grow because it is thermodynamically favored. [25]
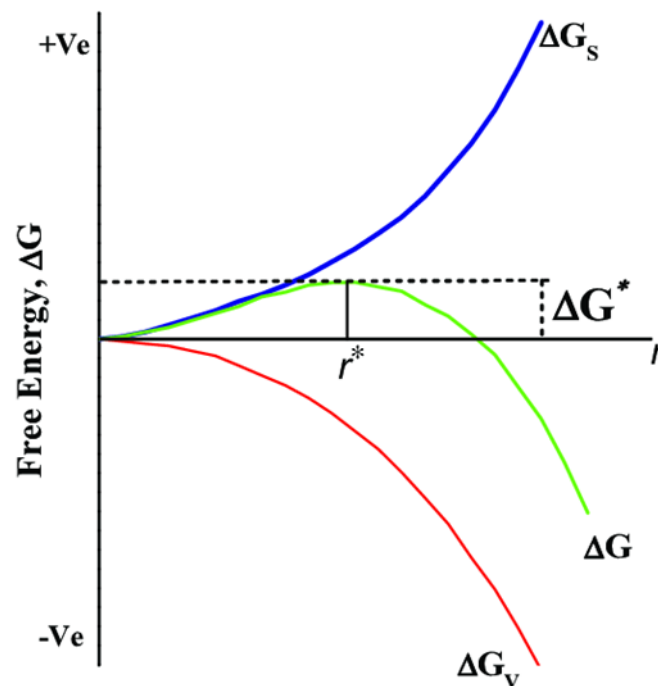

Figure 8: Free energy as a function of the radius. [26]

2.4 Characterization methods

The different characterization techniques used are briefly discussed in the following subsections.

2.4.1 Raman spectroscopy

Raman spectroscopy is a spectroscopic technique employed for the determination of vibrational modes in molecules. While it primarily focuses on vibrational modes, it can also capture rotational and other low-frequency modes within a system. Raman spectroscopy is based on the principle of inelastic scattering of photons, a phenomenon known as Raman scattering. It involves the use of monochromatic light, often emitted by a laser in the visible, near-infrared, or near-ultraviolet range. The laser light interacts with molecular vibrations, the phonons, or other excitations within the system, causing a shift in the energy of the laser photons. This energy shift provides valuable information about the vibrational modes present in the system. [27] In normal Stokes-Raman scattering, molecules gain vibrational energy as incident photons from a visible laser shift to lower energy. During Raman spectroscopy, a laser beam illuminates the sample, and the electromagnetic radiation emitted from the illuminated spot is collected using a lens. This collected light is then directed through a monochromator. Elastic scattered radiation at the laser line's wavelength, which is known as the Rayleigh scattering, is filtered out using a notch filter or edge pass filter. The remaining light is dispersed onto a detector for analysis. [28]
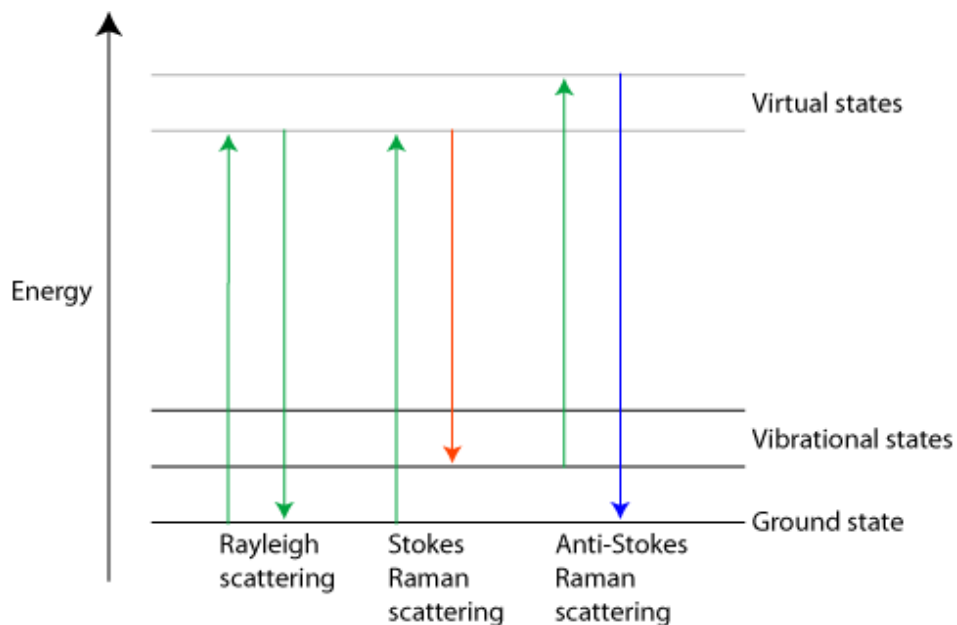

Figure 9: Raman scattering. [29]

In Figure 9 the different possibilities of light scattering are displayed. Light scattering occurs in different ways, with each type of scattering revealing different interactions between photons and matter. Rayleigh scattering, where no energy exchange happens, occurs when incident and scattered photons have the same energy level. In Stokes-Raman scattering, atoms or molecules absorb energy, resulting in the scattered photon having less energy than the incident photon. In Anti-Stokes Raman scattering, on the other hand, the atoms or molecules lose energy, so that the scattered photon has more energy than the incident photon. These different scattering phenomena provide valuable insights into the dynamic interplay between light and matter. [30, 31] It should also be noted that the x-axis of a Raman spectra represents a Raman shift and not the actual wavelength. This ensures comparability, even when different lasers are used.

2.4.2 Scanning electron microscopy

A scanning electron microscope (SEM) utilizes a focused electron beam to scan a sample's surface, generating signals that reveal information about the sample's topography and composition. The electron beam, scanned in a raster pattern, interacts with atoms in the sample, and the emitted electrons or photons are detected to produce an image based on different contrast mechanisms. SEMs can achieve resolutions lower than 1 nm. Specimens are observed in high vacuum or under various environmental conditions, such as low vacuum or wet settings, and at different temperatures. [32] A SEM generates signals for imaging through electron beam interactions with atoms at different depths in the sample. These signals include secondary electrons (SE), back-scattered electrons (BSE), characteristic X-rays, cathodoluminescence (CL), absorbed current, and transmitted electrons. The most common detectors in SEMs are the secondary electron detectors. [32] As secondary electrons are emitted from atoms in the analyzed material, they expend a portion of the excitation energy as the work function for their release. Consequently, these secondary electrons carry relatively low kinetic energy, and only electrons from the top few nanometers can travel to the detector from the sample. [32] This can be also seen in Figure 10. Since these electrons have low energy they only carry morphological information. Contrary to that BSE, which have higher energy are elastically scattered at the nucleus and therefore larger nuclei deflect the incident electrons more than lighter ones, leading to a contrast mechanism based on the atom number.

SEM often allows the recording of X-ray emission spectra using an energy-dispersive spectrometer (EDX). EDX is an analytical technique for elemental analysis, relying on X-ray emission and the unique atomic structure of each element, which produces distinct peaks in the emission spectrum. EDX is employed to identify the chemical

elements present in a sample and estimate their relative abundance. Additionally, it aids in measuring the thickness of multi-layer coatings on metallic surfaces and analyzing different alloys. [33] Typically, X-rays from the top 2 µm of a material can reach the detector. Both individual spectra from selected sample points and EDX images of entire areas can be captured, representing the distributions of chemical elements (see Figure 10).
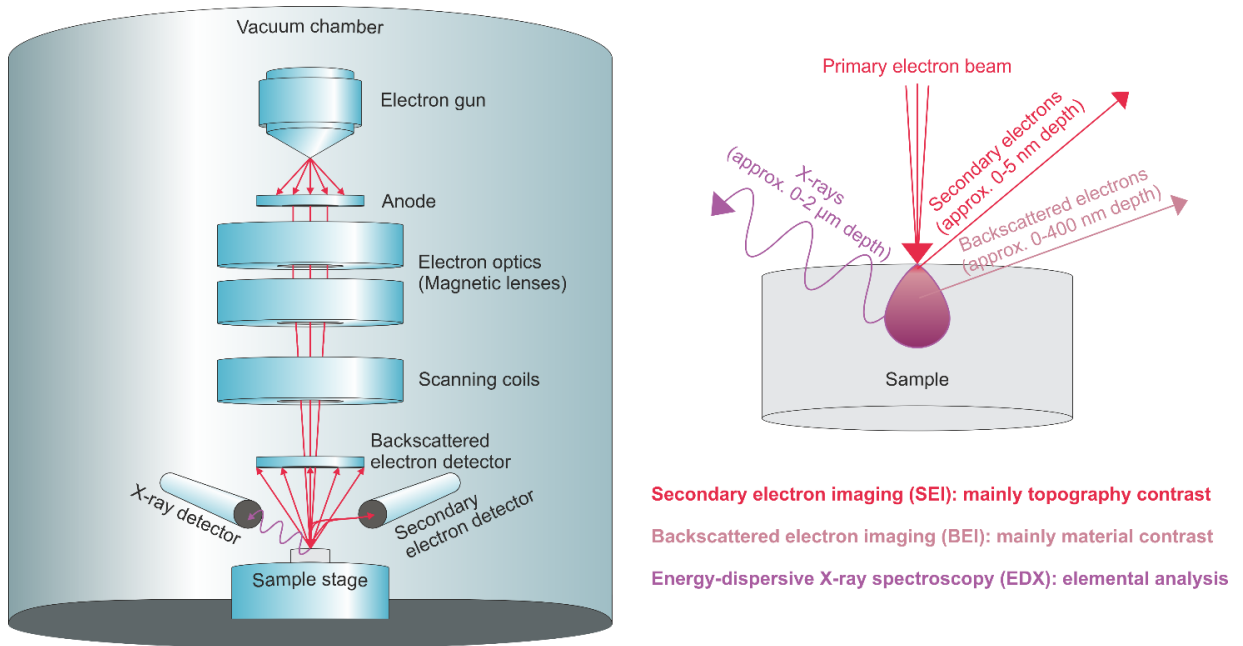

Figure 10: Working and detecting principle of a SEM. [34]

2.4.3 X-ray diffraction

X-ray diffraction (XRD) is an experimental scientific method used to determine the atomic and molecular structure of a crystal. In this technique, the crystalline structure causes an incident X-ray beam to diffract into specific directions. By measuring the angles and intensities of these diffracted beams, a crystallographer can generate a three-dimensional representation of the electron density within the crystal. This electron density information allows the determination of atomic positions, chemical bonds, crystallographic disorder, as well as various other details about the crystal. [35] Diffractometers are versatile and operate in both transmission and reflection mode, with reflection mode being the most widely used. In the Bragg-Brentano θ-2θ configuration, a sample is placed in a sample holder and tilted by an angle θ around an axis as it can be seen in Figure 11 a). At the same time, a detector rotates around the sample at an angle twice as large (2θ). This configuration is contrasted with the GIXRD configuration, where the detector doesn´t rotate in comparison to the sample, and the incidence beam is kept at a fixed value. [35, 36] The main reason for using

GIXRD in the frame of this study was to minimize the collection of excessive information coming from the substrate, avoiding collection of the signal from the whole volume.
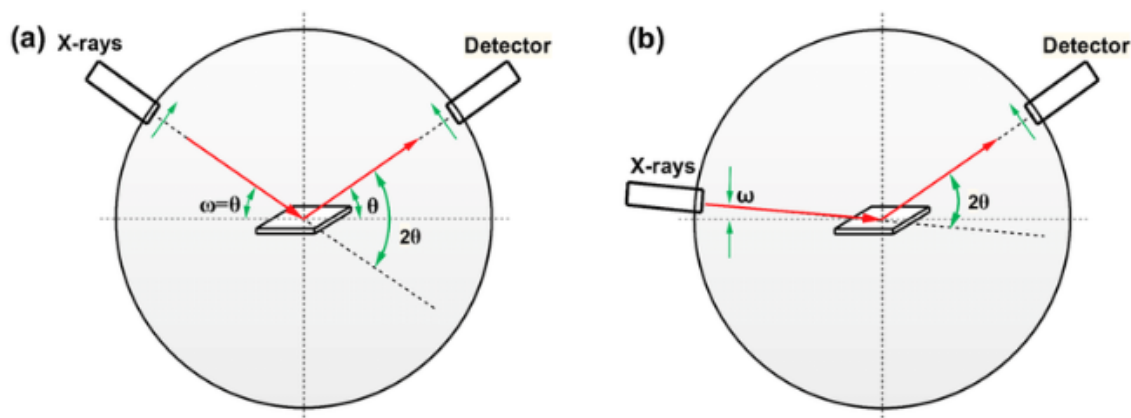

Figure 11: Scheme of (a) Bragg-Brentano (θ - 2θ) and (b) GIXRD geometry. [37]

Thin films serve as excellent model systems for studying electroceramic materials. With well-defined geometries and microstructures that can be customized through fabrication or post-treatment conditions, thin films offer an essential approach to exploring interfacial, microstructural, or confinement effects in oxides. Additionally, more intricate thin film structures, including multilayers, nanocomposite films, layers with graded compositions, and ultimately superlattices, can be engineered. [38]

Thin films exhibit notable differences in physical and chemical properties compared to their bulk ceramic counterparts. These distinctions, influenced by growth conditions during fabrication, encompass factors like thickness, surface roughness, grain sizes, texture orientations, crystallinity, strains/stresses, and compositional variations. These differences are often linked to the growth conditions during fabrication and have a substantial impact on functional properties. Thus, understanding the structure is crucial for tailoring growth conditions and engineering the functional properties, establishing a growth-structure-function relationship within film engineering which can be done by in depth XRD analysis. [38]

2.4.4 Electric characterization

Evaluating the performance of ferroelectric materials under the conditions relevant to the intended applications is becoming more and more important. [39] Firstly, a number of factors need to be considered. In addition to the current magnitude, understanding the bandwidth of the current is crucial for the choice of recording method. The frequency spectrum of the current defines the bandwidth requirements for the

recording amplifier and influences the choice of amplifier. Noise and ground bouncing play an important role in estimating the signal-to-noise ratio (SNR) and have an overall impact on the accuracy of the evaluation of the electrical properties of a piezoelectric or ferroelectric capacitor. There are established methods for recording the charge and current response of the sample.

The electric properties could be measured by using the classic Sawyer-Tower circuit. The Sawyer Tower measuring circuit uses a charge measurement method with a reference capacitor in series with the ferroelectric capacitor. To account for the reverse voltage effect, the reference capacitor must be much larger than the measured capacitor. The reference capacitor must be reset for each sample and the method is limited by cable reflections at high speeds. Parasitic effects, such as cable capacitance, can affect measurements, especially with small capacitors, and obtaining accurate reference capacitors is a challenge due to tolerance issues. [40, 41]
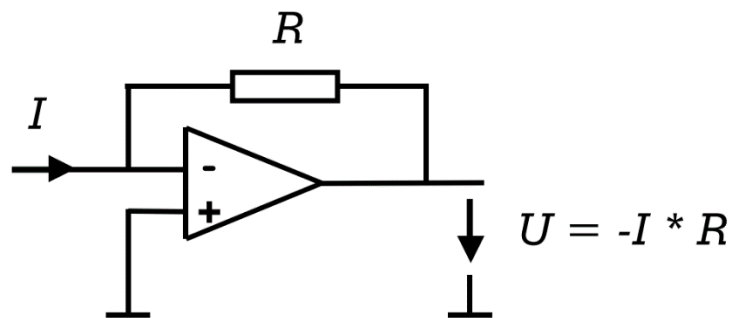

Figure 12: Principle of the Virtual Ground feedback method. [41]

An alternative option involves measuring with the virtual ground method. In this method a current-voltage converter with an operational amplifier and a feedback resistor is used for the current measurement (see Figure 12). The output of the converter is connected to the inverting input of the operational amplifier via a feedback resistor, while the non-inverting input is earthed. This effectively grounds the inverting input, which is advantageous for measuring small capacitors and attenuating cable capacitance effects. The method ensures that the sample is continuously exposed to the full excitation voltage without reverse voltage. For high-speed measurements, however, potential reflections and the characteristics of the operational amplifier must be considered. Overall, the virtual ground method offers high precision for ferroelectric measurements.

3 Preparation of the samples

This section provides a detailed overview of the entire preparation process for the BMN-based thin film samples.

3.1 Sol-gel route

The precursor solution preparation was carried out within a Glovebox (GB1200-E, SylaTech GmbH, Walzbachtal, Germany). At the beginning a solution for the first single system $BiMg_{2/3}Nb_{1/3}O_3$ was prepared. Initially, a series of trials have been required to generate a stable precursor solution of $BiMg_{2/3}Nb_{1/3}O_3$.

For the synthesis of the final $BiMg_{2/3}Nb_{1/3}O_3$ solution, two sub-solutions *(A)* and *(B)* with different solvents are prepared. Sub-solution *(A)* is based on acidic acid to facilitate dissolving the acetate precursors. For this solution *(A)* and aiming for a final concentration of c = 0.3 mol/l, 2.3869 g of Bismuth(III)acetate ($C_6H_9BiO_6$, 99%, Fisher Scientific, Sweden), with an excess of 2%, was dissolved in 9 ml of acetic acid (AcOH) ($C_2H_4O_2$, 100%, Carl Roth, Germany) in a beaker. Then, 0.9007g of Magnesium acetate tetrahydrate ($Mg(CH_3COO)_2$)*4 H_2O, 98%, Carl Roth, Germany) calculated with an excess of 5%, as well as 0.0149g Manganese acetate ($Mn(CH_3COO)_2$ * 4 H_2O, 99%, Sigma Aldrich, USA) was added. The solution *(A)* was stirred for 1h at 80°C, also a few drops of ammonia (NH_3, 28-30%, Merck, Germany) have been additionally added, to adjust the pH and to get a clear and stable solution. 0.6304g of Niobium-ethoxide (99.95%, Sigma Aldrich, USA) was dissolved in 0.4005 g of Acetylacetone (AcAc) ($C_5H_8O_2$, 99%, Sigma Aldrich, USA) in a second flask to produce a solution *(B)*, based on the solvent 2-Methoxyethanol (MOE). The solution was left for stirring 5 min at room temperature, after that 5 ml of 2-Methoxyethanol ($C_3H_8O_2$ 99%, Carl Roth, Germany) was added and again it was left for stirring at room temperature for an hour. Once both precursor solutions, *(A)* and *(B)*, were homogenous, the solution *(A)* was added to the solution *(B)* and 1 ml of MOE was used to rinse the flask as well as to reach the correct stoichiometry. The mixed solution was again left for stirring for 2 hours at room temperature. In the end the solution was transferred into a graduated cylinder and AcOH:MOE in a ratio of 3:2 was added to achieve the correct stoichiometry and volume.

For the preparation of the final solutions $BiMg_{2/3}Nb_{1/3}O_3$-$Bi_{0.5}Na_{0.5}TiO_3$, as well as $BiMg_{2/3}Nb_{1/3}O_3$-$NaNbO_3$, the procedure was based on the processing of the BMN solution with some adaptations. It must be noted that all the materials have a B-site substitution of 1 mol% Mn to reduce leakage currents, and this will not be mentioned

20

separately anymore throughout the thesis. [42, 43] The preparation route for all the produced BMN-based precursor solutions is displayed in Figure 13.

First the detailed description of the solution production of $0.15Bi(Mg_{2/3}Nb_{1/3})O_3$-$0.85(Bi_{0.5}Na_{0.5})TiO_3$ (BMN-BNT):

For the preparation of solution *(A)*, a precise quantity of 1.3725 g of Bismuth(III)acetate (2% excess) was dissolved in 9 ml of AcOH for a concentration of c = 0.3 mol/l. This dissolution process aimed at ensuring the uniform dispersion of the Bismuth(III)acetate in the AcOH solvent. Following this, 0.1351 g of Magnesium acetate (5% excess), 0.2324 g of Sodium acetate (99%, Carl Roth, Germany) (10% excess) and 0.0149 g of Manganese acetate were meticulously added to the solution.

The ensuing mixture underwent a thorough stirring process for 1 hour at 80°C, during which the temperature was carefully controlled. To fine-tune the chemical environment and guarantee a clear and stable solution, an addition of a few drops of ammonia was made, serving the dual purpose of adjusting the pH and promoting solution clarity.

In parallel, a separate flask was employed to prepare solution *(B)*. In this process, 0.0946 g of Niobium-ethoxide were meticulously dissolved in 0.0601 g of AcAc. Additionally, 1.4794g of Titanium isopropoxide ($Ti(C_{12}H_{28}O_4)$, 97%, Sigma Aldrich, USA) were dissolved in 1.0212 g of AcAc and added, in contrast to the first single BMN-solution, to the solution *(B)*. Following an initial 5-minute stirring period at room temperature, 5 ml of MOE were introduced into the solution. The subsequent hour of stirring at room temperature allowed for the complete integration of the components. Upon achieving homogeneity in both precursor solutions, the judicious combination of solution *(A)* with solution *(B)* was executed. To ensure the preservation of stoichiometric ratios and uniformity, an additional step involved the use of 1 ml of MOE to rinse the flask and adjust the mixture. The solution underwent a further 2 hours of stirring at room temperature, promoting thorough mixing and chemical interaction.

In the final step, the resulting solution was carefully transferred into a graduated cylinder. To achieve the desired stoichiometry and volume, an addition of a mixture of AcOH to MOE in precise ratio of 3:2 was performed. This intricate procedure aimed at ensuring the successful synthesis of the desired chemical solution with precision and reproducibility. For a better overview all the calculated masses for the used chemical components can be found and are summarized in Table 1.

Table 1: List of calculated masses for sol-gel-route of BMN-BNT

Chemical component	Mass [g]	n [mol]	M [g/mol]
Bi-acetate	1.3725	0.58	386.112
Na-acetate	0.2324	0.43	82.030
Mg-acetate	0.1351	0.10	214.460
Ti-isopropoxide	1.4794	0.84	284.220
Nb-ethoxide	0.0946	0.05	318.209
Mn-acetate tetrahydrate	0.0149	0.01	245.090
Acetylacetone for Nb	0.0601	0.10	100.120
Acetylacetone for Ti	1.0212	1.68	100.120

For the material system $0.22Bi(Mg_{2/3}Nb_{1/3})O_3$-$0.78NaNbO_3$ (BMN-NN) the same procedure and manganese substitution as for BMN-BNT was used, just with some small deviations.

The preparation of solution *(A)* was done the same way as for the system BMN-BNT, with the only modification that for this solution no addition of ammonia was needed, due to the small amount of Bismuth(III)acetate used. For the mixing of solution *(B)* Niobium-ethoxide was dissolved in a flask in AcAc. An overview of the used amounts of chemicals for this synthesis route to attain a concentration of c = 0.3 mol/l and a volume of V = 20 ml can be seen in the table below. (Table 2)

Table 2: List of calculated masses for sol-gel-route of BMN-NN.

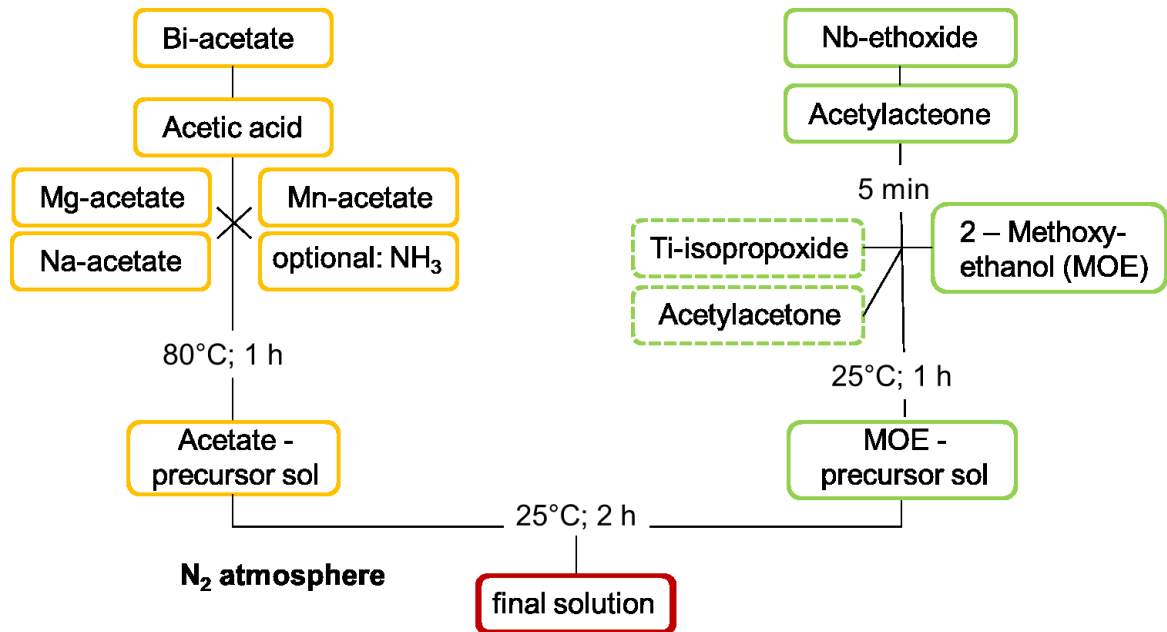| Chemical component	Mass [g]	n [mol]	M [g/mol]
Bi-acetate	0.5251	0.22	386.112
Na-acetate	0.4266	0.78	82.030
Mg-acetate	0.1982	0.15	214.460
Nb-ethoxide	1.6137	0.84	318.209
Mn-acetate tetrahydrate	0.0149	0.01	245.090
Acetylacetone	1.0252	1.69	100.120

Figure 13: Sol-gel route of BMN-based precursor solutions.

3.2 Thin film preparation

Thin films were produced on Pt/TiO$_2$/SiO$_2$/Si substrates with 1x1 cm^2 size, sourced from SINTEF AS (Trondheim, Norway). The whole deposition process and thermal treatment ensued in ISO7 cleanroom environment (ISO5 for the spin-coating). A careful spin cleaning step with once spinning with DI-water and another three times spinning rounds with isopropanol, followed by 5 min drying at 200°C on the heating plate, was employed to ensure a clear surface. The substrates emerged with heightened wetting properties, thus improving subsequent depositions.

Spin coating was carried out in ISO5 Laminar FlowBox (Kojar Tech Oy Blue Series Technologies, Mänttä-Vilppula, Finland) to reduce any contamination of the thin films. The precursor solutions of BMN-BNT and BMN-NN were applied onto the 1x1 cm^2 substrates using a syringe equipped with a 0.2 µm PTFE-filter to avoid solution contamination and large particles. Once the solution is on the substrate, during spin coating it should spread evenly and wet the surface of the substrate. Spin coating was performed with a Spin Coater Spin150i (SPS-Europe GmbH, Ingolstadt, Germany) at 4000 rpm for a duration of 30 s, with an acceleration rate of 2000 rpm/s.

In the earlier sections, it was mentioned that the heat treatment process is considered as a very important step in shaping the microstructure of the films and controlling the way the films crystallize. In the frame of this work, a three-step process has been utilized to accomplish the crystallization of the films. The whole process took place in a Rapid Thermal Annealer Oven (MILA 5050, ULVAC GmbH, Kirchheim bei München,

Germany). The drying process was conducted at a temperature of 200°C with a 10 °C/s ramp in 100% oxygen for 2 minutes. The pyrolysis step was performed at a temperature of 450°C, and also with a 10 °C/s ramp in 100% oxygen. The pyrolysis process lasted 5 minutes for solvent evaporation and elimination of the organic species. The films were then crystallized in the furnace at 750°C, 700°C, 680°C and 650 °C in 100% oxygen conditions. Different heating rates for the crystallization step were explored. For each annealing/crystallization temperature 1 °C/s, 10 °C/s and 30 °C/s heating step ramps were applied. A uniform cooling rate (1 °C/s) was chosen to cool down the films from the different annealing temperatures back to room temperature. The effect of long and short heat rates on the microstructure of the films is discussed in the following chapters. The deposition as well as the annealing process were repeated 5 times, to reach a final thickness of approximately 200 nm for all the deposited films. The complete thin film deposition process is outlined in Figure 14.
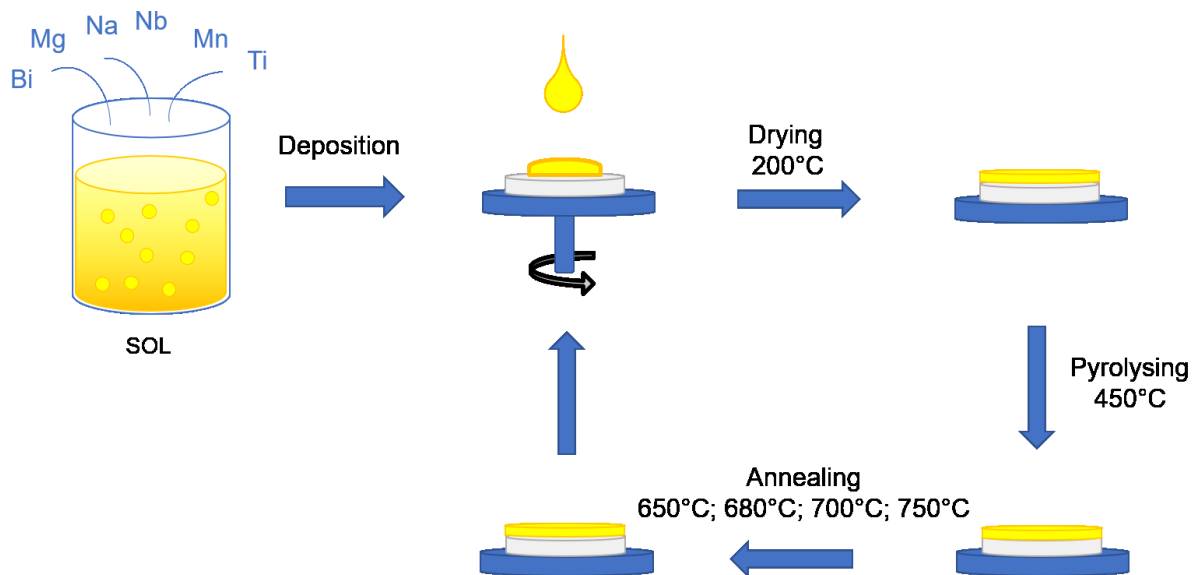

Figure 14: BMN-based thin film deposition route.

3.3 Electrode deposition and capacitor structure

Metal-insulator-metal (MIM) capacitor structures, specifically configured as Au/Cr/BMN-BNT/Pt, as well as Au/Cr/BMN-NN/Pt, were fabricated to allow electrical measurements of the thin films. The fabrication process involved the precise deposition of circular Au/Cr top electrodes onto the thin film surfaces. This deposition was accomplished using advanced e-beam-assisted evaporation technology (HEX Series TAU, Korvus Technology, United Kingdom). The deposition process was finely tuned and controlled with the aid of a shadow mask with a large radial electrode diameter of 1 mm. This strategic design aimed to optimize the electrical characteristics and

performance of the capacitor structures, ensuring accuracy and reliability in subsequent electrical measurements.

Before the entire electrode deposition process, a cleaning procedure was implemented for the samples to ensure optimal conditions. The initial step involves purging the samples with an N_2-gun to effectively remove any dust or particles from the surface. Following this, a comprehensive cleaning is carried out using acetone, with the samples immersed in the solvent for approximately 5 minutes. Subsequently, a thorough rinse in isopropanol for an additional 5 minutes is performed to eliminate any remaining impurities. To conclude the cleaning process, the samples undergo a final drying stage using the N_2-gun and a heating plate at 200°C, ensuring that they are completely free from contaminants and ready for the subsequent electrode deposition steps.

The deposition process was conducted using the Korvus Technology's evaporator HEX Series Tau, employing an e-beam, at a pressure of ~$5*10^{-6}$ mbar. First, chromium (Cr) as adhesion layer was evaporated at a deposition rate of 0.6 Å/s (P = 75 W) to yield a thickness of 10 nm, followed by the evaporation of gold (Au) with a rate of 1.3 Å/s (P = 168 W) to deposit 200 nm Au. Using Au as top electrodes presents challenges due to its non-optimal adhesion to oxides. This drawback can result in the delamination of top electrodes, leading to the premature failure of the energy storage device. Conversely, Cr is known for its strong adhesion to oxide surfaces and thus was used as adhesion layer here.

For measuring the parallel plate capacitor, a bottom electrode contact is essential. This contact was created by gently scratching one edge of the thin film sample and applying a small amount of silver paste. The subsequent step involved drying the sample on a heating plate at 200°C for a duration of 30 minutes. Since the films have nm thickness, a large aspect ratio of 5000 between electrode diameter and film thickness is achieved. Figure 15 displays an image of the produced parallel plate capacitor structure.
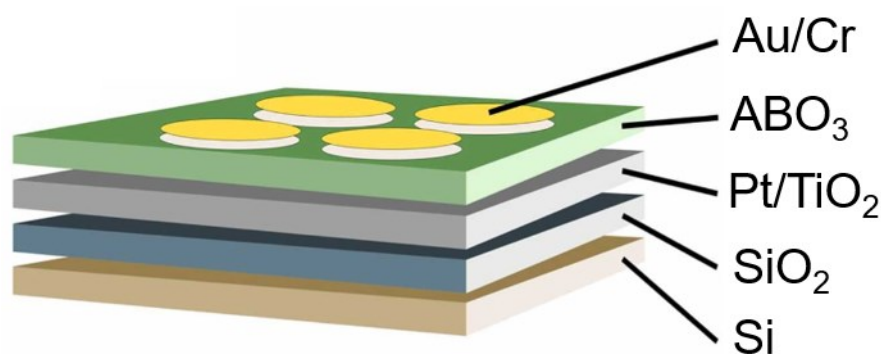

Figure 15: Metal-insulator-Metal (MIM) capacitor structure. [4]

3.4 Characterization

The thin films underwent crystallographic and phase analyses by Grazing Incidence X-ray diffraction (GIXRD) method on Bruker D8 Advance (Karlsruhe, Germany) equipment using Cu-Kα radiation at 40 kV accelerating voltage and 25 mA current. The samples were measured in a continuous mode, with 2θ angle ranging from (10-70) °2θ, 0.01° step and a scan rate of 2 °/min, and with an incidence angle of 0.80°.

Structural insights were derived through Raman spectroscopy using a WITec alpha300R spectrometer (WITec GmbH, Germany) using a grating of 1800 gr/mm and a 100x EC Epiplan-Neofluar DIC objective (Zeiss, Germany), with a 532 nm wavelength solid-state laser and 10 mW applied power. For the in-situ measurements, a temperature stage from Linkam (model TS1500, Linkam Scientific Instruments Ltd., United Kingdom) was used; the measurement spanned from room temperature (25°C) to 1000°C. Temperature steps of 50°C were employed from 300°C to 650°C and from 800°C to 1000°C. Within the range of 650°C to 800°C, 25°C steps were chosen. Each temperature step had a holding time of 2 min to ensure reaching a steady state.

For a comprehensive examination of thin film morphology and assessment of cleaved cross-section thickness, scanning electron microscopy (SEM) was employed. The imaging was conducted using a Zeiss AURIGA®-CrossBeam® dual-beam SEM (Zeiss, Germany), delivering high-resolution micrographs and critical insights into the surface characteristics and structural attributes. Cross-section images were captured using a 30 µm aperture and a 2 kV excitation. The InLens-Secondary Electron (SE) detector was employed for image acquisition. Surface micrographs, on the other hand, were captured with a 3 kV excitation and a 60 µm aperture. The SE, Back Scattered Electron (BSE), and InLens detectors were employed for surface imaging. Elemental analysis of the thin films was performed by measuring with an energy-dispersive X-ray spectrometer (EDX) at the SEM equipped with an X-Act detector (Oxford Instruments, UK). For point and area measurements, a measuring time of 10 s and an acceleration voltage of 5 kV were selected. In contrast, for element distribution images, a measuring time of 786 s and also an acceleration voltage of 5 kV were employed.

Polarization versus electric field hysteresis loops (P-E loops), temperature dependent dynamic hysteresis loops, leakage and cyclic fatigue measurements were conducted using an aixACCT TF3000 analyzer (aixACCT, Germany). For these analyses, tungsten needles with a tip radius of 20 µm were employed. All polarization measurements were executed at a frequency of 1 kHz and 10 kHz. The leakage current density versus electric field, and also the fatigue measurements were carried out at room temperature. For the temperature-dependent dynamic hysteresis measurements, the range covered was from 20°C to 140°C, with increments of 20°C.

4 Results and Discussion

In the next section, the research results are studied and interpreted, with a detailed analysis of the data obtained. By critically examining these results, meaningful insights are gained, links to the existing literature are established and the implications for a wider field of research are highlighted.

4.1 Raman spectroscopy of thin films

The precursor chemistry was recognized as a crucial factor influencing both the crystallization process and the level of crystallographic texture in thin films based on $BiMgNbO_3$ (BMN). An important role in thin film processing is played by the crystallization temperature, which has to be chosen carefully in order to optimize the crystalline quality (i.e., high density and absence of defects) and texture. In the absence of established literature on BMN thin films, the selected temperature steps for the further processing of the BMN-based thin films were determined through in situ Raman spectroscopy experiments. Raman spectroscopy was used also to confirm the stoichiometry of the thin films as a result of the precursor solutions chemistry. First measurements have been done on the single material system BMN. The measurements were conducted as an in-situ crystallization study, wherein the substrate was coated with the prepared BMN precursor solution using a spin coater. Subsequently, after an additional drying step at 200°C on a hot plate, the coated, not yet crystalline, thin film was introduced into the heating chamber of the Linkam stage in the Raman setup.

This was primarily undertaken to gain insight into the range of crystallization temperatures to be employed within the frame of this study. In addition, it was employed to observe and track the occurrence of potential phase transitions.

The whole in situ measurement was executed from room temperature up to 1000°C. From 25°C on, two further measurements at 100°C, as well as 200°C, have been performed. Starting from 300°C up to 650°C and from 800°C up to 1000°C, temperature steps of 50°C have been used. In the range from 650°C to 800°C, a step size of 25°C was selected to have a better temperature resolution in the expected crystallization temperature window.

From room temperature up to 600°C the Raman spectra of BMN appear consistent with an amorphous thin film. Around 675°C the first changes in the peaks can be recognized by the appearance of broad modes at ~300 cm^{-1} and 550 cm^{-1}, which are

associated with a disordered perovskite structure. [44] 675°C thus marks the start of the thin film crystallization process.

In the scope of this thesis, a rapid thermal annealer (RTA) was employed to facilitate the crystallization of the applied thin films and produce the high-temperature perovskite phase with as little secondary phases as possible. The lowest possible crystallization temperature was chosen to have the least severe impact on the substrates. The heating chamber of the Raman, however, was configured with a heating rate of 2 °C/min. Given the intention to vary the heating rates in the RTA much faster than that from 1 °C/s up to 30 °C/s, it was deemed necessary to select a lower crystallization temperature accordingly. Therefore, a lower boundary of 650°C was established for the annealing of the films in the RTA.
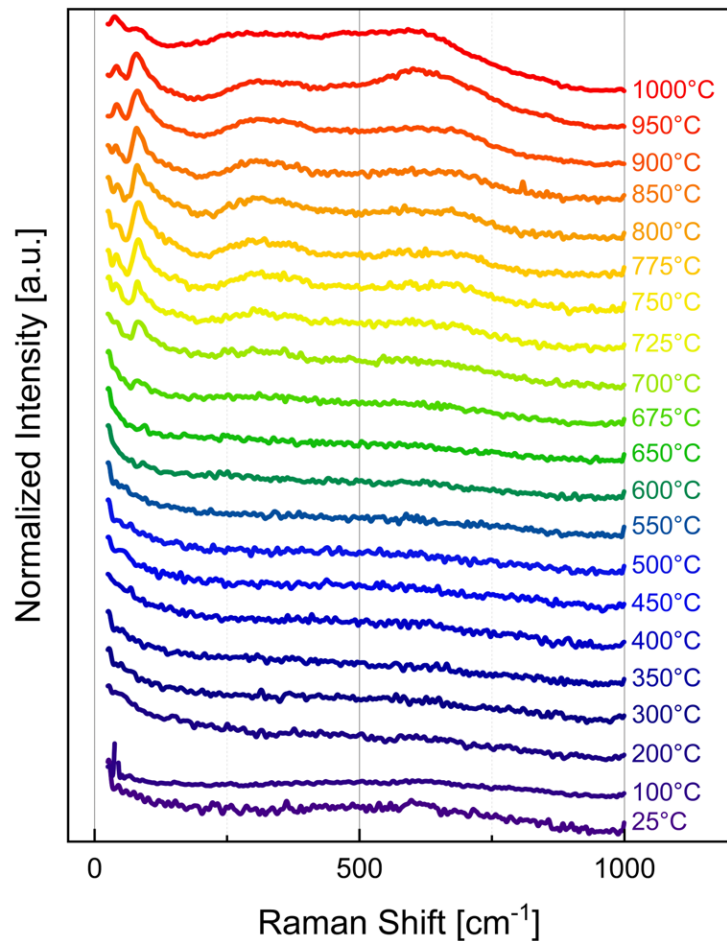

Figure 16: Raman spectra of BMN in-situ temperature-dependent measurement.

As depicted in Figure 16, variations in the Raman spectra are evident up to 1000°C. However, this was not considered as the upper boundary, given that the substrates used for the thin films are incapable of withstanding such high temperatures, which could lead to delamination and diffusion. [22, 23]
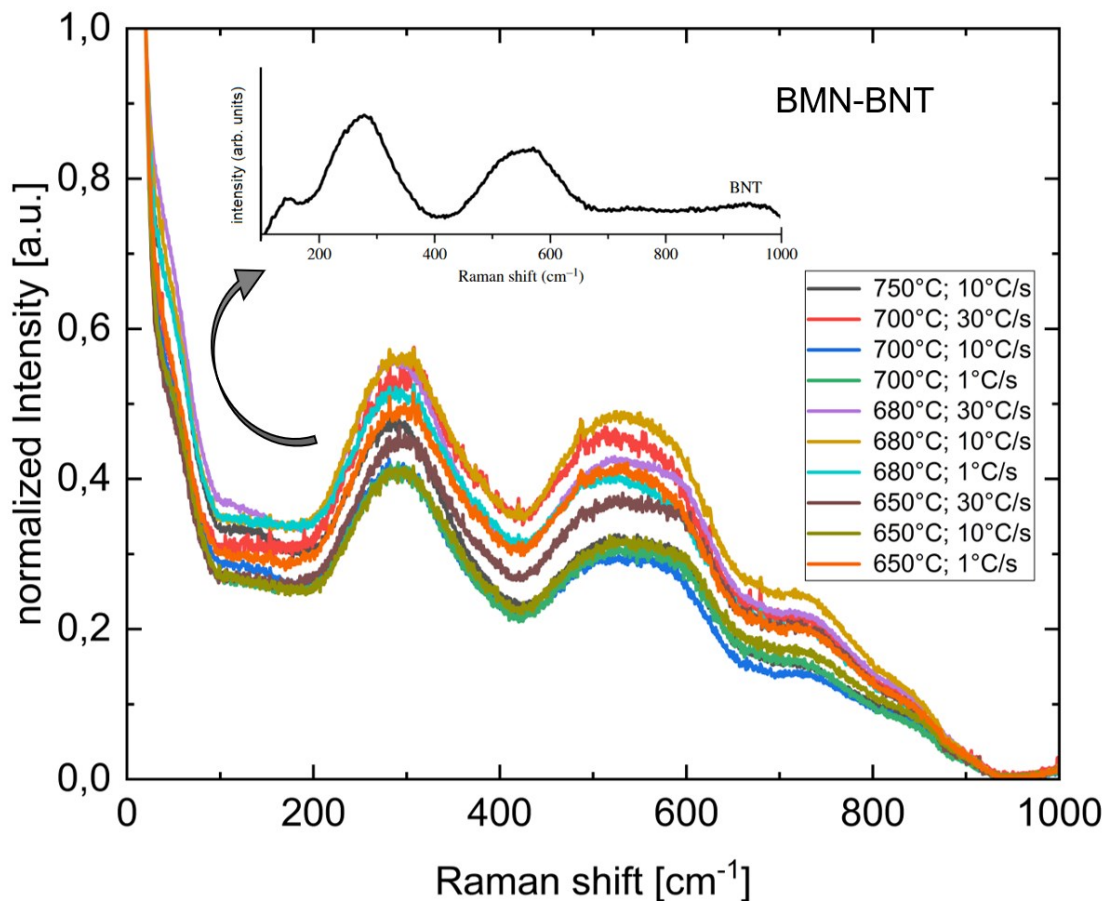
Figure 17: Raman spectra of BMN-BNT thin films at room temperature. [45]

Due to this consideration and the incorporation of Bismuth in the precursor solution, a maximum variation of the crystallization temperature was set at 750°C for the subsequent experiments carried out in the RTA. For the variously prepared thin films of the BMN-BNT material system, Raman measurements were conducted at room temperature (RT) displayed in Figure 17. In Figure 17 above, it is evident that all spectra display similar and more or less broad peaks. No secondary phases were identified that could be attributed to the changed parameters of the process. When the measured spectra are compared with the Raman spectrum of a BNT ceramic [45], similar modes are observed for both materials at 290 cm^{-1} and 540 cm^{-1}. Additionally, less intense modes can be identified around 120 cm^{-1} and 740 cm^{-1}. The modes at around 290 cm^{-1}, 540 cm^{-1} and 740cm^{-1} are an indication for the ferroelectric nature of the produced films, in general it can be said that the appearance of the broad peaks can be explained by a convolution of several peaks. [46] The broad band observed near 290 cm^{-1} (E(TO$_2$)) is indicative of the stretching of short-range TiO$_6$ octahedra, while the band at around 540 cm^{-1} (LO$_2$) is attributed to the symmetric vibration of O-Ti-O stretching within the TiO$_6$ cluster. [47]

Figure 18 presents the Raman spectra of the BMN-NN material system. In comparison with a Raman spectrum of a pure NN thin film [4], it can be observed that the peaks

are all slightly shifted for the measured BMN-NN thin films. This could be ascribed to the combined A- and B-site substitution through Bi^{3+} and Mg^{2+}, respectively. Overall, there were no secondary phases identified that could be linked to the altered parameters of the process. A difference among the prepared BMN-NN films becomes noticeable at low wavenumbers. A distinct and well-defined peak at low wavenumbers is evident in the films prepared with a crystallization temperature of 680°C. This peak cannot come from the antiferroelectric $NaNbO_3$-peaks, located at 60 cm^{-1} and 72 cm^{-1}. [48] In literature no spectral information below 100 cm^{-1} for this structure is reported, contrasting for $Pb(Zr,Ti)O_3$ where this mode, essential for permittivity, is highlighted due to its association with anharmonic Pb vibrations. [49]
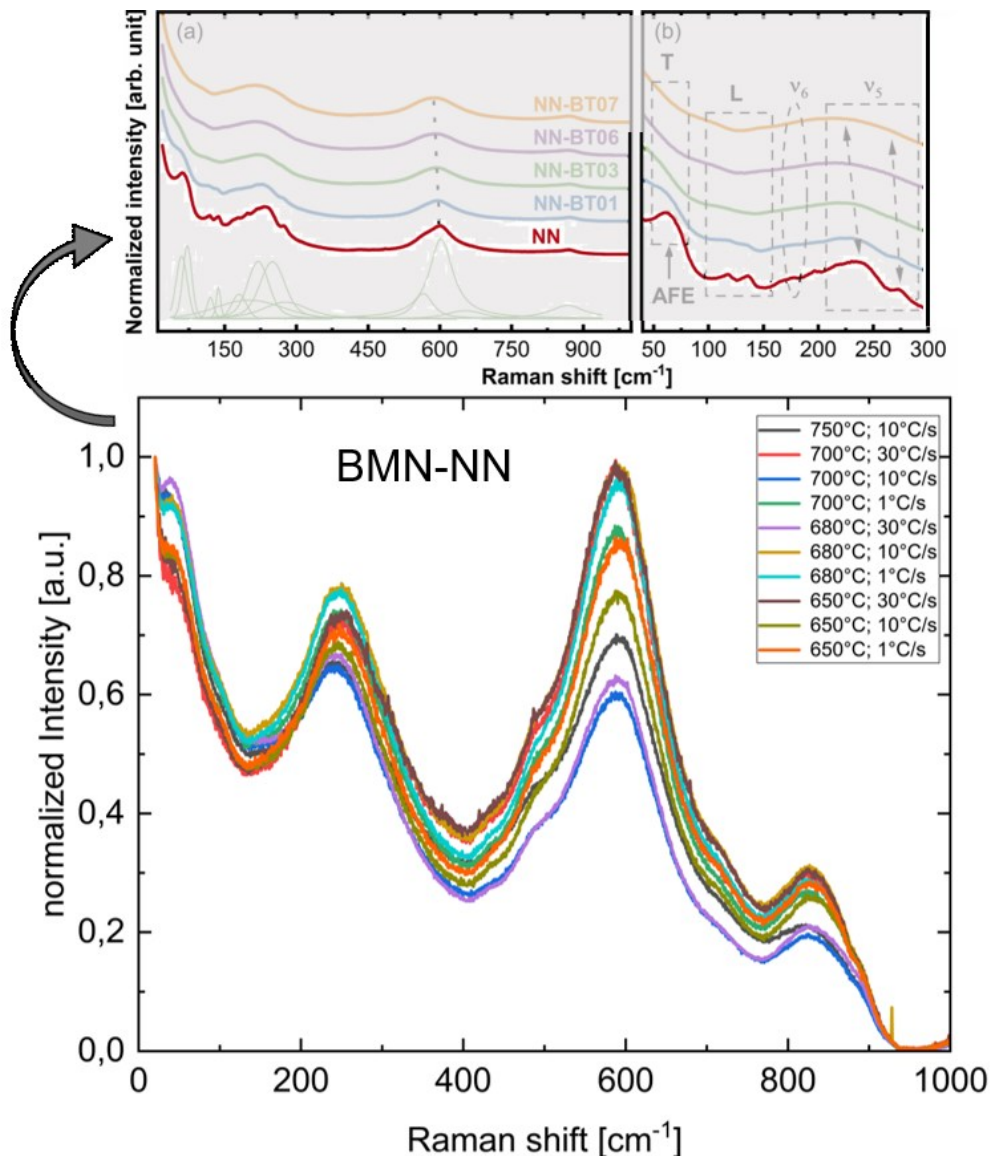

Figure 18: Raman spectra of BMN-NN thin films at room temperature. [4]

4.2 X-ray diffractometry characterization

X-ray diffraction (XRD) is an excellent method for analyzing the structure of materials. Modern diffraction techniques enable us to carry out measurements on thin and ultra-thin films using customized equipment. In the case of this work, the phase of the films is crucial in order to obtain ferroelectric properties. The interest in using this technique was to identify the phases present in the thin films. To achieve this, 2θ scans were performed.

The XRD patterns of the BMN-BNT thin films are presented in Figure 19. The red lines at the bottom of the figure indicate the typical 2θ-values for $Bi_{0.5}Na_{0.5}TiO_3$ (ICDD-number: 036-0340), representing a rhombohedral crystal structure, while the blue lines correspond to $NaNbO_3$ (ICDD-number: 01-074-2456), representing a tetragonal crystal structure. There were peaks observed in some samples, which have been produced at a crystallization temperature of 680 °C, occurring around ~38°, ~45°, and ~65°. These peak positions align remarkably well with the ICDD-code 01-074-2352 of Bi_4O_7. This secondary phase (marked with (*) in Figure 19) due to Bi excess could arise due to variations in the precursor ratios or other processing conditions, leading to an incomplete reaction or incomplete incorporation of $Bi_{0.5}Na_{0.5}TiO_3$ and the formation of the Bi_4O_7. It would be valuable to investigate and optimize the stoichiometric ratios to minimize the presence of unreacted Bi_4O_7 in the final material.
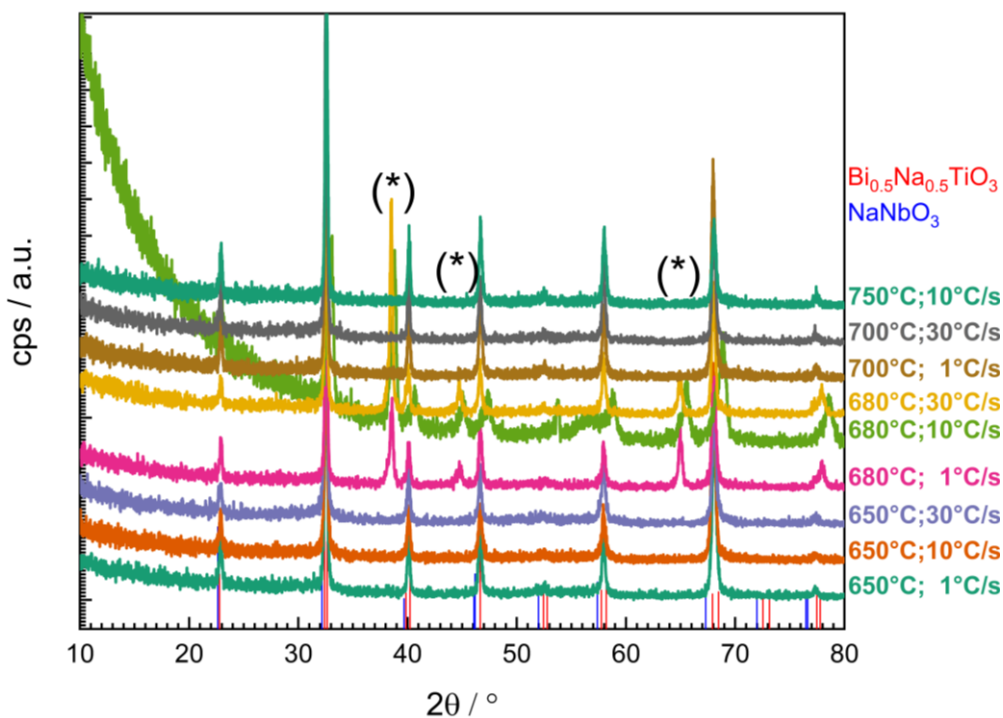

Figure 19: XRD pattern of BMN-BNT thin films at room temperature, secondary phases (*).

The deviation of the curve's behavior from the norm, observed in the sample produced with a heating rate of 10 °C/s and a crystallization temperature of 680 °C (light green line), can be attributed to sample alignment. Despite the appearance of a larger baseline, the positions of the peaks remain unchanged and unshifted, so baseline subtraction was not performed.

In Figure 20, the XRD patterns of the material system BMN-NN at room temperature are shown. The blue lines in Figure 20 denote $NaNbO_3$ (ICDD-number: 01-074-2456), indicating its tetragonal crystal structure, while the red lines represent the typical 2θ-values for $Bi_{0.5}Na_{0.5}TiO_3$ (ICDD-number: 036-0340), indicating its rhombohedral crystal structure. Again, additional peaks can be found for the samples with a crystallization temperature of 680 °C at ~38°, ~45°, ~65° and ~78°, which are most likely from Bi_4O_7 or $NaBiO_3$ (ICDD: 00-050-0085), marked with (*) in Figure 20.
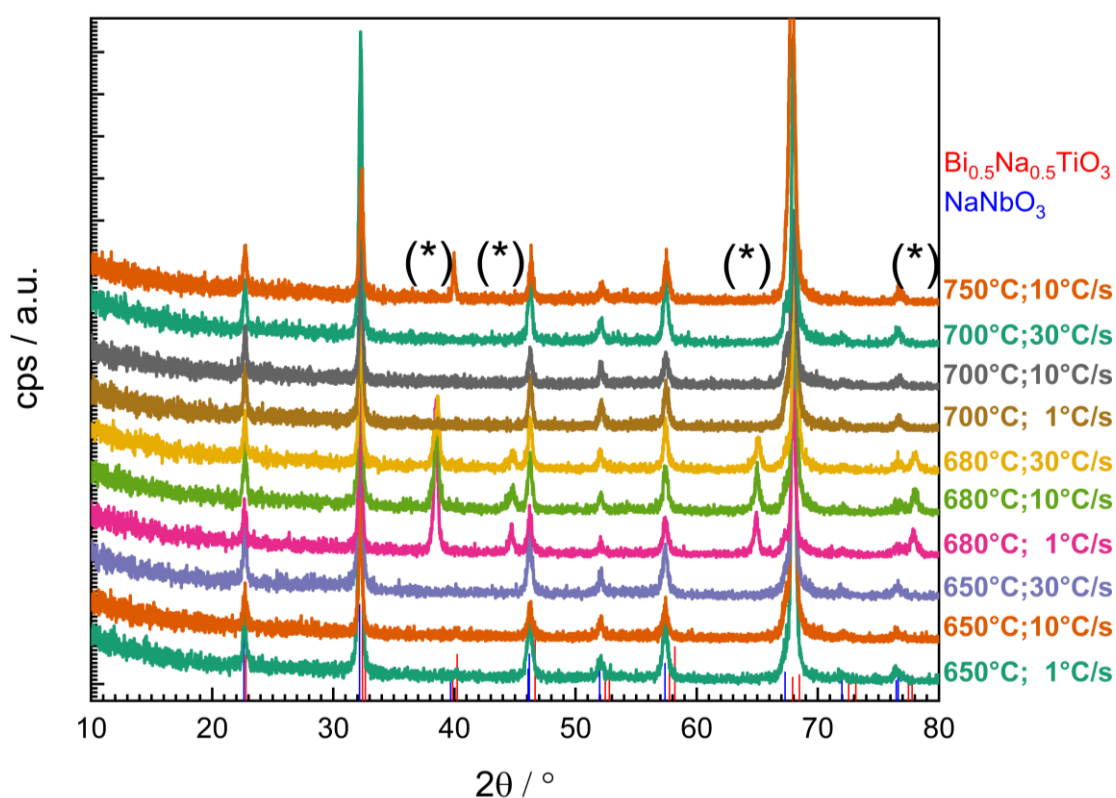

Figure 20: XRD pattern of BMN-NN thin films at room temperature secondary phases (*).

For a more comprehensive interpretation of the XRD data, the peak around 32° (the most intensive peak) was selected and analyzed in detail. (Figure 21) It is apparent that in both XRD patterns (Figure 19 and Figure 20), the peak seems to be a combination peak of the $Bi_{0.5}Na_{0.5}TiO_3$ as well as the $NaNbO_3$. Subsequently, as it can be seen in Figure 21, a discernible shift towards higher 2θ-values becomes evident for both BMN-based systems, as soon as the crystallization temperature increases. This

observed shift could be interpreted as a contraction or reduction in the lattice parameter.

Observing the red dots in Figure 21 for the BMN-BNT system, it can be noted that at 650°C, the peak remains stationary, regardless of the heating rate. Similarly, for the thin films produced with a crystallization temperature of 680°C and subjected to both low and high heating rates (1 °C/s and 30 °C/s), a consistent behavior is observed. The 680/10 exhibits a distinctly different behavior, as evident and explained in Figure 19 as well.
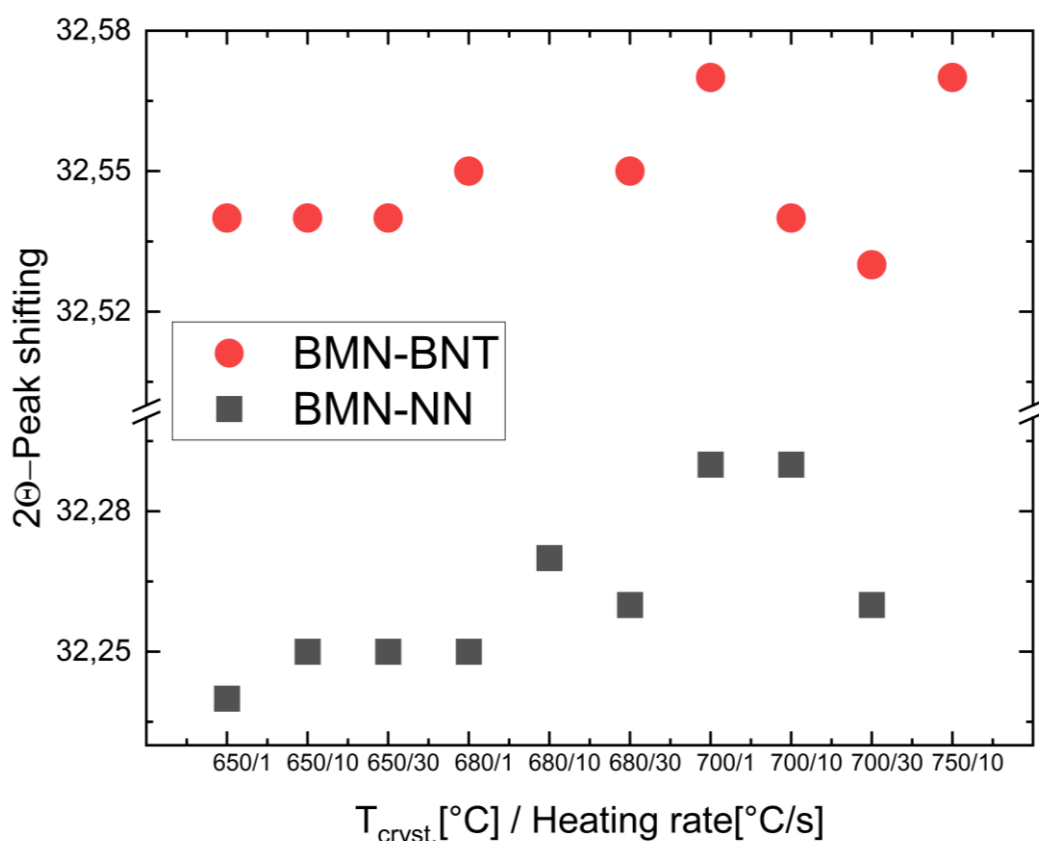

Figure 21: Peak shifting, depending on different $T_{cryst.}$ and heating rates, at a 2Θ value of 32°, outlier observed at 680/10 out of range.

Generally, XRD measurements provide insights into the average lattice constants over a significant volume. An outlier observed at 680°C indicates the presence of a secondary phase, resulting in a notably different overall average lattice constant, as the lattice constant of the secondary phase must be smaller than that of BMN. The A-site substitution in BMN-NN, which increases the ionic radii, leads to a decrease in the 2θ values. Conversely, BMN-BNT exhibits a much lower increase in A-site substitution due to the 50:50 ratio Bi by Na substitution, resulting in BMN-NN having a much lower 2θ value than pure BMN, while BMN-BNT shows a smaller decrease compared to BMN. At 650 °C, the 2θ values are constant over all used heating rates and relatively lower than at the other temperatures, possibly associated with an enlarged lattice

parameter. This indicates of an effective incorporation of $Bi_{0.5}Na_{0.5}TiO_3$ (BNT) into the BMN system at this temperature, correlating with observed optimal leakage behavior and the highest W_{rec} values at this temperature for the highest attainable electric field strength. Additionally, films synthesized at a $T_{cryst.}$ of 700°C with heating rates of 10 °C/s and 30 °C/s exhibit comparable peak positions and demonstrate the best temperature stability. Thus, variations in peak position among other values may be attributed to different lattice constants, possibly coming from secondary phases.

In case of the BMN-NN system, represented by the gray squares in Figure 21, a similar trend is observed. Minimal or negligible shifts are observed at lower crystallization temperatures, while a more pronounced shift towards higher angles, and consequently higher 2θ-values, becomes evident with increasing temperature.

For BMN-NN, the peak positions observed at higher values for a $T_{cryst.}$=700°C and heating rates of 1 °C/s and 10 °C/s represent the best properties, suggesting an optimal lattice parameter in that range. It appears that NN is more sensitive to process parameters overall, exhibiting a wider deviation range compared to BNT, with maximum variation values of 6% for NN and 4% for BNT, respectively. This variability highlights the need for precise control and optimization of processing parameters to achieve consistent and desired material properties, especially when working with BMN-NN thin films.

In general, it is common to observe slight shifts in the peak positions in the 2theta scan, which can be attributed to factors such as residual stresses, substrate-induced strain, or compositional changes in the film. The shape of the peaks is influenced by the size of the grains, as well as compositional gradients and strain distributions. It is also essential to check the substrate peak positions, so that a reference sample is used to verify the proper alignment of the diffractometer. In addition, the lattice parameters of the film can change due to factors such as compositional strain, epitaxial strain, thermal strain or intrinsic residual strain. Oxide layers are usually reduced during deposition, which leads to chemical expansion. To maintain oxygen stoichiometry, annealing in an oxidizing atmosphere is often required. Further XRD experiments, including reciprocal space mapping (RSM), residual stress analysis and in-plane diffraction, may be required to fully understand the nature of strain in a particular layer. [38]

For thin films, however, it is critical to consider other sources of peak broadening that may exceed the contribution of crystal domain size. As mentioned earlier, thin film materials are susceptible to retaining lattice strains that affect their average structure and cause shifts in peak positions, often referred to as macrostrain. [38]

4.3 Scanning electron microscopy characterization

Scanning electron microscopy is a very well-known and practical method to explore the morphological aspects of materials at the nanoscale, in particular to probe the surface morphology and cross section of thin films. Zhou et al. described in detail the fundamentals of SEM. [32]

As already noted in Figure 7 in chapter 0, the impact of the heating rate on the microstructure is relatively minor compared to the temperature, since the heating rate is only varied in the °C/s range and not to °C/min. In this section, the characterization and the influence of different heating rates and crystallization temperatures on the deposited thin films are investigated.

In consideration of electrical properties, which will be further discussed and explained in the next section, a comparison was made between on the one hand thin films produced at the same temperature and on the other hand those produced with the same heating rate. These selected films were then subjected to characterization using SEM. The discussion includes cross-section as well as top-view SEM images. All the cross-section images reveal distinct layers, beginning from the bottom with Si, SiO_2, TiO_2, Pt, and culminating with the deposited functional dielectric on top. This is shown in Figure 22, serving as an example for all the conducted cross-section images. All the films have been measured on a spot without the sputtered gold electrode on top, in the picture the position of the Au/Cr layer is exemplified by a drawn model for visualization.
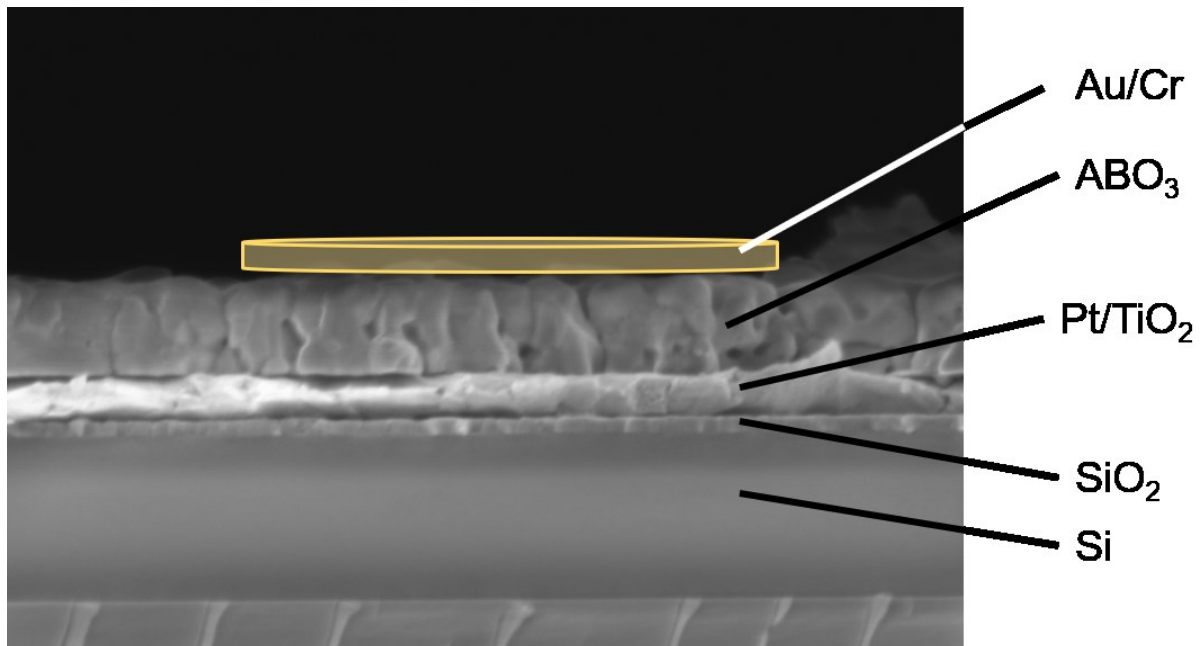

Figure 22: Cross-section of a BMN-based thin film.

In Figure 23 a), cross-sectional SEM micrographs of BMN-BNT samples are presented, all obtained under a consistent crystallization temperature of 700°C. Nevertheless, a distinction is evident; films prepared with a low heating rate (1 °C/s) and those with a high heating rate (30 °C/s) appear less dense, exhibiting some noticeable intergranular porosity, but in general, these two rates show a columnar growth of the grains. In contrast, thin films prepared with a heating rate of 10 °C/s show a denser but more granular microstructure. Even in the cross-section, a variation in grain size is apparent. A more detailed discussion on this aspect will be presented through the top-view images showcased in Figure 23 b) and Figure 23 c).
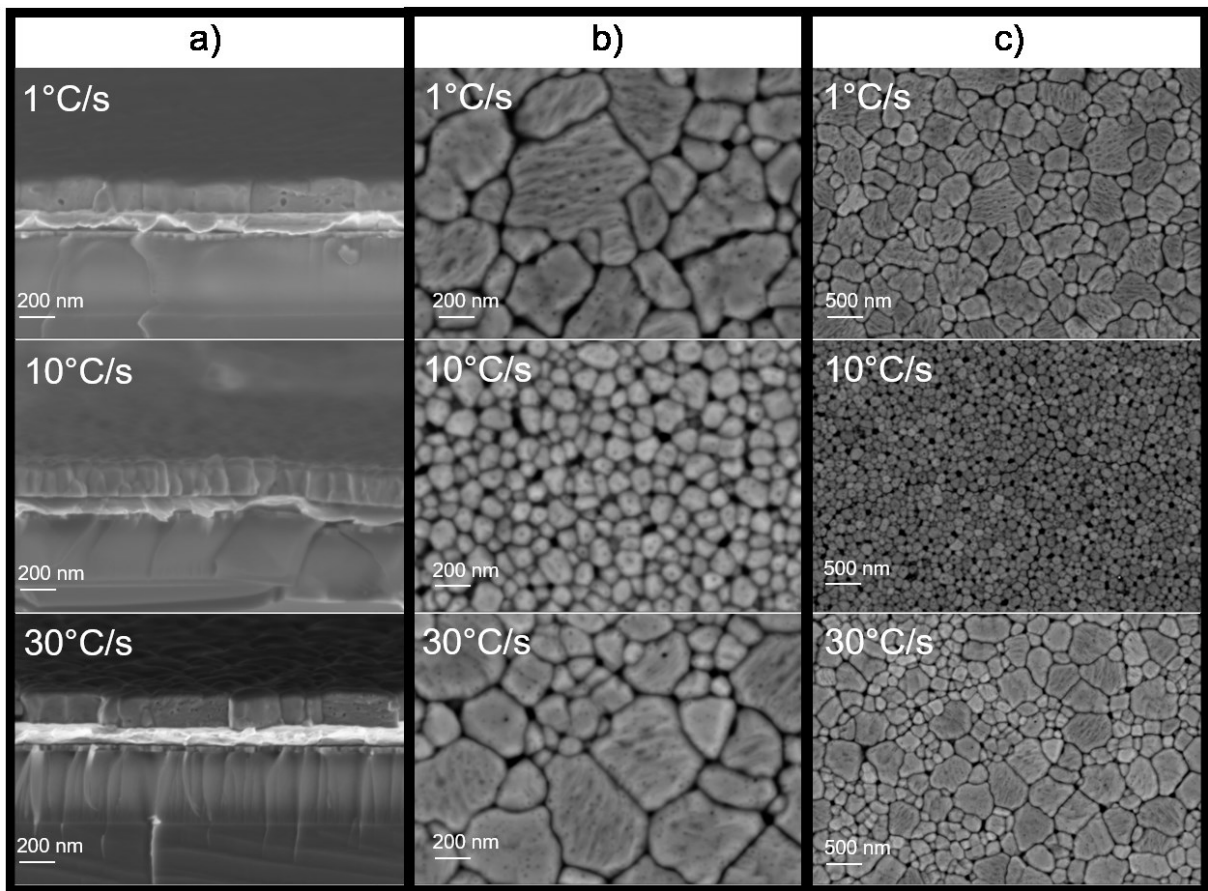

Figure 23: SEM BMN-BNT thin films micrographs a) cross-section b) surface with 50K magnification and c) surface with 20K magnification: a comparison of the different heating rates at a const. crystallization temperature of 700°C.

Cross-sectional SEM measurements of the BMN-based thin films were also performed to measure the thickness of the thin films. The thickness was determined using ImageJ by calculating the average of ten measurements of the functional dielectric lengths in the cross-section. The mean film thicknesses of all BMN-BNT thin films, which have been characterized with SEM, are presented in Table 3.

Table 3: Overview of the mean thicknesses of BMN-BNT thin films.

Material system	Crystal. Temperature [°C]	Heating rate [°C/s]	Mean Thickness [nm]
BMN-BNT	650	10	189.705 ± 8.135
	680	10	170.568 ± 9.679
	700	1	188.236 ± 9.952
	700	10	182.128 ± 8.832
	700	30	181.479 ± 9.964
	750	10	205.035 ± 15.659

Table 3 reveals that the film thicknesses are generally comparable and within a similar range. Therefore, the thickness for calculating the electric field is assumed to be 200 nm for all measured thin films.

As mentioned before, the top-view micrographs can be seen in Figure 23 b) and Figure 23 c). In column b), a magnification of 50K is presented, whereas column c) is captured at the same location but slightly further away, featuring a magnification of 20K. This provides a broader view of the deposited dielectric layer. For the films produced with both low and high heating rates (1 °C/s and 30 °C/s), a well-blended combination of large and small grains is evident. The films produced with a heating rate of 10 °C/s exhibit the highest level of homogeneity, marked by the presence of both, small grains and a consistent distribution of grain sizes throughout the structure. This noteworthy combination suggests a well-controlled and uniform crystallization process, contributing to the overall structural integrity and quality of the thin films. The careful balance of grain sizes at this heating rate underscores the effectiveness of the crystallization conditions, highlighting its significance in achieving optimal film properties.

Figure 24 now highlights chosen BMN-BNT thin films with a consistent heating rate of 10 °C/s, showcasing variations in crystallization temperature at 650°C, 680°C, 700°C, and 750°C. In column a) of Figure 24, cross-section images are presented. In this instance, a notably intergranular porous microstructure is evident at 650°C, gradually becoming more homogeneous as the temperature increases.
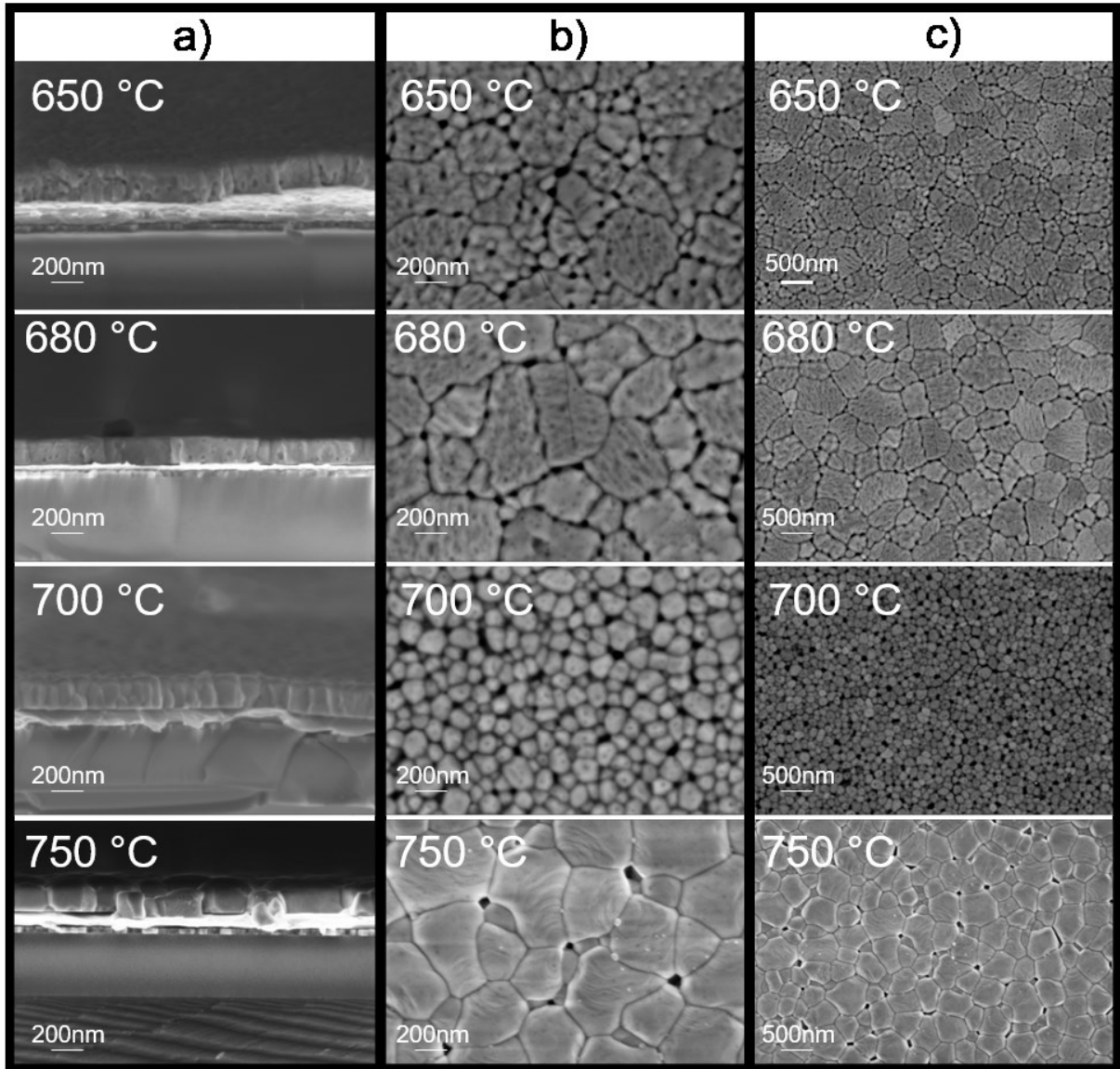
Figure 24: SEM BMN-BNT thin films micrographs a) cross-section b) surface with 50K magnification and c) surface with 20K magnification: a comparison of the different T$_{cryst.}$ at a const. heating rate of 10 °C/s.

Upon analyzing the top view (Figure 24 b) and Figure 24 c)), it becomes apparent that the grain sizes and distribution vary significantly depending on the different temperatures. At 650°C and 680°C, the grains appear with intergranular porosity, and there is an observable increase in grain sizes. At 700°C, a distinct image emerges, with the grains appearing more granular and exhibiting no further intergranular porosity. A homogeneous distribution of grain sizes is noticeable. At 750°C, the grains become significantly larger, accompanied by the emergence of voids or holes between the grain boundaries. A form of layer growth away from the grain boundaries becomes apparent. This can be explained by the interaction between the underlying layer and the added layer, which determines the growth mode to a large extent. Unfortunately, electrical measurements could not be conducted at this particular temperature. The

unavailability of such data limits the insights into the electrical characteristics of the BMN-BNT thin films specifically above 700°C. This gap underlines the need for further investigations and measurements to gain a comprehensive understanding of the electrical behavior of thin films at different crystallization temperatures.

Figure 25 a) shows a detailed view of SEM micrographs representing BMN-NN thin films. These films share a uniform crystallization temperature set at 700°C. This controlled parameter allows a focused examination of the microstructural characteristics across various regions of the thin films.
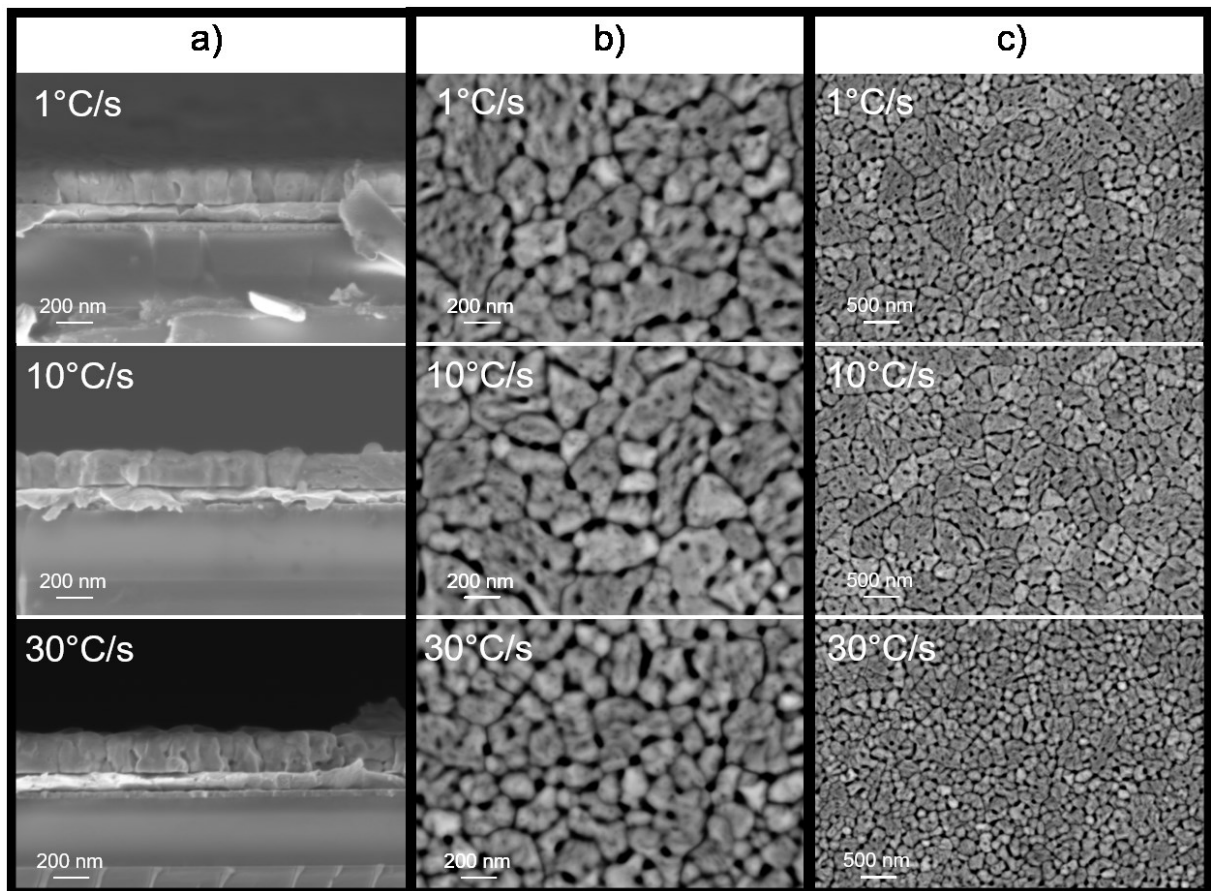

Figure 25: SEM BMN-NN thin films micrographs a) cross-section b) surface with 50K magnification and c) surface with 20K magnification: a comparison of the different heating rates at a const. crystallization temperature of 700°C.

No significant difference can be seen when comparing the different heating rates in the cross-section images of Figure 25 a); however, the films produced at a rate of 10 °C/s have a slightly denser appearance compared to the others.

Examining the top view of Figure 25 b) and c) reveals a significant similarity among the films, with the smallest grains apparent at the highest heating rate (30 °C/s). In a broader context, the films show some grains with a presence of intergranular porosity, but the grains showcase a distinctive columnar growth pattern throughout the material structure. This observation implies a nuanced relationship between the material's

microstructure and the prevalent heating conditions. Also, the grains in the thin film subjected to the highest heating rate (30 °C/s) appear more granular compared to those with lower heating rates.

As previously mentioned, cross-sectional SEM measurements were performed also on the BMN-based thin films, to assess their thickness. Utilizing ImageJ, the thickness was determined by averaging ten measurements of cross-section functional dielectric lengths. Table 4 provides now the mean film thicknesses for all BMN-NN thin films that underwent SEM characterization.

Table 4: Overview of the mean thicknesses of BMN-NN thin films.

Material system	Crystal. Temperature [°C]	Heating rate [°C/s]	Mean Thickness [nm]
BMN-NN	650	10	224.091 ± 15.862
	680	10	216.417 ± 9.542
	700	1	205.714 ± 7.172
	700	10	213.220 ± 6.037
	700	30	224.227 ± 6.664
	750	10	181.241 ± 7.520

When comparing the thicknesses of the films, Table 4 reveals that those of the BMN-NN films are slightly greater than the corresponding values for the BMN-BNT material, as presented in Table 3. The thickness of the thin films is generally very similar. Hence, a uniform thickness of 200 nm is assumed for calculating the electric field across all measured thin films.
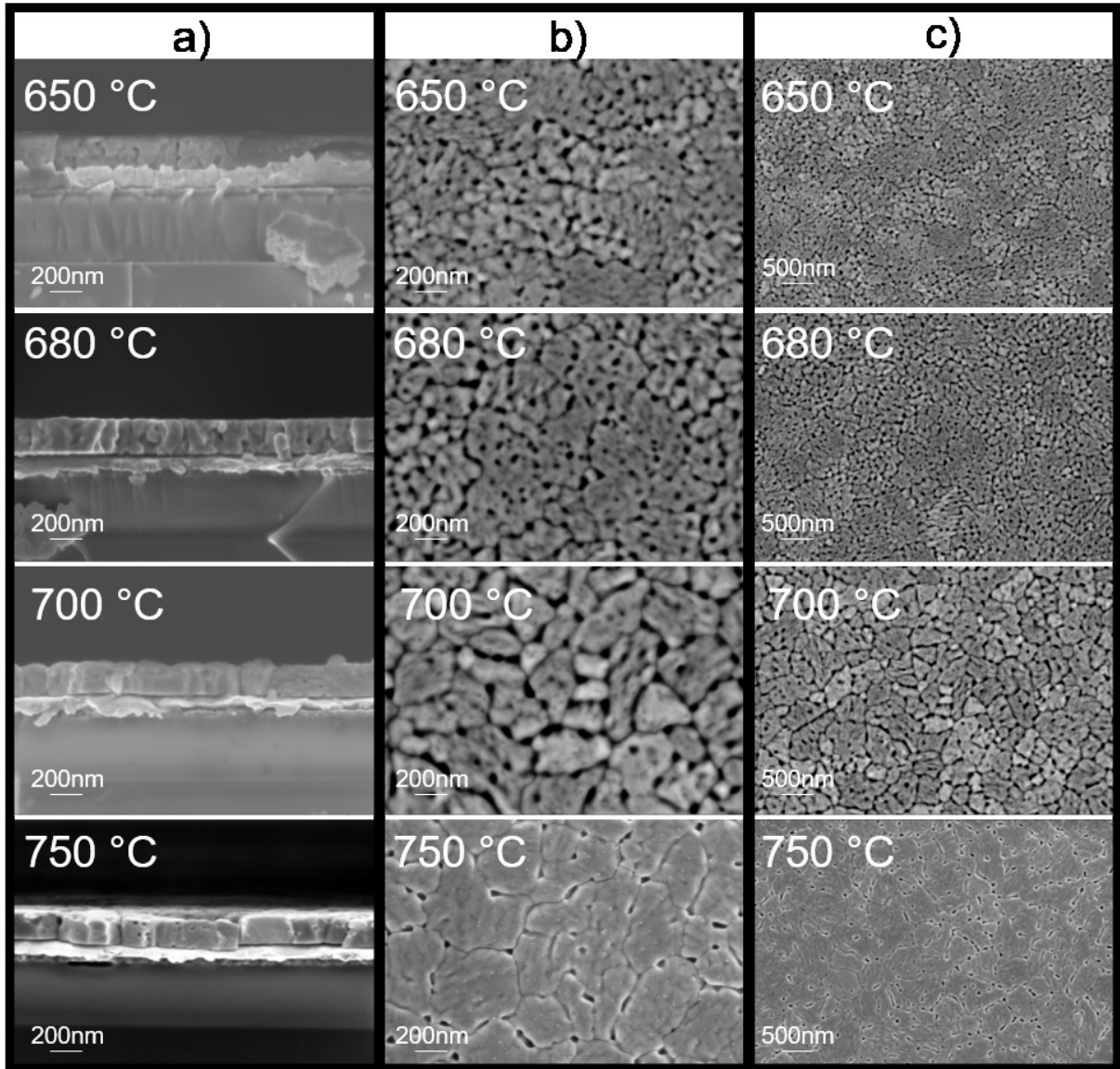
Figure 26: SEM BMN-NN thin films micrographs a) cross-section b) surface with 50K magnification and c) surface with 20K magnification: a comparison of the different $T_{cryst.}$ at a const. heating rate of 10 °C/s.

Figure 26 now features chosen BMN-NN thin films, also specifically selected based on their electrical properties. These films were subjected to a uniform heating rate of 10 °C/s, highlighting variations in crystallization temperature at 650°C, 680°C, 700°C, and 750°C.

The correlation between temperature and grain size is evident: as the temperature increases, the size of the grains also increases. However, it is important to acknowledge the limitations due to interphase problems. With the rise in temperature, there is a noticeable transition in the microstructure to a denser configuration. While grains at 700°C and 750°C exhibit a more separated appearance, the overall microstructure at higher temperatures displays a remarkable reduction in intergranular porosity compared to the films processed at lower temperatures of 650°C and 680°C.

This shift in the structural characteristics underscores the influence of temperature on the density and integrity of the thin films.

Once again, the electrical measurements for the BMN-NN films faced challenges, proving unfeasible at 750°C as the application of an electrical field was not possible. This limitation hinders a comprehensive understanding of the electrical properties of the films at the specific conditions of the elevated high temperature.

In general, for both systems, it can be said that at a temperature around 650°C, interdiffusion takes place between the individual layers. Furthermore, at approximately 750°C, TiO_2 loses its effectiveness as a diffusion barrier completely. [22, 23] The substrates employed in this study are standard substrates commonly used in this field. Alternatively, to address the issue of diffusion barrier loss, substrates like ZnO or others may prove more suitable for applications at high temperatures. [22, 23]

The SEM topography micrograph presented in Figure 27 a) reveals no microstructural inhomogeneities on the nanoscale. A homogeneous microstructure can be confirmed upon comparing the positions of these areas with the respective positions on the EDX elemental mappings, which can be seen in Figure 27 b) to h). The brightness/darkness effect observed in Figure 27 a) can be explained by the topographical variances resulting from distinct crystal orientations within the microstructure. This phenomenon offers insights into the structural complexity of the material, highlighting how various orientations contribute to the overall topographic features observed in the SEM micrograph.
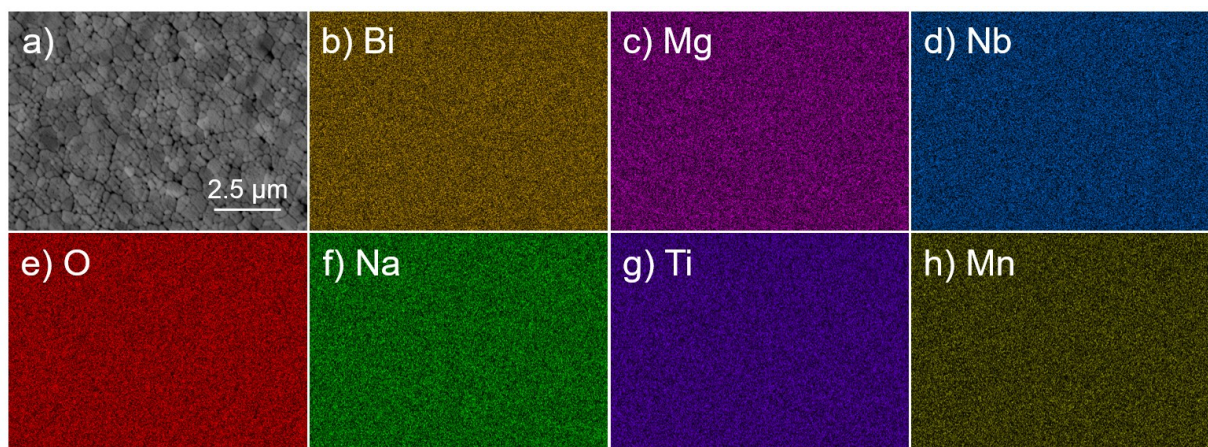

Figure 27: BMN-BNT SEM (secondary electrons) surface image of the film deposited at 700°C crystallization temperature and EDX mapping of the same region of b) Bi, c) Mg, d) Nb, e) O, f) Na, g) Ti and h) Mn.

The same characterization has been conducted for the BMN-NN system. In Figure 28 a) the SEM topography micrograph shows no discernible microstructural inhomogeneities. The uniform and homogenous microstructure also for this material is

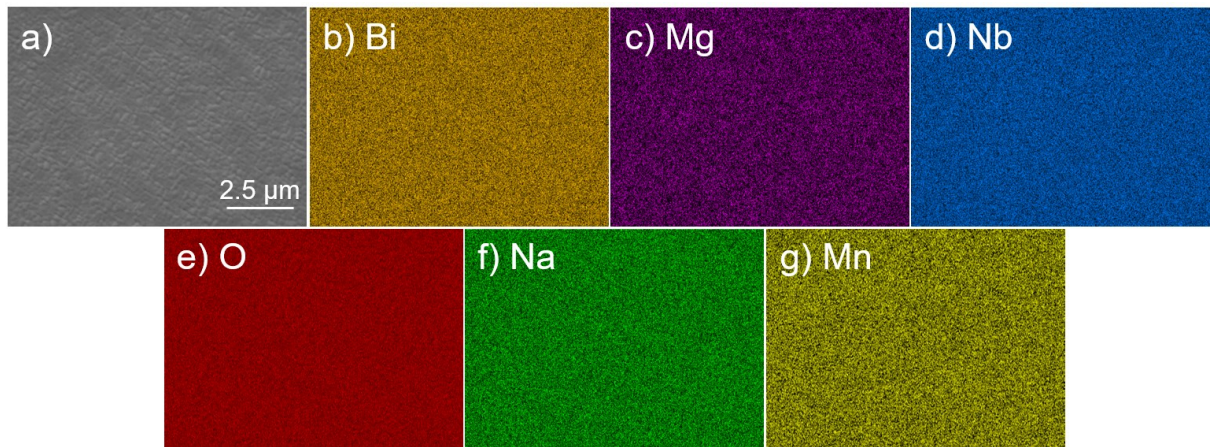affirmed upon comparison with the corresponding positions on the EDX elemental mappings in Figure 28 b) to g).

Figure 28: BMN-NN SEM (secondary electrons) surface image of the film deposited at 700°C crystallization temperature and EDX mapping of the same region of b) Bi, c) Mg, d) Nb, e) O, f) Na and g) Mn.

In Figure 29, the behavior of the atom% in BMN-BNT-based thin films is illustrated, showcasing variations with different heating rates and crystallization temperatures.
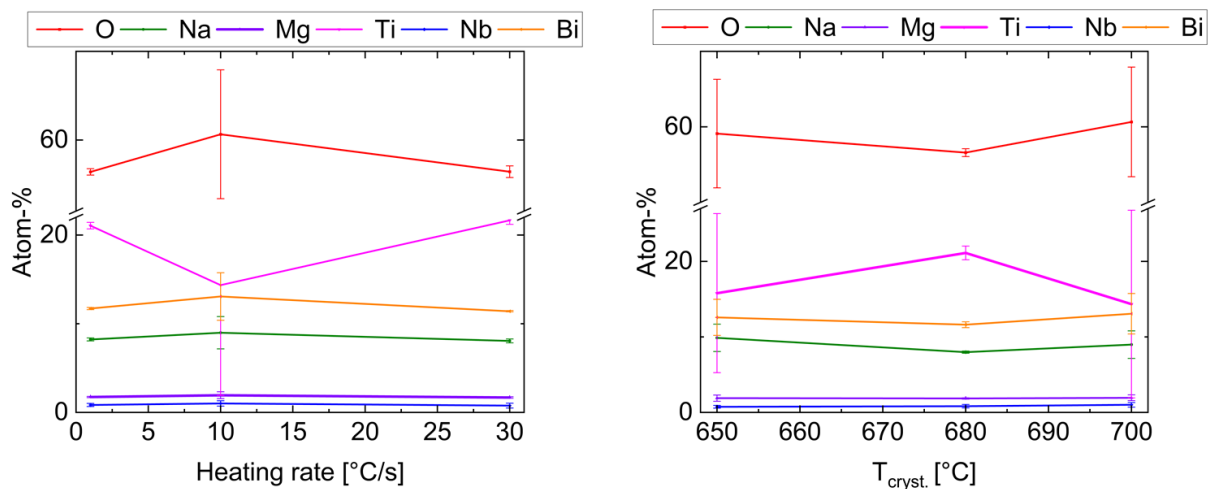

Figure 29: BMN-BNT elemental distribution over Heating rate ($T_{cryst.}$ = const. = 700°C) and $T_{cryst.}$(HR = const. = 10 °C/s).

For each thin film sample of BMN-BNT, elemental distribution measurements were conducted through two single-point measurements and one area scan. To gain a comprehensive understanding of elemental distribution in the films, the results from all measurements were averaged. The analysis revealed a notable high error bar at a heating rate of 10 °C/s, which can be attributed to the single-point measurements. In certain areas, Titanium (Ti) is essentially absent, explaining the observed variations. The atom% for each element generally aligns with expectations and calculations, with

the exception of Titanium, which, although still within the range, exhibits some variation due to the averaged measurements.
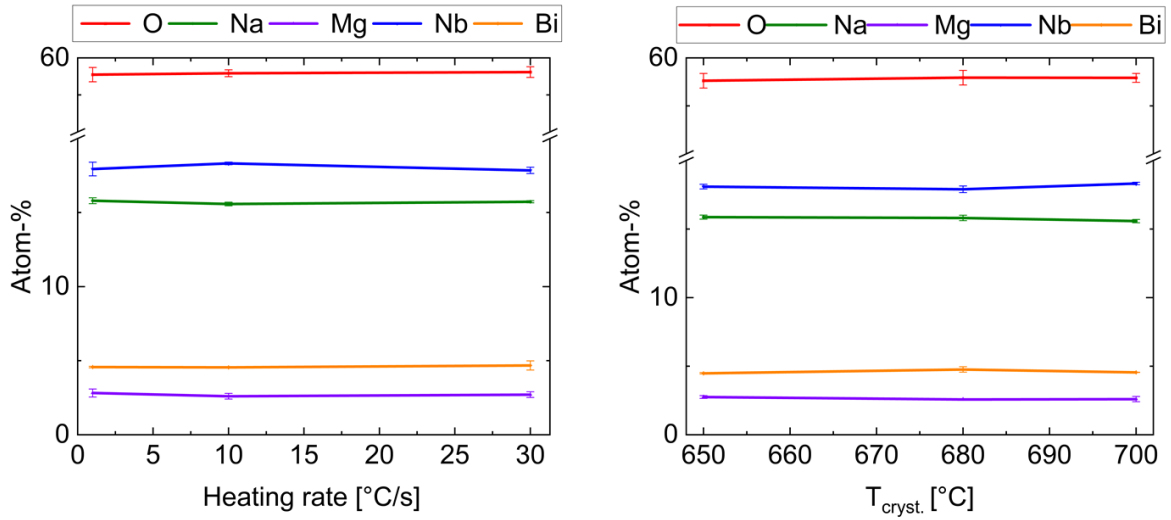

Figure 30: BMN-NN elemental distribution over Heating rate (T_{TZ} = const. = 700°C) and $T_{cryst.}$(HR = const. = 10 °C/s).

Similar to the approach taken for the BMN-BNT material, elemental distribution measurements for BMN-NN thin film samples were carried out using two single-point measurements and one area scan. Figure 30 illustrates that the material displays a remarkably stable elemental distribution behavior, both across different heating rates and varying crystallization temperatures. This stability is also visually evident in SEM images (Figure 25), where minimal changes in density or homogeneity are observed. Furthermore, the elemental composition remains in line with expectations and calculated values, indicating consistent and expected amounts.

4.4 Electric measurements and electric properties

This section deals with systematic research into the electrical behavior and properties of the BMN-based systems. Through precise measurements and in-depth analysis, this section aims to explain the electrical properties and clarify fundamental aspects that improve the overall understanding of the subject, also in view of a potential application of the investigated materials.

4.4.1 Polarization-electric field (PE) hysteresis loops

The section on the PE loops is divided into two subsections to provide a more comprehensive understanding of the area of application.

4.4.1.1 Bipolar dynamic hysteresis measurements

The dynamic hysteresis measurements record the hysteresis loop of a ferroelectric material and help to analyze the influence of the process parameters on the shape of the hysteresis loop. Measurement parameters such as the amplitude or frequency of the excitation signal can be varied. Either bipolar or unipolar loops have been chosen as representative examples due to their ability to achieve the highest electric field, coupled with elevated values of electrical properties such as W_{rec}. Bipolar PE-loops of the BMN-based thin films and are showcased in Figure 31 a) and b) for BMN-BNT and BMN-NN, respectively. For BMN-BNT, an electric field of 1000 kV/cm could be attained at a frequency of 10 kHz, while for BMN-NN, at the same frequency, an electric field of 750 kV/cm was achieved. A detailed discussion of all the characteristics will be provided in the upcoming section.
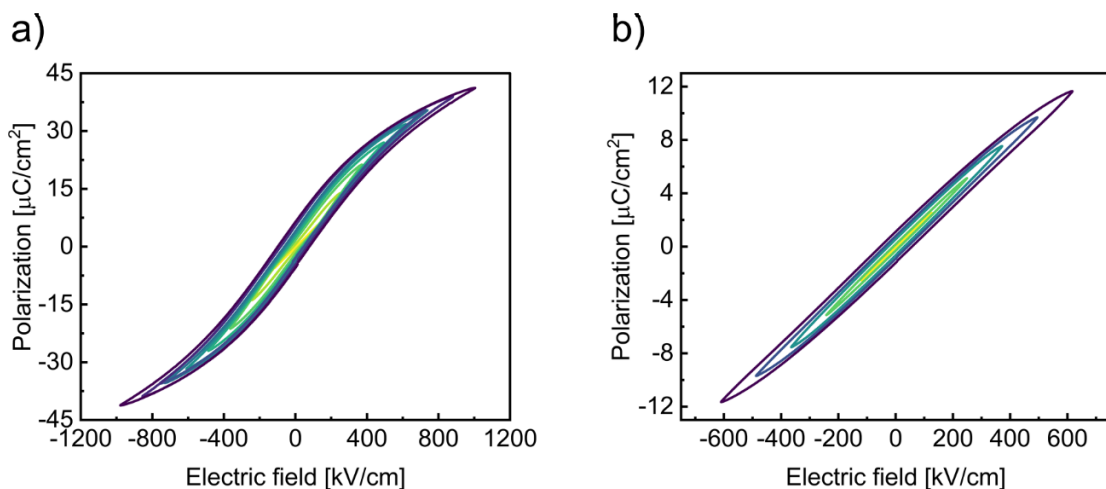

Figure 31: Bipolar PE-loops up to the highest reachable electric field of a) BMN-BNT and b) BMN-NN.

Generally, and as confirmed by the experiments in this study, films tend to exhibit more leakage at lower frequencies (around 1 kHz), leading to lower energy storage efficiency. Increasing the frequency helps suppressing some of the leakage effects, as the dynamics of surface charges and defects are slower than approximately 1 kHz. However, true ferroelectric switching occurs across a wide range of frequencies. To reduce the impact of leakage contributions, all films were measured at 10 kHz to decouple from the leakage and consequently provide a more accurate evaluation of the actual energy storage properties. To gain a better understanding and insight of how the heating rate and temperature influence the electrical properties of the bipolar loops, a comparison of relevant properties over the electric field was conducted. Firstly, it must be acknowledged that electrical measurements could not be conducted on films crystallized at a temperature of 750°C. This could be explained by a damaged microstructure, an interdiffusion with the substrate or a possible damage of the substrate due to elevated temperatures. The high failure rate resulted in a mix of successful and unsuccessful attempts, making it impossible to draw any scientific conclusions. So, for all the electrical measurements, films produced with crystallization temperatures of 650°C, 680°C, and 700°C were selected for a comparison. The W_{rec} over electric field behavior for BMN-BNT thin films can be seen in Figure 32.
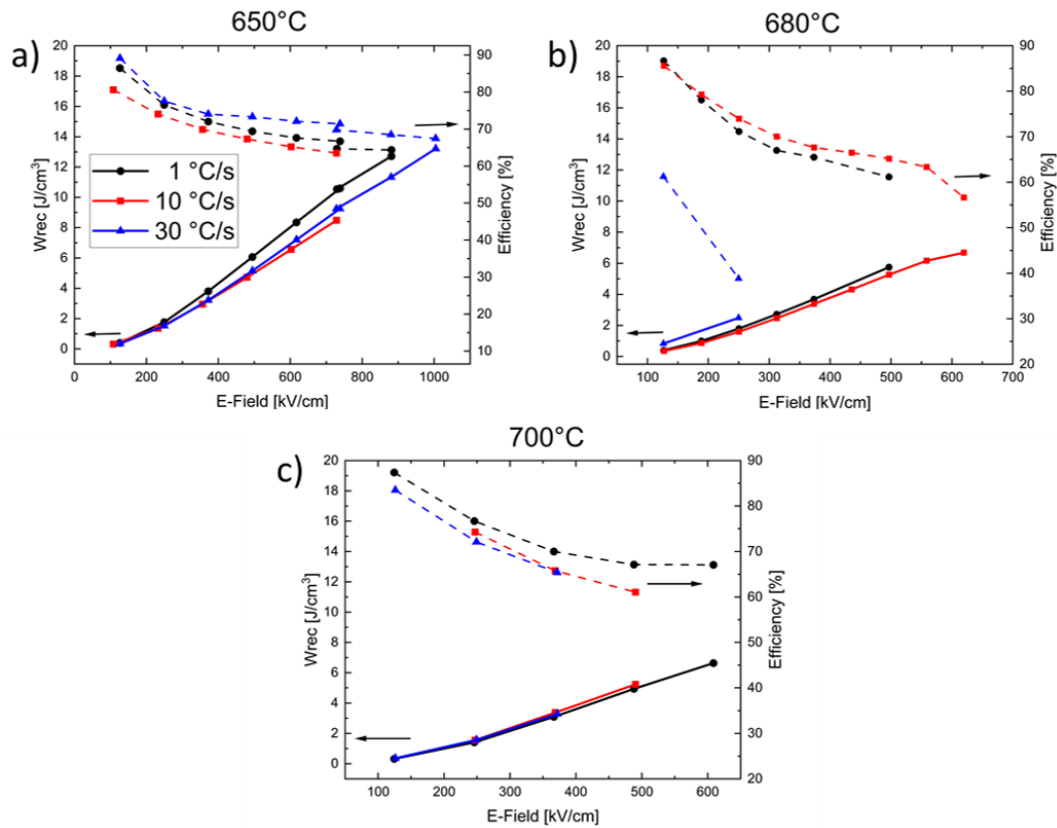

Figure 32: BMN-BNT thin films: Behavior of varying heating rate at a) T_{cryst} = 650°C, b) $T_{cryst.}$ = 680°C and c) $T_{cryst.}$ = 700°C on electric field.

In Figure 32 a), it is evident that for a crystallization temperature of 650°C, the highest electric field as well as the highest value for recoverable energy density (W_{rec}) can be achieved with a heating rate of 30 °C/s. Additionally, the efficiency exhibits the most favorable behavior under these conditions. Likewise, the behavior is relatively consistent across other heating rates, yet a breakdown at lower electric field levels becomes evident. At a crystallization temperature of 680°C, as depicted in Figure 32 b), the lowest (1 °C/s) and the middle (10 °C/s) heating rates demonstrate the highest values for W_{rec} as well as for the efficiency. However, the highest heating rate (30 °C/s) tested over the electric field did not surpass values higher than 250 kV/cm, indicating a notably low best-case breakdown strength under these conditions. As evident in Figure 32 c), at 700°C, all three heating rates exhibit nearly identical behavior, characterized by a linear trend. However, the highest recoverable energy density (W_{rec}) and the highest electric field are achieved with a heating rate of 1 °C/s.

For all W_{rec}-electric field graphs of the BMN-BNT material, Figure 32 a), b), and c), it can be observed that the W_{rec} increases with higher electric field, while the efficiency behaves inversely - showing a decrease with higher electric field values. In general, an initial trend can be identified, indicating that films with low crystallization temperatures and high heating rates, as well as those with middle heating rates and middle crystallization temperatures, and finally, films with high crystallization temperatures and low heating rates, exhibit the best values for W_{rec} at high electric fields. Highest W_{rec}-values are reached for the films prepared with a $T_{cryst.}$ of 650°C.

In Figure 33, all the BMN-NN films produced at 650°C, 680°C, and 700°C and the different heating rates are depicted to illustrate the behavior of W_{rec} concerning the electric field. For Figure 33 a), corresponding to 650°C crystallization temperature, it is noteworthy that the highest electric field and the highest W_{rec} are achieved with the highest heating rate (30 °C/s).
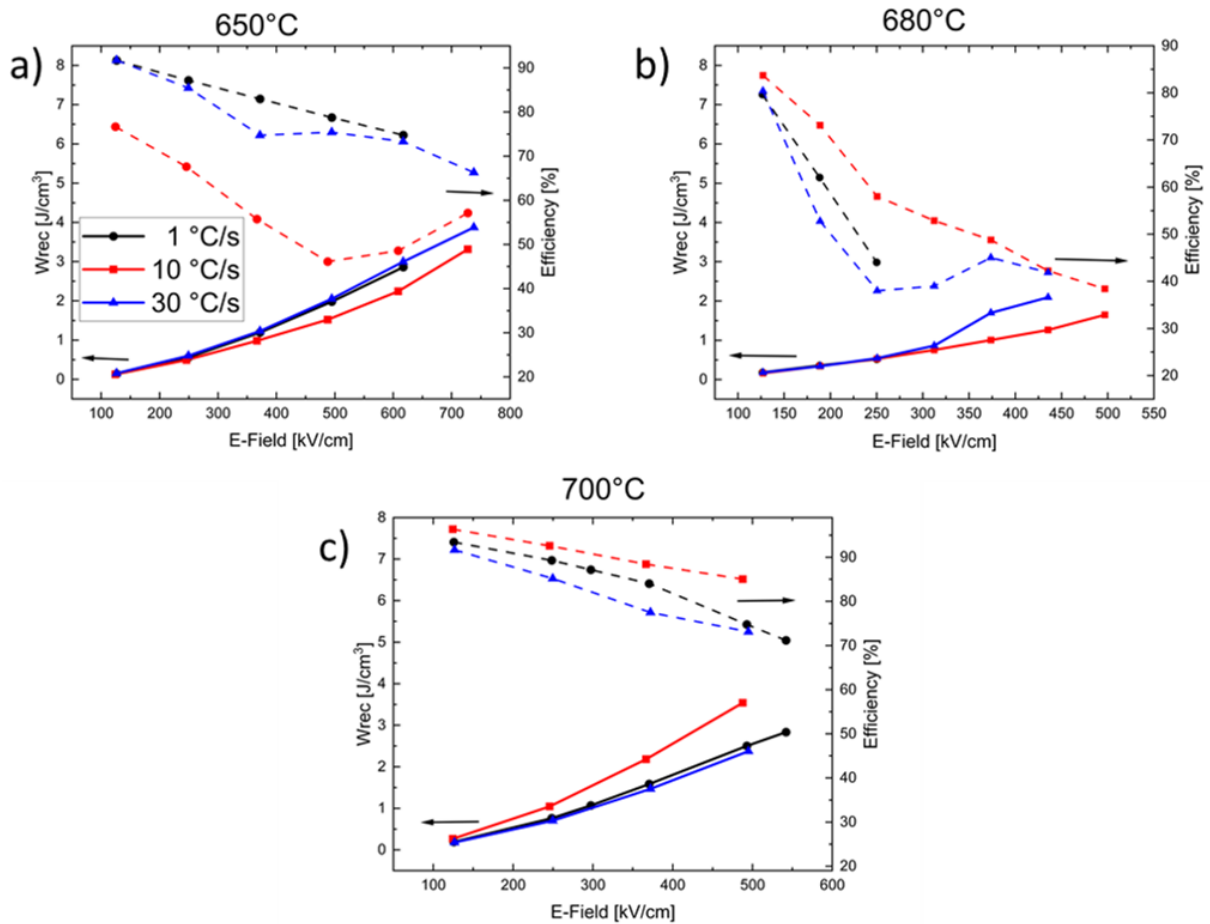
Figure 33: BMN-NN thin films: Behavior of varying heating rate at a) T_{cryst} = 650°C, b) $T_{cryst.}$ = 680°C and c) $T_{cryst.}$ = 700°C on electric field.

It should be noted that the efficiency for this temperature and also for Figure 33 b) varies significantly across different heating rates. Also, Figure 33 b) shows that the W_{rec} values are significantly lower compared to the values at lower and higher crystallization temperatures. The highest electric field can be achieved with films of a $T_{cryst.}$ of 650°C. (Figure 33 a) In general, it can be observed that, for this composition, lower electric fields are reached as for the material system BMN-BNT, and correspondingly, the values for W_{rec} are also lower.

4.4.1.2 Unipolar dynamic hysteresis measurements

In the field of microelectromechanical systems (MEMS), which are based on piezoelectric thin films, the electrical properties play an essential role in determining device functionality. Unipolar loops are of greater interest for applications, due to their special behavior and the possibility of achieving higher electric fields compared to bipolar measurements. Understanding and optimizing these electrical properties is critical to the effective performance of MEMS devices using piezoelectric thin films.
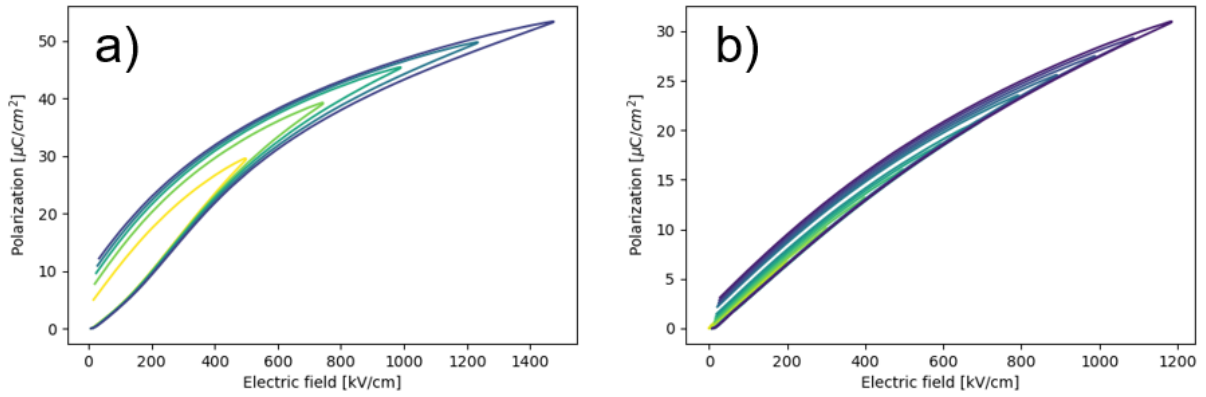
Figure 34: Unipolar PE loops up to the highest reachable electric field of a) BMN-BNT and b) BMN-NN.

In Figure 34 a) unipolar PE-loops of the BMN-BNT material system are shown. This observation shows that a considerable electric field is achieved, reaching up to 1400 kV/cm. In contrast, Figure 31 shows that the highest electric field achieved in bipolar BMN-BNT measurements is around 1000 kV/cm. For BMN-BNT as well, higher polarization values can be achieved compared to the bipolar measurements. A similar trend is observed in Figure 34 b) for the BMN-NN system. Additionally, it can be noted that the loops of the BMN-NN material exhibit a slimmer shape, with significantly higher polarization levels achievable compared to bipolar loops within the same system. It should be noted that a frequency of 10 kHz was selected for all these measurements. Due to the positive impact on achieving higher electric values, all subsequent measurements were conducted using a unipolar measurement setup.

For the upcoming comparison in terms of crystallization temperature, only films with high electric values for W_{rec} are highlighted. For example, films made from both the BMN-BNT and BMN-NN material systems, which were produced at a crystallization temperature of 680°C, exhibited low and insignificant electrical values, which makes them less relevant for applications and they therefore do not appear in the comparison.
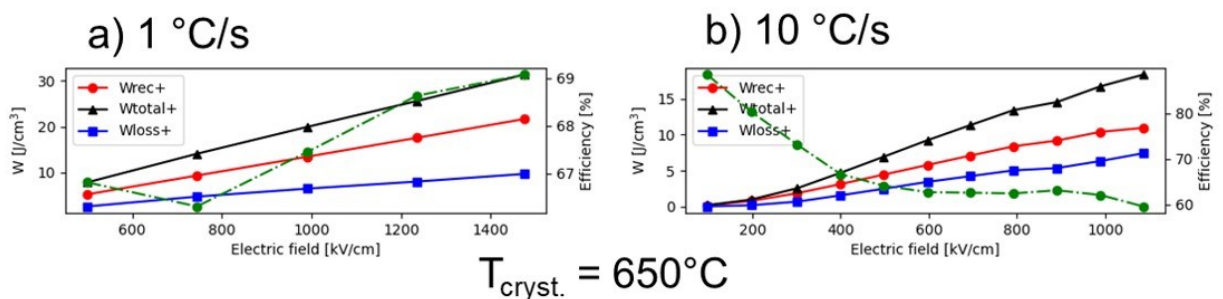

Figure 35: BMN-BNT unipolar loops and W_{rec} value over electric field comparison of different heating rates at $T_{cryst.}$ = 650°C.

49

In Figure 35 it can be seen that films produced at $T_{cryst.}$ = 650°C and a low heating rate of 1 °C/s, reach a high W_{rec} of around 20 J/cm³. The electrical values decrease with an increase in the heating rate. However, the efficiency at low heating rate (1 °C/s) remains relatively stable over a wide range of electric field values. Conversely, the efficiency at a heating rate of 10 °C/s exhibits fluctuations and experiences a significant decrease.
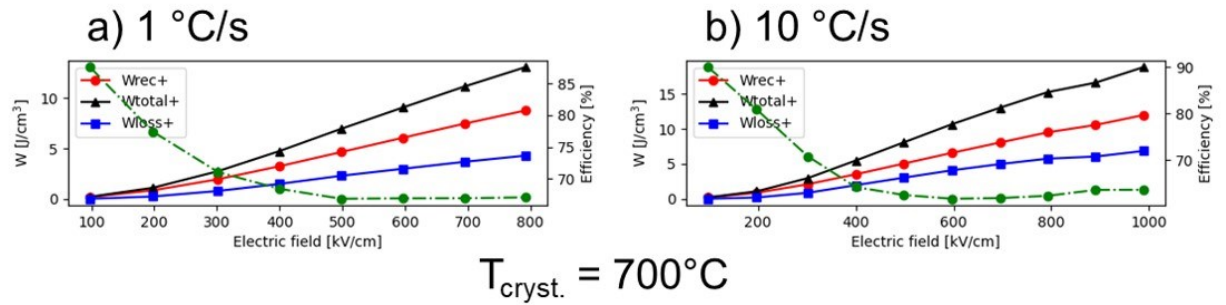

Figure 36: BMN-BNT unipolar loops and W_{rec} value over electric field comparison of different heating rates at $T_{cryst.}$ = 700°C.

Figure 36 displays the W_{rec} values of films produced with a crystallization temperature of 700°C. In both a) and b), the values fall within a similar range, yet they are lower compared to the films produced at 650°C (Figure 35). Additionally, the efficiency varies over a broad range. Although the electric field values are high, films with a crystallization temperature of 650°C (Figure 35) in the same system achieve even higher values.

For the forthcoming comparison of the BMN-NN system in Figure 37, only three films exhibited high electric values for W_{rec}. Namely, two films with a crystallization temperature of 650°C, one at a low (1 °C/s) and the other at a high (30 °C/s) heating rate, and one additional film with a heating rate of 10 °C/s and a higher crystallization temperature of 700°C are highlighted and they will be analyzed in the upcoming part in more detail.

In terms of W_{rec}, the highest value (≈ 13 J/cm³) is achieved with a $T_{cryst.}$ of 700°C and a heating rate of 10 °C/s. Additionally, for this thin film the efficiency values are higher compared to the other two films produced at $T_{cryst.}$ = 650°C. It's worth noting that high electric field values can be achieved for this system with all three films and the different synthesis parameters.
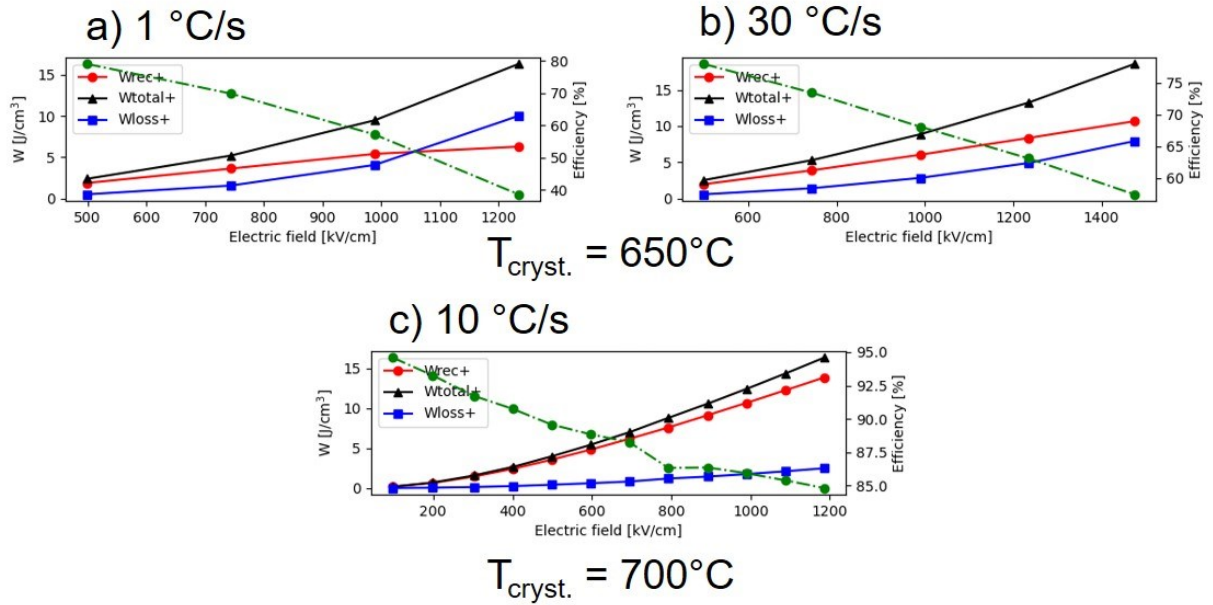
Figure 37: BMN-NN unipolar loops and W_{rec} value over electric field comparison of different heating rates at a) and b) $T_{cryst.}$ = 650°C and c) $T_{cryst.}$ = 700°C.

To generate an overview of all the produced films with varying processing parameters, it was essential to identify suitable parameters for a meaningful comparison. For both material systems, BMN-BNT and BMN-NN, the highest electric field all films could reach was 500 kV/cm. This served as the lower boundary for initiating a comparison based on the W_{rec} values of unipolar PE-loops. (see Figure 38) All measurements were conducted with a frequency of 10 kHz. In Figure 38 a), it is evident that, for the BMN-BNT material system, the highest values of W_{rec} at 500 kV/cm are achieved with a crystallization temperature of 700°C and a heating rate of 30 °C/s. It is important to note that the electric breakdown strength of this thin film occurred already at 500 kV/cm. However, as previously mentioned in Figure 35, the $T_{cryst.}$ = 650°C and a heating rate of 1 °C/s show high values for the W_{rec}. In general, it can be observed that for the BMN-NN system the best electric properties are attained for a low $T_{cryst.}$ and a low heating rate (1 °C/s), as well as for a high $T_{cryst.}$ and a high heating rate (30 °C/s).

The previously discussed result is reflected in Figure 38 b) as well. The highest W_{rec} values can be achieved with a high crystallization temperature of 700°C and a heating rate of 10 °C/s. The other two crystallization temperatures do not appear to be the optimal choices for reaching high values for W_{rec}.
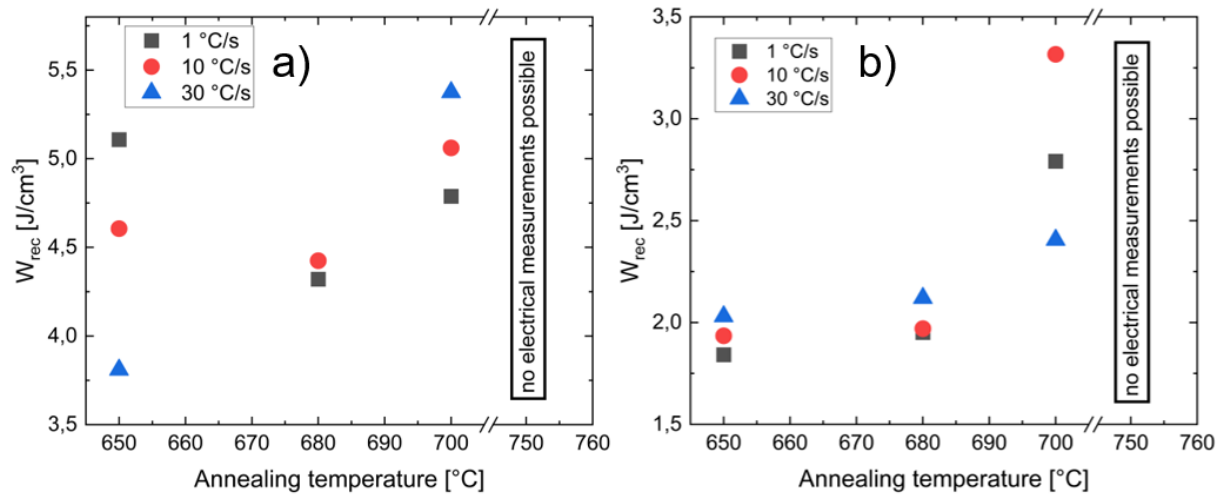
Figure 38: Comparison on W_{rec} at the same electric field (500 kV/cm) with different heating rates over the crystallization temperatures a) BMN-BNT and b) BMN-NN thin films.

As a reminder, and already mentioned in the beginning of this section, electrical measurements could not be carried out at a crystallization temperature of 750°C because of substrate failure. The high error rate led to a mixture of successful and unsuccessful attempts, so that no scientific conclusions could be drawn.

4.4.2 Leakage current density measurements

In Figure 39, the leakage current density versus the electric field is plotted for all BMN-BNT thin films. Films produced with a crystallization temperature of 650°C and heating rates of 1 °C/s and 30 °C/s, as well as $T_{cryst.}$ = 700°C and a heating rate of 1 °C/s, exhibit low leakage currents that increase with higher electric field. Meanwhile, the films with a crystallization temperature of 650°C and a 10 °C/s heating rate and $T_{cryst.}$ = 700°C with a 10 °C/s heating rate show low leakage currents at lower fields, but there is an increase at higher fields. In particular, at a crystallization temperature of 680°C and at heating rates of 1 °C/s and 10 °C/s, the leakage current density is high, indicating a higher conductivity. This is thought to come from the presence of secondary phases in small amounts, as also shown by XRD analysis, since metal oxides (MeO) are semiconducting and influence the conductivity of the thin films.
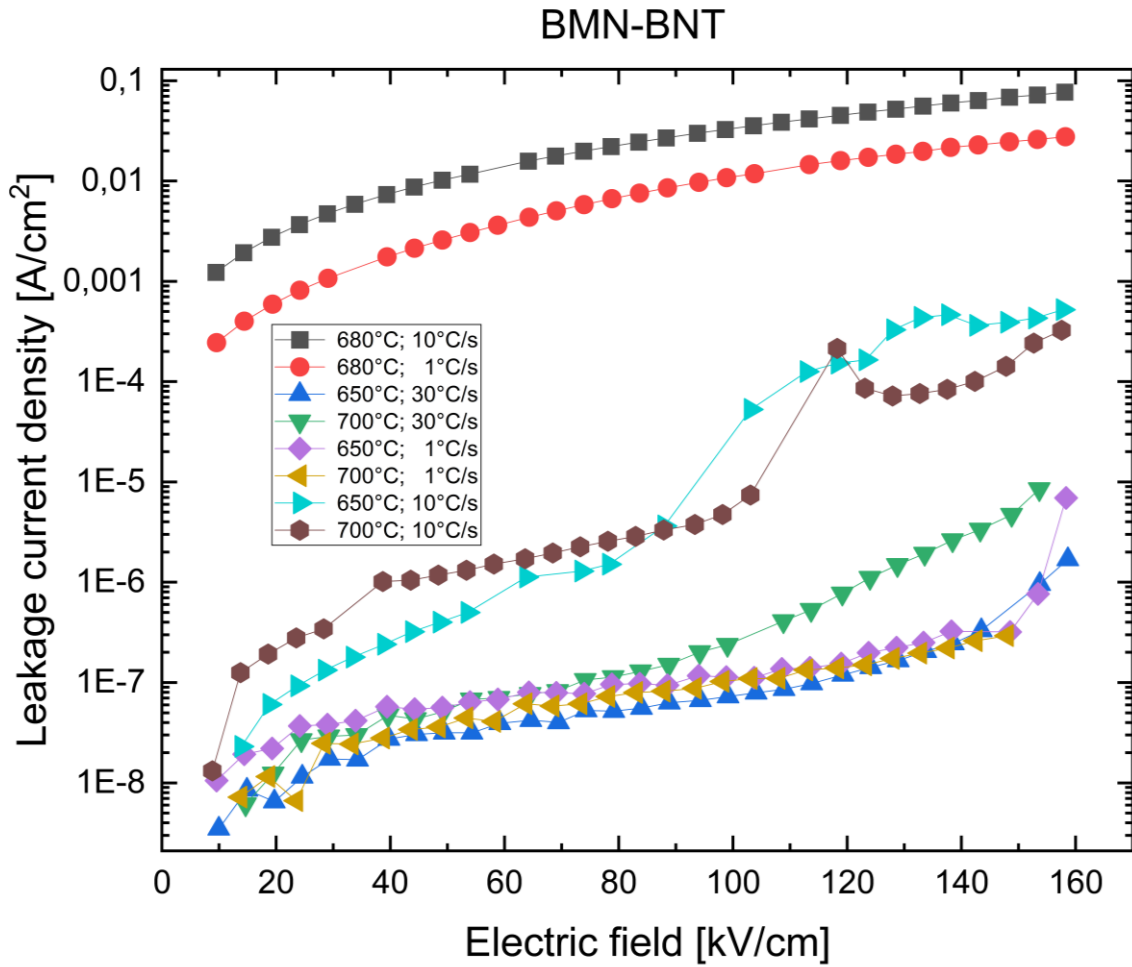
Figure 39: Leakage current density vs. applied DC electric field of BMN-BNT thin films.

The relationship between leakage current density and electric field for all BMN-NN thin films is illustrated in Figure 40. The films produced with a crystallization temperature of 700°C and a heating rate of 10 °C/s exhibit the lowest leakage current. Additionally, the film with a crystallization temperature of 650°C and a heating rate of 30 °C/s, as well as $T_{cryst.}$ = 700°C and 30 °C/s demonstrate a similar low-leakage current behavior. The different crystallization temperatures of 700°C and 650°C with the same heating rate of 1 °C/s show a slight increase of the leakage current at higher electric field. The only film that significantly deviates from the norm, starting from an electric field of 80 kV/cm, is produced at a crystallization temperature of 650°C and a heating rate of 10 °C/s. In general, it must be said that the BMN-NN system exhibits a much more stable behavior than BMN-BNT regarding the leakage current. All the films demonstrate lower conductivity levels compared to the other material system of BMN-BNT, within these three exceptions of the BMN-BNT material ($T_{cryst.}$ = 650°C and HR = 1 °C/s, $T_{cryst.}$ = 650°C and HR = 30 °C/s, $T_{cryst.}$ = 700°C and HR = 1 °C/s).

Additionally, it seems that the changing processing parameters do not significantly affect this material in terms of conductivity and leakage.
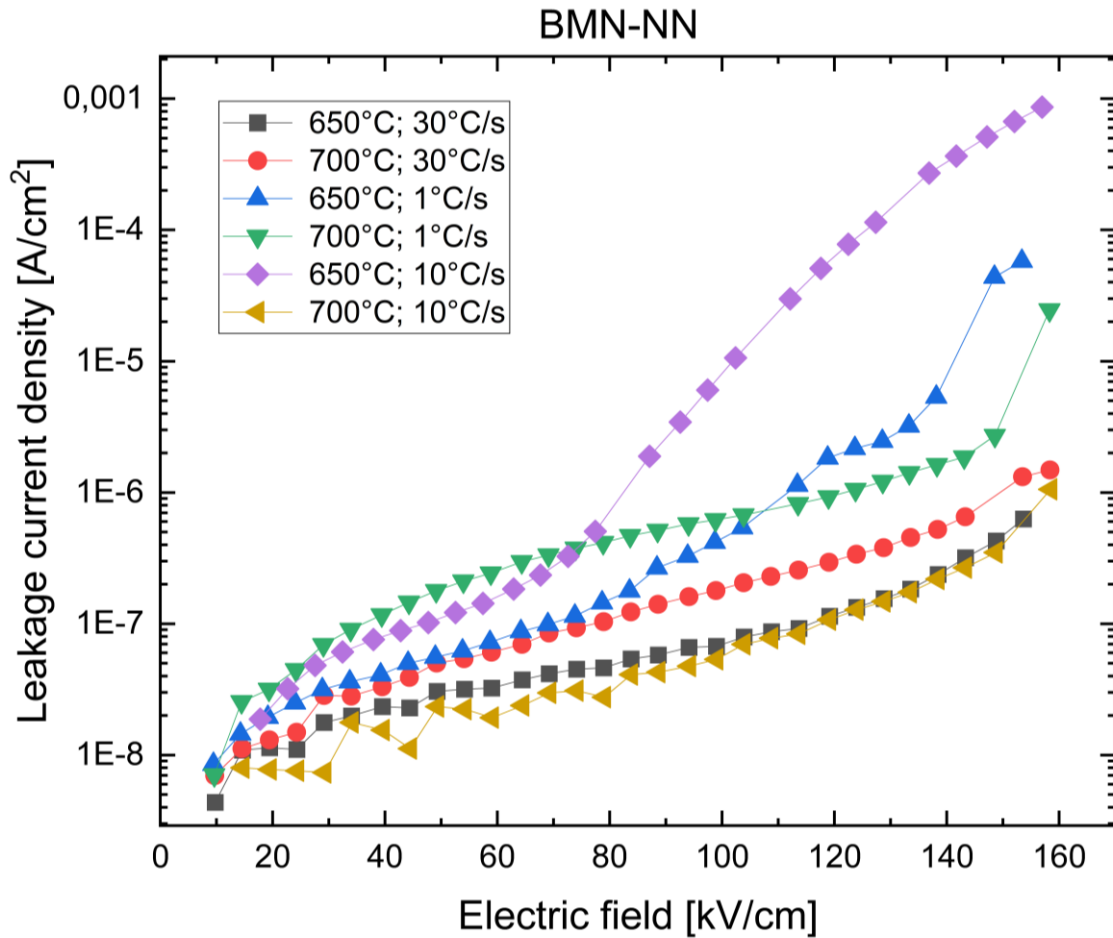

Figure 40: Leakage current density vs. applied DC electric field of BMN-NN thin films.

It must be noted that measurements were not possible for one film in the BMN-BNT system ($T_{cryst.}$ = 680°C and HR = 30 °C/s), and for the BMN-NN system, all samples prepared at a crystallization temperature of 680°C did not exhibit measurable leakage current behavior. Bubbles occurred at the interface on and next to the deposited Au electrodes while voltage was applied for the measurement, which may be an indication of E-field induced water hydrolysis. [50]

4.4.3 Temperature-dependent PE measurements

Figure 41 shows the temperature-dependent unipolar PE hysteresis curves for BMN-BNT thin films, produced at a crystallization temperature of 650°C, from 20°C to 140°C, respectively. All different three heating rates (Figure 41 a) 1 °C/s, b) 10 °C/s and c) 30 °C/s) show a slight increase of P_{max} with increasing temperature. However, the shift is relatively smaller for the 1 °C/s and 30 °C/s heating rates compared to the films produced with a 10 °C/s heating rate. There is a noticeable decrease in the level of polarization as the heating rates increase. Furthermore, the W_{rec} values remain relatively stable with increasing temperature for all heating rates, but the highest W_{rec} values are achieved with a heating rate of 1 °C/s, as also depicted in Figure 41a).
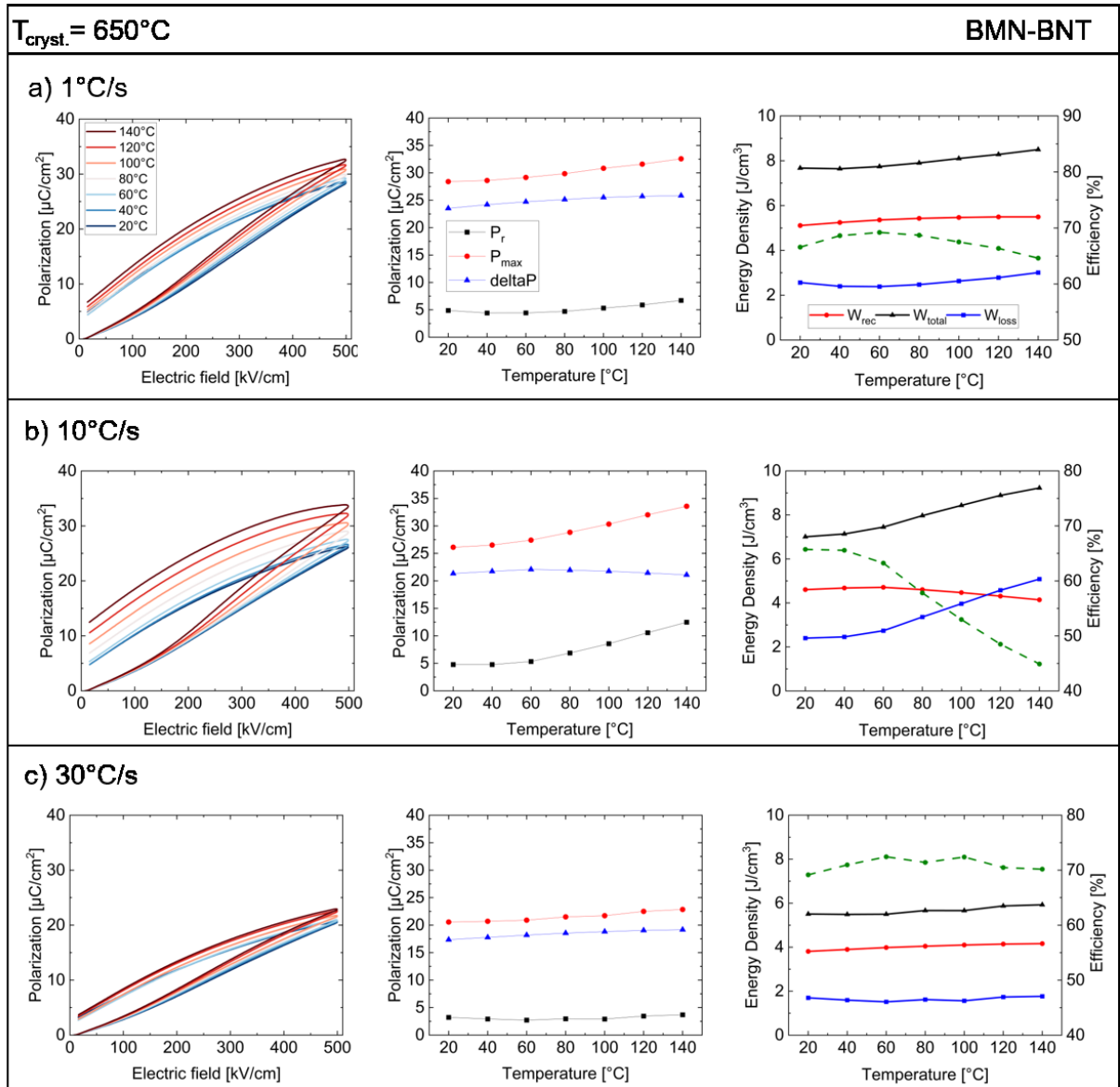
Figure 41: Temperature dependent DHM of BMN-BNT with $T_{cryst.}$ = 650°C.

The temperature-dependent PE hysteresis loops for the BMN-BNT thin films produced at a crystallization temperature of 700°C are illustrated in Figure 42, covering a temperature range from 20°C to 140°C. First it can be said that the P_{max} shows a slight increase as a function of temperature for all three heating rates. Additionally, P_{max} increases with the rising heating rates. It's noteworthy that the highest W_{rec} values can be reached accordingly to this fact at the highest heating rate (30 °C/s). In general, it can be stated that this material system has favorable properties with regard to temperature-dependent dynamic hysteresis measurements.
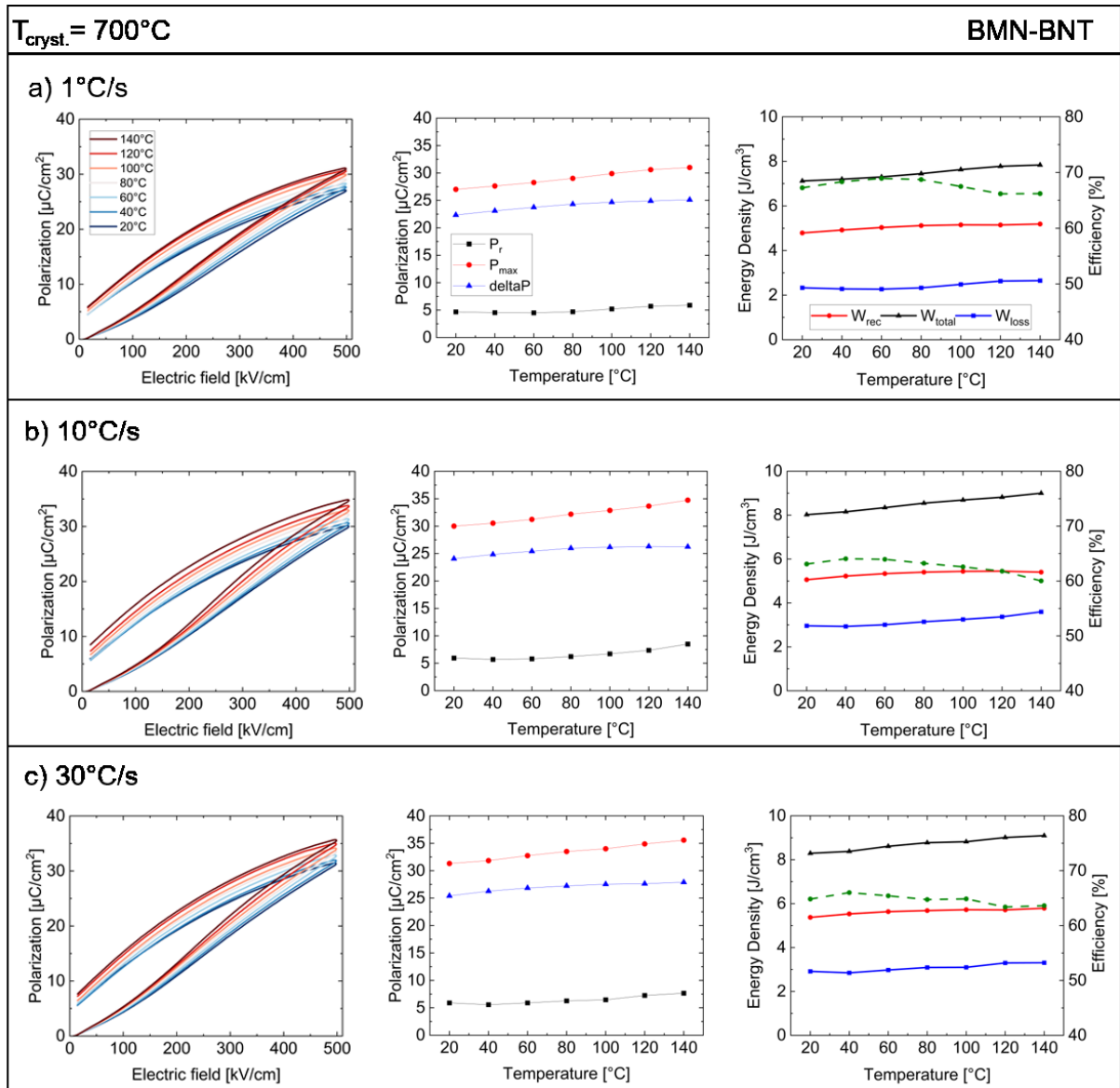
Figure 42: Temperature dependent DHM of BMN-BNT with $T_{cryst.}$ = 700°C.

Figure 43 shows the temperature-dependent PE hysteresis loop for the BMN-NN material system. The thin films in this Figure are produced at a crystallization temperature of 650°C, and are measured from 20°C to 140°C, respectively. As it can be seen in Figure 43 a) and b) the films show a stable behavior until 80°C, but over this temperature a blown-up loop appears and no significant interpretation can be provided anymore. This might be attributed to a thermally-activated leakage current mechanism that overlays the transient polarization current. Just the films produced with a heating rate of 30 °C/s (Figure 43 c) show a relatively stable behavior until a temperature of 140°C. The W_{rec} for this film is quite stable, but compared to the values in the following Figure 44 it is not the highest W_{rec}, which can be reached with this material. Therefore, a crystallization temperature of 650°C seems to be not the best option for achieving the highest and best properties with this material system.
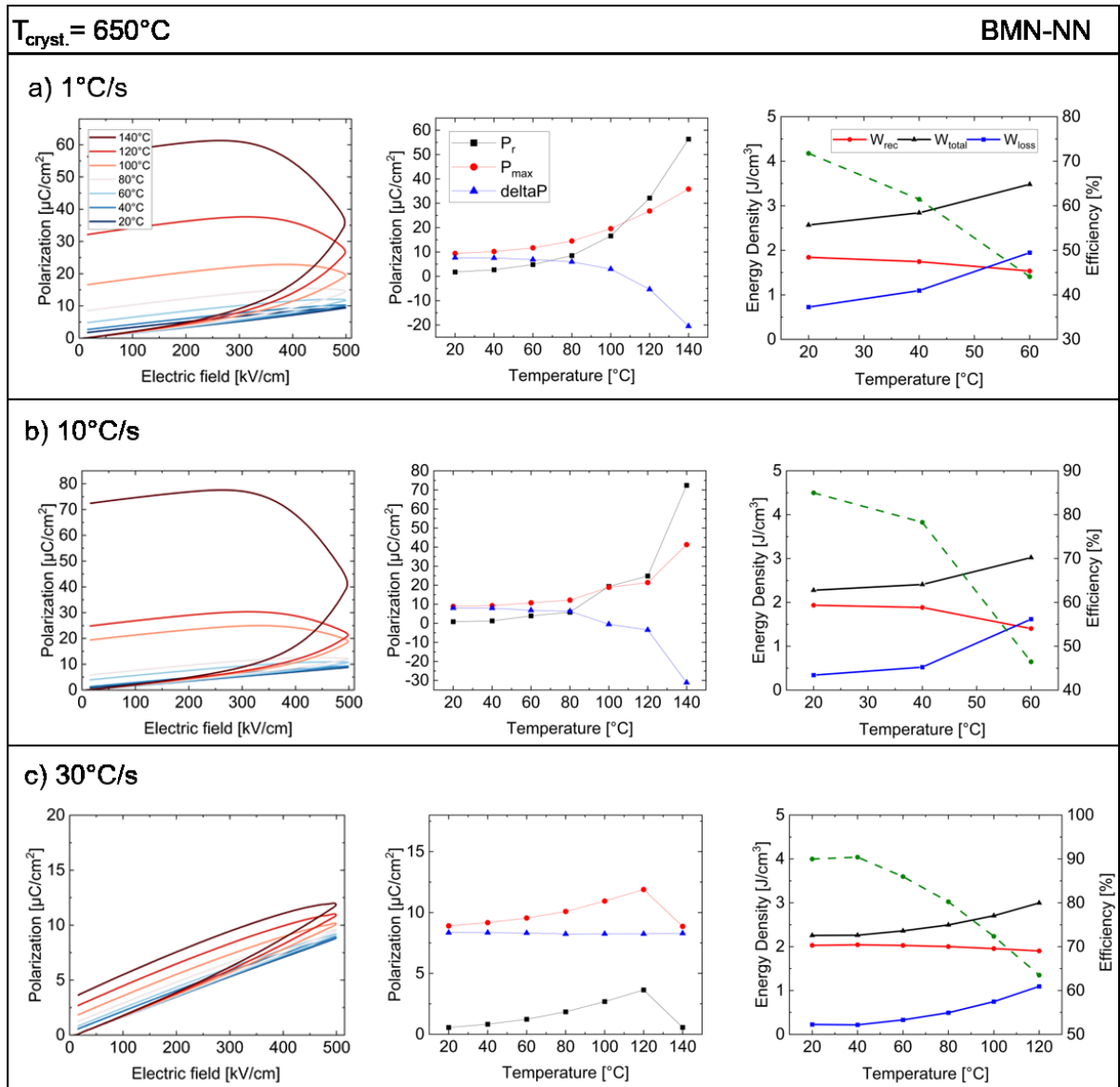
Figure 43: Temperature dependent DHM of BMN-NN with $T_{cryst.}$ = 650°C.

As already mentioned before, Figure 44 clearly demonstrates that temperature-dependent DHM works significantly better with the BMN-NN system at a crystallization temperature of 700°C for the produced films. A stable and slightly increasing behavior for P_{max} can be found for all three heating rates (Figure 44 a) 1 °C/s, b) 10 °C/s and c) 30 °C/s). The greatest and best properties, as well as the least shift of the temperature-dependent loops, can be observed for the heating rate of 10 °C/s. The uniform and stable efficiency behavior over the temperature range should also be highlighted.

In comparison with the other material system BMN-BNT it can be said that in general, the BMN-BNT material system shows higher and more promising properties with regard to temperature-dependent dynamic hysteresis measurements. However, BMN-NN thin films, produced with a crystallization temperature of 700°C, also exhibit a positive and stable behavior.
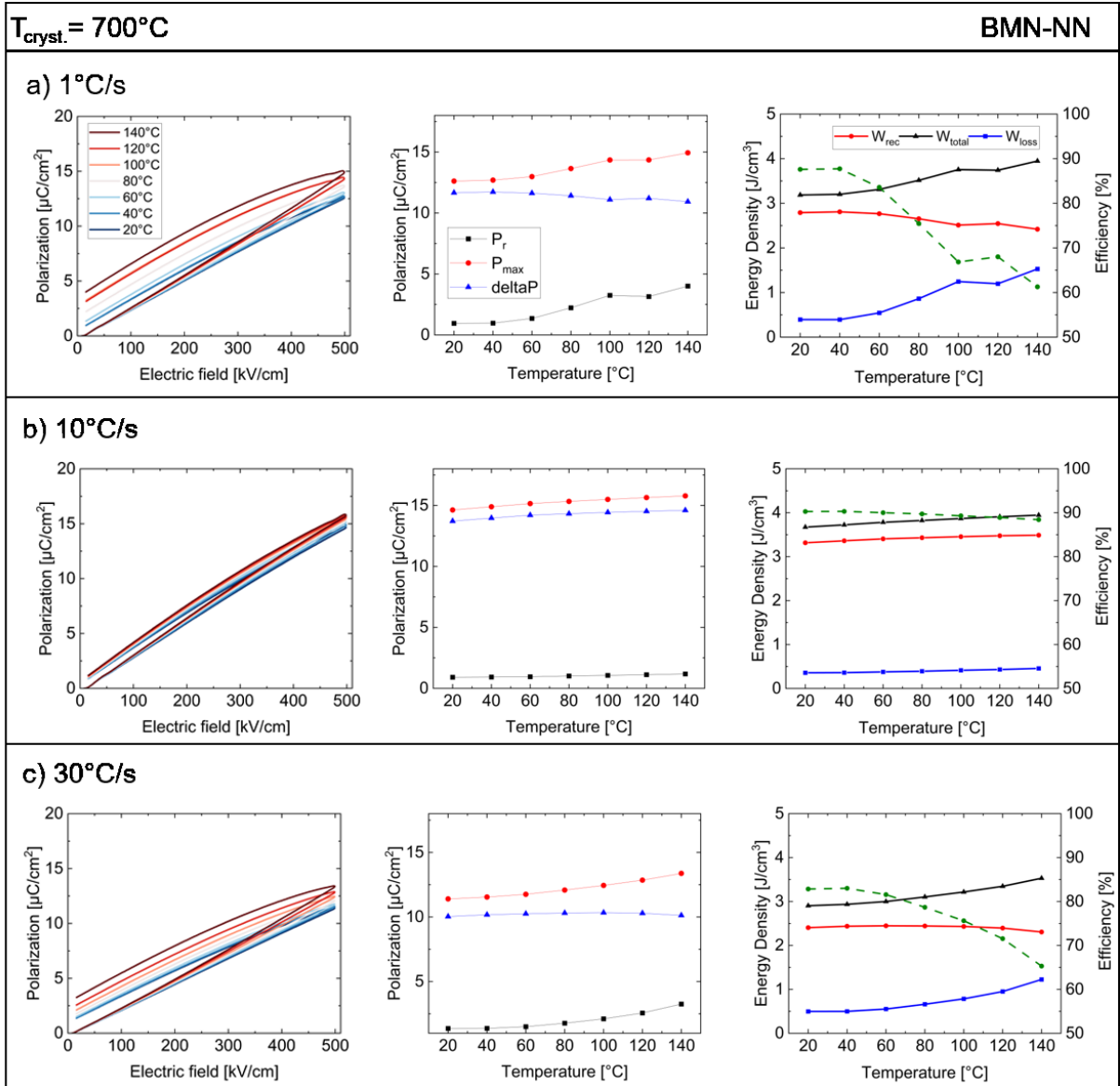
Figure 44: Temperature dependent DHM of BMN-NN with $T_{cryst.}$ = 700°C.

4.4.4 Fatigue measurements

The cyclic fatigue measurements of the MIM capacitors realized from both material systems were evaluated by subjecting them to 10^6 unipolar cycles at an electric field of 500 kV/cm and a frequency of 10 kHz. For each decade of cycling, three PE hysteresis measurements were performed while maintaining the same settings as the cycling conditions (500 kV/cm, 10 kHz). This approach was used to investigate changes in the appearance of the PE- loops and evaluate changes in critical properties relevant to capacitor applications during lifetime.

In Figure 45 all the films of the BMN-BNT material system produced at a crystallization temperature of 650°C are presented for cyclic fatigue measurements. In Figure 45 a) it can be observed that the films with a heating rate of 1 °C/s withstand 10^3 cycles before experiencing an irreversible breakdown of the dielectric. In the Figure 45 b, there is a slight decrease in the behavior of P_{max} and W_{rec} values observed until a breakdown after 10^4 cycles. The last heating rate at a crystallization temperature of 650°C demonstrates only minor continuous degradation of properties with the ongoing cycles, showing a high cyclic stability for a metal oxide based MIM and can be seen in Figure 45 c).
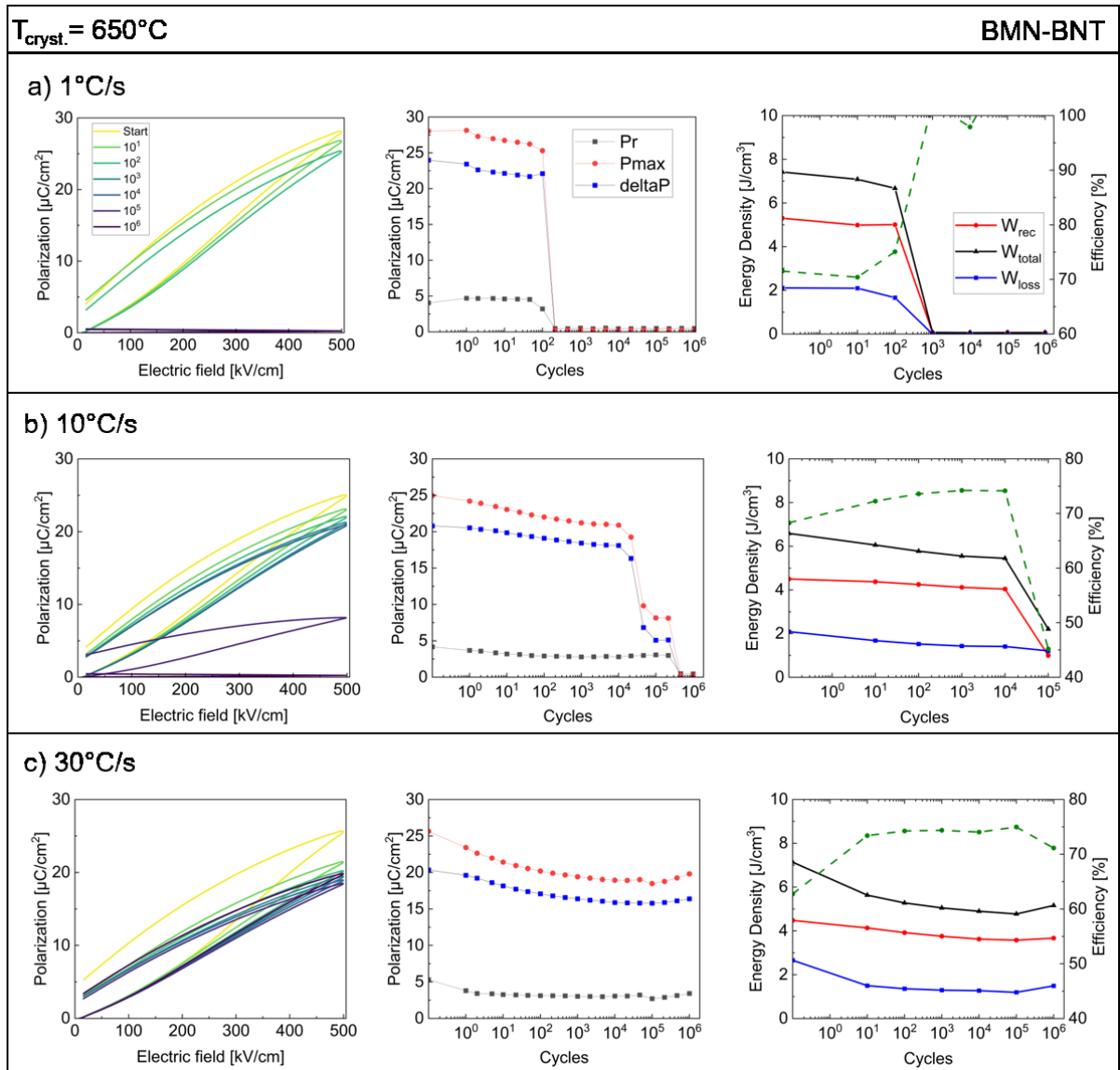
Figure 45: Fatigue measurements of BMN-BNT with $T_{cryst.}$= 650°C.

For cyclic fatigue measurements, Figure 46 presents all films within the BMN-BNT material system produced at a crystallization temperature of 700°C. In Figure 46 a) a stable fatigue behavior and consistent P_{max} can be observed up to 10^3 cycles. After this point, there is a significant decrease in the electric values (P_{max} and W_{rec}), but no breakdown of the dielectric occurs. In Figure 46 b), it is evident that the film experiences a breakdown after 10^2 cycles. Similarly, in Figure 46 c), an early breakdown of the dielectric occurs at 10^3 cycles. Generally, for the BMN-BNT system, it can be noted that the films produced at 650°C (see Figure 45) exhibit better fatigue properties than the films with a T_{cryst} = 700°C.
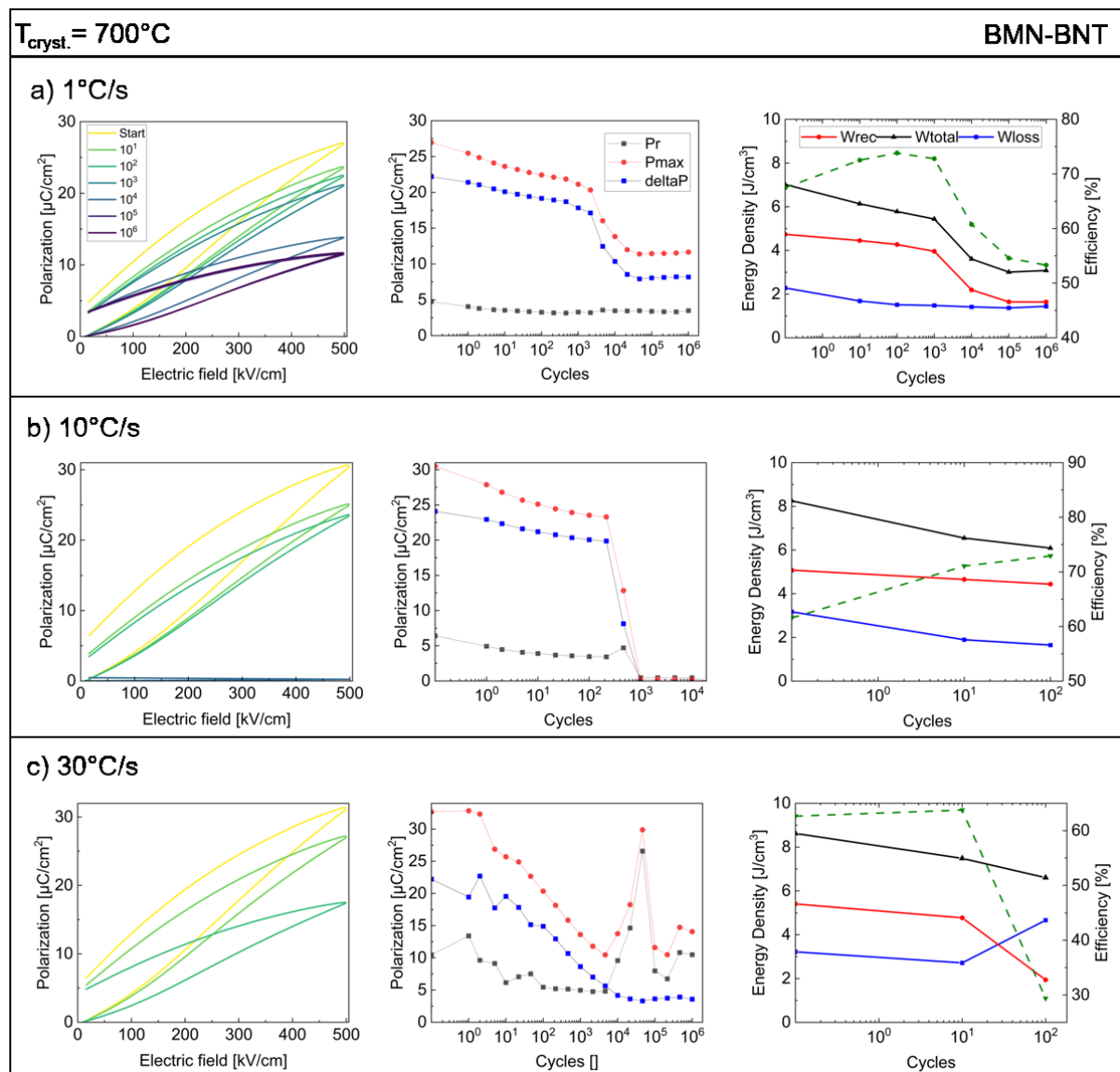
Figure 46: Fatigue measurements of BMN-BNT with $T_{cryst.}$ = 700°C.

Fatigue test have been also done for the BMN-NN material system. In Figure 47 all thin films with a crystallization temperature of 650°C are shown. Regarding Figure 47 a) it can be stated that, except for one data outlier at 10 cycles, the film sustains a high number of cycles until it reaches breakdown through the dielectric (10^6). Figure 47 b) and also Figure 47 c) show only slight, nearly not noticeable degradation of properties with the consecutive cycles, indicating high cyclic stability for this material system.
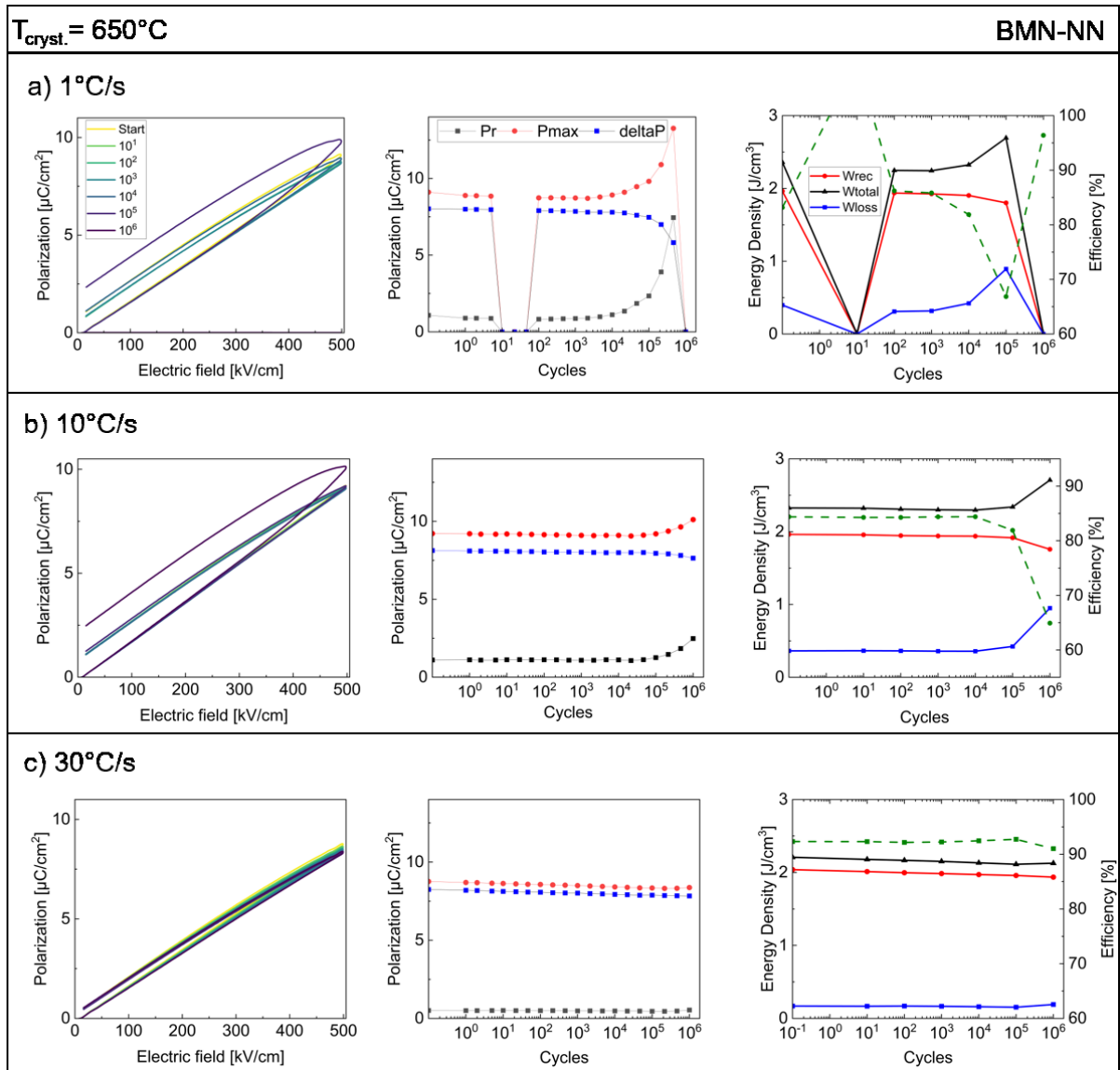
Figure 47: Fatigue measurements of BMN-NN with $T_{cryst.}$ = 650°C.

Figure 48 presents all the films of the BMN-NN material system produced with a crystallization temperature of 700°C that have undergone cyclic fatigue measurements. The behavior of the three different heating rates is similar. Between 10^5 and 10^6 cycles the films underwent a dielectric breakdown. However, until this point, the W_{rec} and P_{max} values are nearly unchanged, indicating no noticeable decrease in these values. This once again underlines the remarkable resistance of this BMN-NN material system to cyclic fatigue measurements and confirms its suitability for long-term applications and not just single-use scenarios. This robust performance highlights the materials durability and reliability under recurring loading conditions.

63
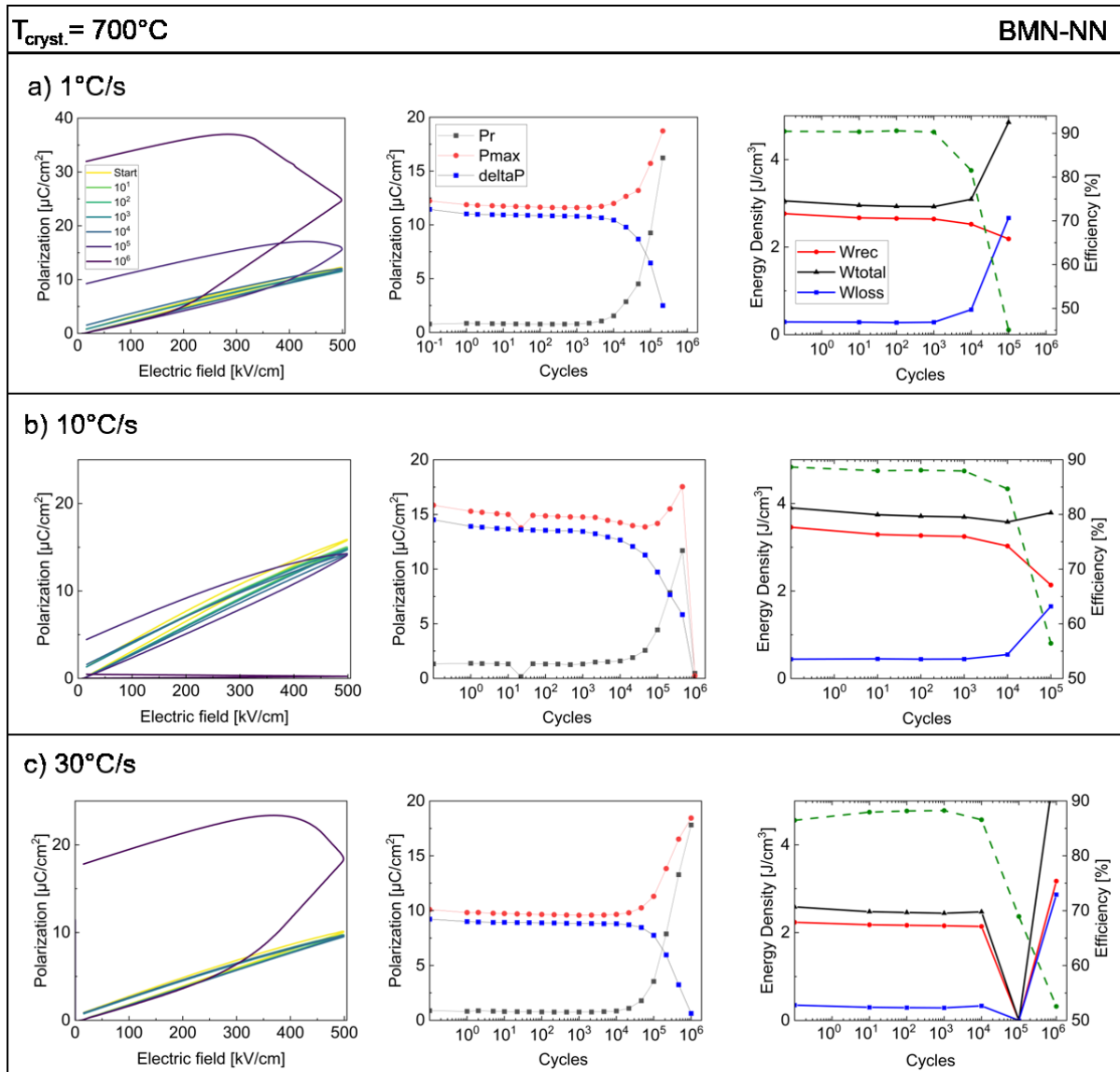
Figure 48: Fatigue measurements of BMN-NN with $T_{cryst.}$ = 700°C.

In Table 5, the percentage variation of the energy properties relative to cycles before breakdown is calculated and presented. This analysis provides valuable insight into the performance degradation of materials with repeated cycling and allows a quantitative assessment of the evolution of energy properties with prolonged use. By quantifying the percentage variation, a better understanding of the material's resilience and stability under cyclic loading conditions, allowing decisions regarding its suitability for long-term applications, can be made. This data is critical for optimizing material selection and design to ensure durability and reliability in real-world operating scenarios.

Table 5: Percentage of variation of energy storage properties for BMN-BNT and BMN-NN thin films.

Material system	$T_{cryst.}$ [°C]	Heating rate [°C/s]	Cycles []	W_{rec} [%]	W_{total} [%]	W_{loss} [%]	Efficiency [%]
BMN-BNT	650	1	10^2	5.58	10.05	21.27	3.55
	650	10	10^4	10.22	17.32	32.60	5.86
	650	30	10^6	18.02	27.69	43.97	8.39
	700	1	10^3	16.45	22.54	35.19	5.31
	700	1	10^6	25.10	14.61	1.60	7.46
	700	10	10^2	12.60	26.21	48.01	11.36
	700	30	10^2	64.07	23.42	30.91	33.25
BMN-NN	650	1	10^5	8.22	12.42	55.53	16.32
	650	10	10^6	10.44	14.11	61.79	19.48
	650	30	10^6	5.09	3.74	11.12	1.30
	700	1	10^5	20.89	37.01	89.06	45.38
	700	10	10^5	38.20	02.90	73.21	32.24
	700	30	10^4	4.26	4.37	5.10	0.10

5   Conclusion and Outlook

The investigation of lead-free dielectric capacitors, with a specific focus on the thin film systems BMN-BNT and BMN-NN, involving variations in heating rates and crystallization temperatures, has provided valuable insights into their process-structure-property relationships.

Stable precursor solutions were prepared, and both systems were successfully synthesized using chemical solution deposition on $Pt/TiO_2/SiO_2/Si$ substrates. All the films exhibited perovskite phase to a certain degree and process conditions that avoid the presence of secondary phases were identified. The perovskite structure was confirmed by Raman spectroscopy and X-ray diffraction. A comprehensive characterization protocol, including scanning electron microscopy, and energy-dispersive X-ray analysis, has contributed to a detailed understanding of the microstructural features, showing a change in nucleation and a Ti segregation at nanoscale, depending on processing parameters. It was discovered that the impact on the microstructure from different crystallization temperatures is more pronounced than the influence of varying heating rates. The XRD analysis revealed variations in the (111) peak position, suggesting the presence of secondary phases that affect the overall lattice constant of the measured volume, even though the material composition itself was not changed. These variations indicate potential deviations from phase purity at a very small scale, supported by the absence of distinct peaks in the spectrum except for the one at $T_{cryst.}$ = 680°C. Electrical measurements could confirm this finding and showed higher leakage and/or poorer energy storage properties in films with such peak fluctuations. This could be attributed to the nucleation-growth behavior of the thin films, which is associated with the presence of a non-equilibrium phase and the specific characteristics of a diffusion barrier-driven process. Additionally, the nucleation process is significantly influenced by decomposition reactions and the annealing conditions.

Additionally, electrical measurements have provided insights into the electrical properties of the thin films. This covered evaluating the energy storage properties through polarization vs. electric field hysteresis loops (bipolar and unipolar), understanding the temperature-dependent responses, conducting measurements on the behavior of leakage current density, and exploring cyclic fatigue behaviors, all relevant for applications. Firstly, the BMN-BNT composition ($T_{cryst.}$ = 650°C and HR = 1 °C/s) exhibited promising energy storage properties, as measured in a unipolar polarization vs. electric field hysteresis loop (PE loop), achieving a W_{rec} of approximately 20 J/cm³ with an efficiency of 69%. Similarly, for BMN-NN ($T_{cryst.}$ = 700°C and HR = 10 °C/s) under the same conditions, a W_{rec} of 13 J/cm³ and an efficiency of 84% were obtained. In the context of leakage current density measurements, all BMN-

NN films exhibited low leakage currents and low conductivity levels. In contrast, for BMN-BNT, only a few prepared films ($T_{cryst.}$ = 650°C and HR = 1 °C/s also HR = 30 °C/s) demonstrated low leakage current density. Regarding thermal stability hysteresis measurements up to 140°C, the BMN-BNT materials exhibited the most favorable values and behavior for films with a crystallization temperature of 700°C and heating rates of 10 °C/s and 30 °C/s. BMN-NN exhibited unfavorable behavior for films with a crystallization temperature of 650°C. However, for a T_{cryst} of 700°C and a HR of 10 °C/s, relatively good values were obtained, although still lower than those for the BMN-BNT system. On the other hand, the BMN-NN system demonstrated superior cyclic fatigue stability for all prepared films with a $T_{cryst.}$ of 650°C, enduring up to 10^6 unipolar cycles. Additionally, the thin films with $T_{cryst.}$ = 700°C exhibited also good values although a best-case breakdown for all of them occurred around 10^5 unipolar cycles. For the BMN-BNT only one film, with a T_{cryst} = 650°C and a HR = 30 °C/s, showed promising fatigue behavior.

The optimal conditions for the thin films depend on the specific requirements, with considerations for polarization vs. electric field hysteresis loops (PE loops), leakage current, fatigue behavior, and temperature stability. Let's first focus on the BMN-BNT material system. For the PE loops and leakage current measurements, a thin film with a $T_{cryst.}$ of 650°C and a HR of 1 °C/s appears to be a favorable choice. However, for fatigue behavior, although $T_{cryst.}$ of 650°C is still preferred, a higher heating rate yields better properties. Temperature stability is maintained across all BMN-BNT films, but the best overall properties are observed for $T_{cryst.}$ = 700°C with HR = 10 °C/s and HR = 30 °C/s. In BMN-NN thin films, the most promising candidate for PE loops, leakage, and temperature-dependent measurements is the specimen with a $T_{cryst.}$ of 700°C and a HR of 10 °C/s. This particular film exhibits standout performance across these crucial parameters. One last thing to note is that better stability is evident in the fatigue measurements of BMN-NN produced with a $T_{cryst.}$ of 650°C.

In general, the observed variations in the process parameters have proven to significantly impact both, the microstructure and the electrical properties. The interplay between these structural characteristics and electrical behavior underscores the necessity for a further investigation of processing conditions to achieve tailored material properties. The materials will undergo further analysis, and research will be conducted, exploring compositions in a range around the investigated composition of this thesis. These discovered values for the crystallization temperature and heating rate provide a solid foundation for future investigations and serve as valuable references for various applications and measurements of BMN-based material systems. The proposed application scenarios for the fabricated materials, such as BMN-BNT for energy storage capacitors in non-cyclic applications such as peak power balancing in IoT systems and BMN-NN for cyclic applications in IoT or cell phones,

demonstrate a strategic use of advanced materials to meet specific performance requirements in different technology areas. By tailoring materials to the particular requirements of different applications, such as optimizing energy storage capacity and durability in non-cyclic scenarios versus prioritizing cyclic stability and efficiency in mobile devices, these strategies demonstrate a nuanced understanding of material properties and their practical implications. This targeted approach not only improves the overall functionality and efficiency of devices, but also emphasizes the importance of material innovation in advancing technological capabilities in various fields.

6 References

[1] V. Veerapandiyan, F. Benes, T. Gindel, and M. Deluca, "Strategies to Improve the Energy Storage Properties of Perovskite Lead-Free Relaxor Ferroelectrics: A Review," *Materials*, vol. 13, no. 24, p. 5742, 2020, doi: 10.3390/ma13245742.

[2] M. E. Lines, *Principles and applications of ferroelectrics and related materials*. Oxford: Clarendon Press, 2009.

[3] P. Office, "Richtlinie 2011/65/EU des Europäischen Parlaments und des Rates vom 8. Juni 2011 zur Beschränkung der Verwendung bestimmter gefährlicher Stoffe in Elektro- und ElektronikgerätenText von Bedeutung für den EWR," [Online]. Available: https://www.ce-richtlinien.eu/richtlinien/RoHS/Richtlinie/RL_ RoHS_2011_65_EU.pdf

[4] A. M. Kobald, H. Kobald, and M. Deluca, "Phase stability and energy storage properties of polycrystalline antiferroelectric BaTiO3-substituted NaNbO3 thin films," *Journal of the European Ceramic Society*, 2023, doi: 10.1016/j.jeurceramsoc.2023.11.071.

[5] S. R. Elliott, *The physics and chemistry of solids,* 2008th ed. Chichester, Weinheim: Wiley, 2008.

[6] D. Damjanovic, "Ferroelectric, dielectric and piezoelectric properties of ferroelectric thin films and ceramics," *Rep. Prog. Phys.*, vol. 61, no. 9, pp. 1267–1324, 1998, doi: 10.1088/0034-4885/61/9/002.

[7] L. Jin, F. Li, and S. Zhang, "Decoding the Fingerprint of Ferroelectric Loops: Comprehension of the Material Properties and Structures," *J. Am. Ceram. Soc.*, vol. 97, no. 1, pp. 1–27, 2014, doi: 10.1111/jace.12773.

[8] A. Pramanick, A. D. Prewitt, J. S. Forrester, and J. L. Jones, "Domains, Domain Walls and Defects in Perovskite Ferroelectric Oxides: A Review of Present Understanding and Recent Contributions," *Critical Reviews in Solid State and Materials Sciences*, vol. 37, no. 4, pp. 243–275, 2012, doi: 10.1080/10408436.2012.686891.

[9] G. H. Haertling, "Ferroelectric thin films for electronic applications," *Journal of Vacuum Science & Technology A*, vol. 9, no. 3, pp. 414–420, 1991, doi: 10.1116/1.577424.

[10] I. Burn and D. M. Smyth, "Energy storage in ceramic dielectrics," (in En;en), *J Mater Sci*, vol. 7, no. 3, pp. 339–343, 1972, doi: 10.1007/BF00555636.

[11] H. Zhang *et al.,* "A review on the development of lead-free ferroelectric energy-storage ceramics and multilayer capacitors," *J. Mater. Chem. C*, vol. 8, no. 47, pp. 16648–16667, 2020, doi: 10.1039/D0TC04381H.

[12] P. Muralt, "Ferroelectric thin films for micro-sensors and actuators: a review," *J. Micromech. Microeng.*, vol. 10, no. 2, pp. 136–146, 2000, doi: 10.1088/0960-1317/10/2/307.

[13] F. T. Ulaby, E. Michielssen, and U. Ravaioli, *Fundamentals of applied electromagnetics,* 6th ed. Boston: Prentice Hall, 2010.

[14] K. Uchino, *Ferroelectric devices,* 2nd ed. Boca Raton: CRC Press, 2010. [Online]. Available: https://www.taylorfrancis.com/books/mono/10.1201/b15852/ ferroelectric-devices-kenji-uchino

[15] T. Schneller, R. Waser, M. Kosec, and D. Payne, Eds., *Chemical solution deposition of functional oxide thin films*. Wien, Heidelberg, New York, Dordrecht, London: Springer, 2013. [Online]. Available: https://search.ebscohost.com/ login.aspx?direct=true&scope=site&db=nlebk&db=nlabk&AN=691483

[16] R. W. Schwartz, "Chemical Solution Deposition of Perovskite Thin Films," *Chem. Mater.,* vol. 9, no. 11, pp. 2325–2340, 1997, doi: 10.1021/cm970286f.

[17] K. Bakken, "In situ Characterization of Ferroelectric Oxide Thin Films during Aqueous Chemical Solution Deposition," *1503-8181*, 2020. [Online]. Available: https://ntnuopen.ntnu.no/ntnu-xmlui/handle/11250/2652461

[18] K.-N. Pham *et al.,* "Epitaxial K0.5Na0.5NbO3 thin films by aqueous chemical solution deposition," *Royal Society open science*, vol. 6, no. 1, p. 180989, 2019, doi: 10.1098/rsos.180989.

[19] C. J. Brinker and G. W. Scherer, *Sol-gel science: The physics and chemistry of sol-gel processing*. Boston: Academic Press, 1990.

[20] R. W. Schwartz, T. Schneller, and R. Waser, "Chemical solution deposition of electronic oxide films," *1631-0748*, vol. 7, no. 5, pp. 433–461, 2004, doi: 10.1016/j.crci.2004.01.007.

[21] N. Bassiri-Gharb, Y. Bastani, and A. Bernal, "Chemical solution growth of ferroelectric oxide thin films and nanostructures," *Chem. Soc. Rev.*, vol. 43, no. 7, pp. 2125–2140, 2014, doi: 10.1039/C3CS60250H.

[22] S. Halder, T. Schneller, and R. Waser, "Enhanced stability of platinized silicon substrates using an unconventional adhesion layer deposited by CSD for high temperature dielectric thin film deposition," (in En;en), *Appl. Phys. A*, vol. 87, no. 4, pp. 705–708, 2007, doi: 10.1007/s00339-007-3866-3.

[23] C. T. Shelton *et al.,* "Chemically Homogeneous Complex Oxide Thin Films Via Improved Substrate Metallization," *Adv Funct Materials*, vol. 22, no. 11, pp. 2295–2302, 2012, doi: 10.1002/adfm.201103077.

[24] J. W. Schmelzer, A. S. Abyzov, V. M. Fokin, C. Schick, and E. D. Zanotto, "Crystallization of glass-forming liquids: Maxima of nucleation, growth, and overall crystallization rates," *Journal of Non-Crystalline Solids*, vol. 429, pp. 24–32, 2015, doi: 10.1016/j.jnoncrysol.2015.08.023.

[25] X. Y. Liu, "Heterogeneous nucleation or homogeneous nucleation?," *The Journal of Chemical Physics*, vol. 112, no. 22, pp. 9949–9955, 2000, doi: 10.1063/1.481644.

[26] A. Gautam, P. Komal, P. Gautam, A. Sharma, N. Kumar, and J. P. Jung, "Recent Trends in Noble Metal Nanoparticles for Colorimetric Chemical Sensing and Micro-Electronic Packaging Applications," *Metals*, vol. 11, no. 2, p. 329, 2021, doi: 10.3390/met11020329.

[27] D. J. Gardiner and P. R. Graves, Eds., *Practical Raman Spectroscopy*. Berlin, Heidelberg: Springer Berlin Heidelberg, 1989.

[28] D. J. Gardiner, "Introduction to Raman Scattering," in *Practical Raman Spectroscopy*, D. J. Gardiner and P. R. Graves, Eds., Berlin, Heidelberg: Springer Berlin Heidelberg, 1989, pp. 1–12. [Online]. Available: https://link.springer.com/chapter/10.1007/978-3-642-74040-4_1

[29] Department of Materials Science and Metallurgy - University of Cambridge, *Raman Spectroscopy (all content).* [Online]. Available: https://www.doitpoms.ac.uk/tlplib/raman/printall.php (accessed: Jan. 16 2024).

[30] D. A. Long, *The Raman effect: A unified treatment of the theory of Raman scattering by molecules,* 1st ed. Chichester: Wiley, 2002.

[31] J. M. Chalmers, Ed., *Handbook of vibrational spectroscopy.* Chichester, Weinheim: Wiley, 2002.

[32] W. Zhou, R. Apkarian, Z. L. Wang, and D. Joy, "Fundamentals of Scanning Electron Microscopy (SEM)," in *Scanning Microscopy for Nanotechnology: Techniques and Applications*, W. Zhou, Ed., New York, NY: Springer New York, 2007, pp. 1–40.

[33] J. Goldstein, D. E. Newbury, J. R. Michael, N. W. M. Ritchie, J. H. J. Scott, and D. C. Joy, *Scanning electron microscopy and X-ray microanalysis*. New York, NY, U.S.A.: Springer, 2018.

[34] Schmid T., *Scanning-electron microscopy.* [Online]. Available: https://fakultaeten.hu-berlin.de/en/mnf/forschung_internationales/grs/salsa/p-a-labs/application-lab/instrumentation/a-labs-sem (accessed: Jan. 9 2024).

[35] J. Epp, "4 - X-ray diffraction (XRD) techniques for materials characterization," in *Woodhead Publishing series in electronic and optical materials*, number 88, *Materials characterization using nondestructive evaluation (NDE) methods*, G. Hübschen, I. Altpeter, R. Tschuncky, and H.-G. Herrmann, Eds., Amsterdam, Boston, Cambridge: Elsevier/WP Woodhead Publishing, 2016, pp. 81–124. [Online]. Available: https://www.sciencedirect.com/science/article/pii/B9780081000403000043

[36] M. Birkholz, *Thin film analysis by X-Ray scattering,* 2nd ed. Weinheim: WILEY-VCH, 2009.

[37] Mohsin Raza, "Oxygen vacancy stabilized zirconia (OVSZ); synthesis and properties," Unpublished, 2017.

[38] G. F. Harrington and J. Santiso, "Back-to-Basics tutorial: X-ray diffraction of thin films," (in En;en), *J Electroceram*, vol. 47, no. 4, pp. 141–163, 2021, doi: 10.1007/s10832-021-00263-6.

[39] L. Ode, M. Hikam, B. Soegijono, and A. Sudarmaji, "The Electrical Hysteresis Loop and Polarization Value of BaZrxTi1-xO3 Multilayer Films Material at Different Annealing Temperature (x = 0.1 and 0.08) based on Sawyer Tower Circuit," *2014 International Conference on Physics and its Applications (ICOPIA-14)*, pp. 41–48, 2014, doi: 10.2991/icopia-14.2015.8.

[40] R. Bouregba and G. Poullain, "Computation of the polarization due to the ferroelectric layer in a stacked capacitor from Sawyer–Tower hysteresis measurements," *J. Appl. Phys.*, vol. 93, no. 1, pp. 522–532, 2003, doi: 10.1063/1.1527212.

[41] aixACCT Systems GmbH, *Manual TF Analyzer 3000 / Vers. 5.0.M2: Manual TF Analyzer 3000 / Vers. 5.0.M2*.

[42] Y. Hamazaki, W. Sakamoto, M. Moriya, and T. Yogo, "Effects of BaTiO 3 Content and Mn Doping on Ferroelectric Properties of NaNbO 3 –BaTiO 3 Thin Films Prepared by Chemical Solution Deposition," *Jpn. J. Appl. Phys.*, vol. 48, no. 9, 09KA08, 2009, doi: 10.1143/JJAP.48.09KA08.

[43] W. Sakamoto, Y. Hamazaki, H. Maiwa, M. Moriya, and T. Yogo, "Lead-free piezoelectric thin films of Mn-doped NaNbO3–BaTiO3 fabricated by chemical solution deposition," *Thin Solid Films*, vol. 518, no. 15, pp. 4256–4260, 2010, doi: 10.1016/j.tsf.2009.12.102.

[44] A. Bencan *et al.,* "Atomic scale symmetry and polar nanoclusters in the paraelectric phase of ferroelectric materials," *Nat Commun*, vol. 12, no. 1, p. 3509, 2021, doi: 10.1038/s41467-021-23600-3.

[45] A. Nesterović *et al.,* "Structure and dielectric properties of (1-x)Bi0.5Na0.5TiO3-xBaTiO3 piezoceramics prepared using hydrothermally synthesized powders," *Royal Society open science*, vol. 8, no. 7, p. 202365, 2021, doi: 10.1098/rsos.202365.

[46] T. Schulz, V. K. Veerapandiyan, T. Gindel, M. Deluca, and J. Töpfer, "Hexavalent (Me - W/Mo)-modified (Ba,Ca)TiO 3 -Bi(Mg, Me)O 3 perovskites for high-temperature dielectrics," *Journal of the American Ceramic Society*, vol. 103, no. 12, pp. 6881–6892, 2020, doi: 10.1111/jace.17403.

[47] Shahin Sayyed, *STUDY OF STRUCTURAL PHASE TRANSITION AND DIELECTRIC BEHAVIOR OF BiNaTiO3-SrTiO3 (BNT-ST) SOLID SOLUTION*, 2014. [Online]. Available: https://www.researchgate.net/publication/277668175_STUDY_OF_STRUCTURAL_PHASE_TRANSITION_AND_DIELECTRIC_BEHAVIOR_OF_BiNaTiO3-SrTiO3_BNT-ST_SOLID_SOLUTION

[48] Z. X. Shen, X. B. Wang, M. H. Kuok, and S. H. Tang, "Raman scattering investigations of the antiferroelectric-ferroelectric phase transition of NaNbO3," *J.*

Raman Spectrosc., vol. 29, no. 5, pp. 379–384, 1998, doi: 10.1002/(SICI)1097-4555(199805)29:5<379::AID-JRS249>3.0.CO;2-F.

[49] E. Buixaderas, C. Kadlec, P. Vaněk, S. Drnovšek, H. Uršič, and B. Malič, "Far infrared and Raman response in tetragonal PZT ceramic films," *Boletín de la Sociedad Española de Cerámica y Vidrio*, vol. 54, no. 6, pp. 219–224, 2015, doi: 10.1016/j.bsecv.2015.11.003.

[50] R. P. Dahl-Hansen, "Reliability of piezoelectric microelectomecanical systems in humid conditions," *1503-8181*, 2020. [Online]. Available: https://ntnuopen.ntnu.no /ntnu-xmlui/handle/11250/2651731